

Entwicklung einer Kalibriervorschrift und Berechnung des Unsicherheitenbudgets für das KATRIN Laser Raman System

Development of a calibration procedure and calculation of the uncertainty budget for the KATRIN laser Raman system

Masterarbeit
von

Genrich Zeller

am Institut für Experimentelle Teilchenphysik
durchgeführt am Institut für Technische Physik
Tritiumlabor Karlsruhe

Referent:	Prof. Dr. Guido Drexlin
Korreferent:	Prof. Dr. Ulrich Husemann
Betreuende Mitarbeiter:	Dr. Magnus Schlösser Hendrik Seitz-Moskaliuk Simon Niemes

Bearbeitungszeit: 01.11.2016 – 01.12.2017

Erklärung zur Selbstständigkeit

Ich versichere, dass ich diese Arbeit selbstständig verfasst habe und keine anderen als die angegebenen Quellen und Hilfsmittel benutzt habe, die wörtlich oder inhaltlich übernommenen Stellen als solche kenntlich gemacht und die Satzung des KIT zur Sicherung guter wissenschaftlicher Praxis in der gültigen Fassung vom 17.05.2010 beachtet habe.

Karlsruhe, den 01.12.2017, _____
Genrich Zeller

Als Ansichtsexemplar genehmigt von

Karlsruhe, den 01.12.2017, _____
Prof. Dr. Guido Drexlin

Contents

1	Introduction	1
2	The KATRIN experiment	3
2.1	Motivation for neutrino mass measurements and experimental overview of the KATRIN experiment	3
2.1.1	Overview of neutrino physics	3
2.1.2	The measurement principle	5
2.1.3	Overview of the experimental setup	6
2.2	The windowless gaseous tritium source (WGTS)	9
2.2.1	The working principle of the WGTS	9
2.2.2	The KATRIN requirements on source composition monitoring	9
3	Laser Raman spectroscopy for KATRIN	14
3.1	Overview of the Raman effect	14
3.1.1	Basic principles of Raman scattering and Raman spectroscopy	14
3.1.2	Theory of Raman intensities	16
3.2	The KATRIN laser Raman system	18
3.2.1	The experimental setup	18
3.2.2	Performance and achievements	19
3.3	Methods for intensity calibration of the KATRIN laser Raman system	20
3.3.1	Calibration using accurate gas samples	20
3.3.2	Calibration using theoretical intensities	21
3.3.3	Existing calibration procedure	25
4	Development of a calibration procedure for the KATRIN laser Raman system	29
4.1	Motivation and objective	29
4.2	Experimental setup of a laser Raman test system	29
4.3	Alignment procedure for the SRM 2242 for the calibration of a laser Raman system	30

4.4	Systematic investigations of the SRM 2242 with the test system	34
4.4.1	Influence of the vertical position of the SRM 2242 relative to the laser beam	35
4.4.2	Comparison of three different SRM 2242	38
4.4.3	Demonstration of the achievable reproducibility	40
4.5	Calibration of the KATRIN laser Raman system	42
4.5.1	Quantifying the reproducibility of the alignment procedure inside the glovebox	42
4.5.2	Discussion and consequences for the KATRIN experiment	45
5	Calculation of the uncertainty budget of the laser Raman source monitoring system	47
5.1	Motivation	47
5.2	Introduction to uncertainty calculation according to the Guide to the Expression of Uncertainty in Measurement	48
5.3	Uncertainty of the spectral sensitivity	51
5.4	Uncertainty budget for the KATRIN laser Raman system	57
5.4.1	General description of the measurement and model for the evaluation	57
5.4.2	Uncertainty and correlations caused by spectral sensitivity correction	58
5.4.3	Determination of other uncertainty sources in laser Raman measurements	62
5.4.4	Results and discussion	67
6	Conclusion and outlook	69
A	Spectral sensitivity measurements in every CCD bin	72
A.1	Spectral sensitivity as a function of the vertical position of the SRM 2242 .	74
A.2	Spectral sensitivity determined with three different SRM 2242	78
A.3	Spectral sensitivity determined with multiple repositionings of the SRM 2242	82
A.4	Spectral sensitivity of the KATRIN LARA system determined with multiple repositionings of the SRM 2242 inside the glovebox	86
A.5	Measured and normalized intensity curves of the SRM 2242 in every bin .	90
A.6	Histogram of the intensity values of the measured and normalized intensity curves of the SRM 2242 at 660 nm in every bin	94
A.7	Spectral sensitivity with the combined standard uncertainty confidence interval in every bin	98
B	Full calculation of uncertainties	102

List of Figures

2.1	The differential electron energy spectrum of tritium β -decay.	6
2.2	Principle of the MAC-E-Filter.	7
2.3	The setup of the KATRIN experiment.	8
2.4	Conceptual design of the Windowless Gaseous Tritium Source and the Inner Loop.	10
2.5	Final state distributions of different daughter molecules.	12
3.1	Different types of photon scattering in energy level diagrams.	15
3.2	Schematic measurement setup for Raman spectroscopy.	15
3.3	Schematic view of a typical Raman spectrum of a diatomic molecule. . . .	16
3.4	Definition of Raman scattering angles and polarization states.	18
3.5	The LARA3 beam path layout.	19
3.6	Illustration and image of the LARA cell inside the glovebox.	20
3.7	Typical Raman spectra of a gas mixture containing all six hydrogen isotopologues and a high resolution spectrum of the tritium Q_1 -branch.	23
3.8	Coverage and relative uncertainty of the Q_1 -branches by the SRM 2242 certification.	24
3.9	SRM 2242 in mount and calibration cell.	25
3.10	Spatial homogeneity of the spectral sensitivity of a CCD.	26
3.11	Reproducibility of the spectral sensitivity.	28
3.12	The spectral sensitivity as a function of the beam position within the SRM 2242.	28
4.1	Experimental setup of the LARA test system in the optical laboratory. . . .	31
4.2	Setup of the alignment screen and webcam in the LARA test setup.	32
4.3	Camera images and sketches of the laser dot passing through the SRM 2242 at different lateral positions.	33
4.4	Calibration cell and the alignment screen inside the glove box.	33
4.5	Images of three different SRM 2242 in comparison.	35

4.6	Schematic illustration of the data analysis of SRM 2242 measurements with the test system.	36
4.7	Spectral sensitivity as a function of the vertical position of the SRM 2242. .	37
4.8	Relative standard uncertainty of the spectral sensitivity for different vertical positions of the SRM 2242 in all bins of the CCD.	37
4.9	Spectral sensitivity determined with three different SRM 2242.	38
4.10	Relative standard uncertainty of the spectral sensitivity of three different SRM 2242 in all bins of the CCD.	39
4.11	Spectral sensitivity determined with multiple repositionings of the SRM 2242.	41
4.12	Relative maximum difference of the spectral sensitivity curves of multiple repositionings of the SRM 2242 in all bins of the CCD.	41
4.13	Schematic illustration of the data analysis of SRM 2242 measurements with the KATRIN LARA system.	42
4.14	Spectral sensitivity of the KATRIN LARA system determined with multiple repositionings of the SRM 2242 inside the glove box.	43
4.15	Relative maximum difference of the spectral sensitivity of the KATRIN LARA system in the relevant bins of the CCD.	44
5.1	Illustration of the GUM seven-step process for uncertainty calculation. . .	48
5.2	Comparison of the Student's distribution for different degrees of freedom and a Gaussian distribution.	49
5.3	Measured and normalized intensity curves of the SRM 2242.	52
5.4	Histogram of the intensity values of the measured and normalized intensity curves of the SRM 2242 at 660 nm.	53
5.5	Standard uncertainty of the measured intensity in different bins.	54
5.6	Standard uncertainty of the NIST certified intensity in different bins. . . .	54
5.7	Standard uncertainty of the spectral sensitivity in different bins.	55
5.8	Spectral sensitivity with the combined standard uncertainty confidence interval in bin 9.	56
5.9	Illustration of the LARASoft analysis routine.	59
5.10	Multiple measurements of the spectral sensitivity $\eta_j(x)$ with fitted linear functions.	61
5.11	Averaged spectrum $\bar{\eta}(x)$ and two spectra $\eta_{1,2}(x)$, which take the observed correlations into account.	61
5.12	Illustration of the LARASoft workflow for the astigmatism correction uncertainty calculation.	63
5.13	Illustration of the LARASoft workflow for the baseline subtraction uncertainty calculation.	65
A.1	Spectral sensitivity in every CCD bin as a function of the vertical position of the SRM 2242.	77

A.2	Spectral sensitivity in every CCD bin determined with three different SRM 2242.	81
A.3	Spectral sensitivity in every CCD bin determined with multiple repositionings of the SRM 2242.	85
A.4	Spectral sensitivity in every CCD bin of the KATRIN LARA system determined with multiple repositionings of the SRM 2242 inside the glovebox.	89
A.4	Measured and normalized intensity curves of the SRM 2242.	93
A.5	text	94
A.5	Histogram of the intensity values of the measured and normalized intensity curves of the SRM 2242 at 660 nm.	97
A.6	text	98
A.6	Spectral sensitivity with the combined standard uncertainty confidence interval in every bin.	101

List of Tables

5.1	Student's $t_p(\nu)$ -factor for different degrees of freedom and coverage probabilities.	51
5.2	Uncertainty caused by the spectral calibration.	60
5.3	Comparison of different uncertainty sources.	64
5.4	Uncertainties of relevant measurands for the LARA cell#6 measurement results and for a KATRIN-like measurement scenario.	67
B.1	Full calculation of astigmatism correction uncertainty.	102
B.2	Full calculation of baseline correction uncertainty.	103

Chapter 1

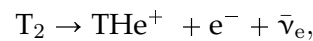
Introduction

Neutrinos are the most abundant leptonic particles in the universe. The Standard Model of particle physics describes three generations of neutrinos as weakly interacting, electrically neutral and massless. However, neutrino oscillation experiments prove that neutrinos have a non-zero rest mass [Fuk98a, Ahm02]. The actual value of the neutrino mass remains unknown, although it is an important parameter in particle physics and cosmology. The best upper limit for the electron antineutrino mass that is achieved with model-independent measurements of the tritium β -decay is $m_{\bar{\nu}_e} < 2.05 \text{ eV}/c^2$ (95 % C.L.) [Pat16]. The **K**arlsruhe **T**ritium **N**eutrino (KATRIN) experiment aims to measure the electron antineutrino mass with an unprecedented sensitivity of

$$m_{\bar{\nu}_e} = 0.2 \text{ eV}/c^2 \text{ (90 \% C.L.) [KAT05]},$$

thus improving the current laboratory limit by an order of magnitude. In the KATRIN experiment, the β -electrons are produced in a high-luminosity windowless gaseous tritium source (WGTS) and are guided adiabatically by a magnetic field to the spectrometer. The spectrometer is of MAC-E-Filter type [Pic92] and analyses the electrons with an energy resolution of $\Delta E = 0.93 \text{ eV}$.

A stable WGTS activity of 10^{11} Bq is achieved by realizing a gas column stability on the per mill level within the 10 m long beam tube which is cooled down to 30 K. This is established by a constant tritium gas injection into the beam tube centre while the gas is pumped off at the tube's ends. The gas is then reprocessed and cleaned in order to be reinjected. The isotopic tritium purity in the source should be higher than 95 % during KATRIN measurements. In addition to tritium T_2 , all other hydrogen isotopologues (DT, D_2 , HT, HD, H_2) are present in the source. All three tritium-containing molecules can undergo radioactive β -decay:



The mass difference between the three initial hydrogen molecules and the final helium hydride cation (THe^+ , DHe^+ and HHe^+) influences the kinetics of the decay and thus the energy carried away by the electron, which is the only measured particle by the experiment.

In order to account for the mass differences, it is crucial to measure and monitor the isotopic tritium purity ϵ_T and the HT-DT-ratio κ in real-time. For the KATRIN experiment to reach its ambitious goal ϵ_T needs to be measured with a trueness better than 3 % and a precision of 0.1 %, while for κ a trueness of 10 % has to be achieved [KAT05, Sch13a, Bod15].

At the KATRIN experiment a laser Raman (LARA) system is used for this purpose. In a test of the LARA system under KATRIN-like operation conditions a precision of better than 0.1 % was achieved in less than a minute of measurement time [Fis11]. In order to fulfil the trueness requirements the LARA system needs to be calibrated.

One possible method for the intensity calibration of a Raman system is to combine theoretical intensities from ab initio calculations with the experimentally measured spectral sensitivity of the Raman system at hand [Sch13a]. The theoretical intensities for the hydrogen isotopologues are provided by Schwartz and LeRoy [Sch87, LeR11]. The spectral sensitivity of a Raman system can be determined with the standard reference material (SRM) 2242, which is manufactured, distributed and certified by the American National Institute of Standards & Technology (NIST).

However, in order to use the SRM 2242 for the measurement of the spectral sensitivity and to fulfil the demanding KATRIN requirements, the SRM 2242 must be positioned relative to the laser beam with an accuracy on the level of the laser beam diameter, which is on the 100 μm level.

The main task of this work was to develop and to characterize a SRM 2242 alignment procedure for the use with the KATRIN LARA system. The second task was to calculate the uncertainty budget of the KATRIN LARA system and demonstrate that the KATRIN requirements can be fulfilled with the newly developed alignment procedure.

The thesis is structured as follows. First, in chapter 2 the motivation and experimental setup of the KATRIN experiment are described. In this context, focus is placed on the working principle of the WGTS and the requirements for gas composition monitoring. Second, an overview of laser Raman spectroscopy for the KATRIN experiment is given in chapter 3. The Raman effect in general, the KATRIN LARA system and different methods for the intensity calibration are covered. The calibration with the SRM 2242 is discussed in detail. Third, the developed calibration procedure and the investigation of various systematic effects are presented in chapter 4. The influence of the vertical position of the SRM 2242 is investigated and three different SRM 2242 plates are compared to each other with regards to their emitted spectrum. Additionally, the capability of the calibration procedure with a test system and inside of the glove box is demonstrated. Fourth, in chapter 5 the Guide to the Expression of Uncertainty in Measurement (GUM)[JCG08] is introduced. The GUM framework is applied to determine the uncertainty of the calibration procedure and the correlations and uncertainty caused by the intensity calibration. Additionally, some other sources of uncertainty are considered to determine the LARA uncertainty budget and check if the KATRIN requirements can be fulfilled. Finally, in chapter 6 a summary of the results and an outlook are given.

Chapter 2

The KATRIN experiment

Postulated and discovered in the 20th century, neutrinos are a vital part of the Standard Model of particle physics. The Standard Model describes neutrinos as massless, neutral and exclusively weakly interacting particles. However, neutrino oscillation experiments have demonstrated that neutrinos indeed have a non-zero rest mass ([Fuk98a, Ahm02]). The determination of this mass is the goal of the Karlsruhe Tritium Neutrino (KATRIN) experiment. In section 2.1 the motivation as well as theoretical and experimental basics of the KATRIN experiment are described. Then in section 2.2 the tritium source of KATRIN is presented in detail with a focused discussion of why molecular source composition monitoring on the per mill level is crucial.

2.1 Motivation for neutrino mass measurements and experimental overview of the KATRIN experiment

The KATRIN experiment at the Karlsruhe Institute of Technologie (KIT) aims to determine the effective mass of the electron antineutrino using the tritium β -decay with a sensitivity of

$$200 \text{ meV}/c^2 \text{ at a confidence level (C. L.) of } 90\% [\text{KAT05, Dre13}]. \quad (2.1)$$

The current limit of $2.0 \text{ eV}/c^2$ [Pat16] was set by Mainz ($2.3 \text{ eV}/c^2$ [Kra05]) and Troitsk ($2.05 \text{ eV}/c^2$ [Ase11]) and will thus be improved by an order of magnitude. Achieving this goal requires increased statistics and a precise understanding and reduction of systematic uncertainties.

In section 2.1.1 a short review of neutrino physics and the tritium β -decay is given. In section 2.1.2 and section 2.1.3 the measurement principle and setup of KATRIN is described briefly.

2.1.1 Overview of neutrino physics

In 1914 it was shown by J. Chadwick [Cha14] that the energy spectrum of β -decay electrons is continuous. Until then, it was assumed that the spectrum should be a monoenergetic line, since the β -decay was seen as a two-body problem. To explain the continuous

electron spectrum, W. Pauli postulated the neutrino in 1930 [Pau30, Pau85]. By adding this additional particle in an apparent two-body decay the problem could be solved:

$$n \rightarrow p^+ + e^- + \bar{\nu}_e. \quad (2.2)$$

In 1956 C.L. Cowan and F. Reines succeeded in experimentally detecting the neutrino and confirming Paulis postulate [Rei56]. Since then many properties (e.g. helicity [Gol58] and spin) of the neutrino could be determined, and described by the Standard Model. To this day, however, the value of the neutrino mass remains unknown.

Only recently, in 2015, Kajita [Fuk98a] and McDonald [Ahm02] received the Nobel price 'for the discovery of neutrino oscillations, which shows that neutrinos have mass' [Nob15]. While the neutrino oscillation experiments proof that neutrinos have a mass, they can only measure mass differences. Hence, experiments such as Mainz, Troitsk [Bel95] and the KATRIN experiment, are necessary to measure the neutrino mass directly. These experiments utilize tritium β -decay measurements.

In the following sections neutrino oscillations and the tritium β -decay are outlined.

Neutrino oscillation

The existence of neutrino oscillation was first predicted by B. Pontecorvo [Pon57]. At that time there was only one known neutrino and Pontecorvo expanded his idea [Pon68] with the discovery of the muon neutrino. The Homestake experiment, led by R. Davis [Dav68], was one of the first experiments to measure evidence for neutrino oscillations. In comparison to the theoretical model of solar neutrinos, a deficit of electron neutrinos was measured. S. Mikheyev, A. Smirnov and L. Wolfenstein could later describe this deficit in a new theoretical model [Wol78],[Mik85]. Since then, the effect of increased neutrino oscillation in matter has been known as the MSW-effect. The effect was first experimentally confirmed by the SNO experiment [Ahm02]. The neutrino oscillation effect has also been proven with atmospheric neutrinos [Fuk98b] and reactor neutrinos [An12].

Mathematically, neutrino oscillation can be described by the following equations:

$$|\nu_\alpha\rangle = \sum_i U_{\alpha i}^* |\nu_i\rangle \quad \text{and} \quad |\nu_i\rangle = \sum_\alpha U_{i\alpha} |\nu_\alpha\rangle. \quad (2.3)$$

Here $|\nu_\alpha\rangle$ are the weak flavour eigenstates with $\alpha = e, \mu, \tau$ and $|\nu_i\rangle$ ($i = 1, 2, 3$) the mass eigenstates. The matrix U is the so-called Pontecorvo-Maki-Nakagawa-Sakata (PMNS) matrix [Mak62]. The case for two neutrinos is briefly considered as an illustration. The oscillation of two neutrinos is described by

$$|\nu_e(t)\rangle = \cos\theta e^{-iE_{\nu_1}t/\hbar} + \sin\theta e^{-iE_{\nu_2}t/\hbar}, \quad (2.4)$$

where E_{ν_i} is the neutrino energy and θ the mixing angle. The probability that an electron neutrino will convert into a muon neutrino after covering a distance length L is:

$$P(\nu_e \rightarrow \nu_\mu) = \sin^2(2\theta) \sin^2\left(\frac{\Delta m_{12}^2 L}{4E}\right). \quad (2.5)$$

Since Eq. 2.5 is dependent on the squared difference of masses Δm_{12}^2 the observation of neutrino oscillations is an indirect proof for non-zero neutrino rest masses.

Tritium β -decay

This section is mainly based on [Dre13] and [KAT05]. In the KATRIN experiment the tritium β -spectrum is measured precisely in the region close to the kinematic endpoint. β^- -decay is the conversion of the mother nucleus ${}^A_Z X$ into a daughter nucleus ${}^{Z+1}_A X$ under the emission of an electron and an electron antineutrino. Inside the mother nucleus, a neutron is converted into a proton (Eq. 2.2). Correspondingly, the tritium β -decay is



Tritium has the following properties that make it the β -emitter of choice for neutrino mass investigations [KAT05]:

- The second lowest endpoint energy of all β^- -emitters $E_0 = 18.6$ keV [Mye15].
- A short half life $t_{1/2} = 12.3$ a.
- The simple electron shell of both tritium and its daughter nucleus ${}^3\text{He}^+$. This allows for the calculation of atomic and molecular corrections.
- The lowest nuclear charge number Z , which means that the inelastic scattering of out-going β -electrons in the source is small.
- A super-allowed nuclear decay into the daughter nucleus ${}^3\text{He}^+$. For this reason, no corrections from the nuclear transition matrix elements M have to be considered.

The electron spectrum is described by (slightly altered from [Dre13]):

$$\frac{d^2 N}{dt dE} = \frac{G_F^2 \cdot \cos^2(\Theta_C)}{2\pi^3} \cdot |M_{\text{nucl}}^2| \cdot F(E, Z') \cdot (E + m_e) \sqrt{(E + m_e)^2 - m_e^2} \quad (2.7)$$

$$\cdot \sum_{i,j} |U_{ei}^2| \cdot P_j \cdot (E_0 - E - V_j) \sqrt{(E_0 - E - V_j)^2 - m^2(\nu_i)} \cdot \Theta(E_0 - E - V_j - m(\nu_i)).$$

Here G_F is the Fermi constant and Θ_C the Cabbibo angle. The nuclear matrix transition element $|M_{\text{nucl}}^2|$ is characteristic for the β -decaying nucleus as well as the Fermi function $F(E, Z')$, which additionally depends on nuclear charge of the daughter nucleus and Coulomb interaction between the emitted electron and the daughter nucleus. The electron's kinetic energy and mass are denoted by E and m_e . The endpoint energy E_0 is the maximal kinetic energy of the electron. V_j denotes different possible excited states of the daughter molecule. For more information and the derivation the reader is referred to [Dre13]. In Fig. 2.1 the electron energy spectrum of the tritium β -decay is depicted. The neutrino mass appears as a quadratic term in Eq. 2.7. Therefore, the KATRIN experiment has to surpass Mainz and Troitsk by a factor of 100 in regards to statistic and systematic uncertainty to achieve a ten times better mass sensitivity.

2.1.2 The measurement principle

The KATRIN experiment combines ideas from the two previous experiments from Mainz and Troitsk. Both experiments used a so-called MAC-E-Filter¹, but with different characteristics of tritium sources. In its basics a MAC-E-Filter acts as an integrating high-energy

¹Magnetic Adiabatic Collimation combined with an Electrostatic Filter

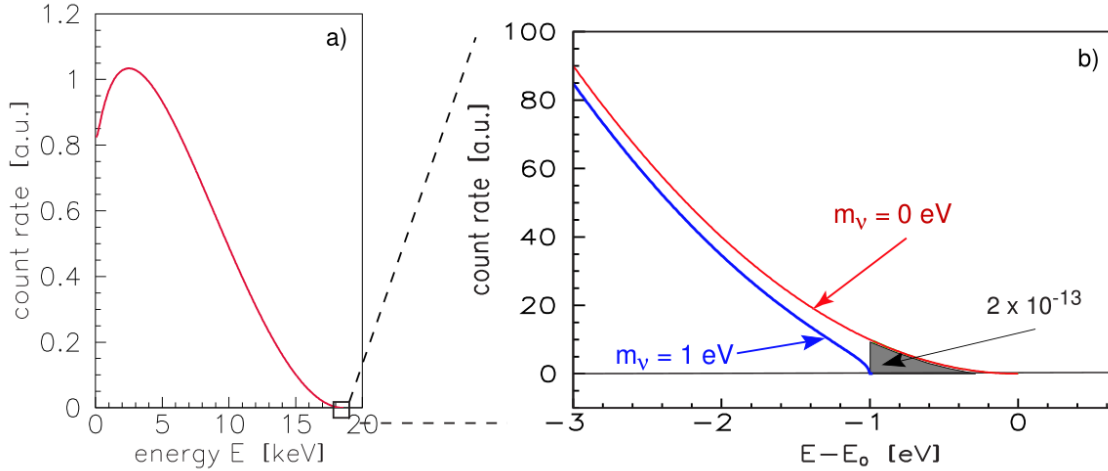


Figure 2.1: The differential electron energy spectrum of tritium β -decay. a) Complete energy range. b) Small energy range close to the Endpoint E_0 . In red the curve for a vanishing neutrino mass $m_\nu = 0 \text{ eV}$ is shown. The blue curve shows the distortion of the curve and the shift of the endpoint for a non-zero neutrino mass of $m_\nu = 1 \text{ eV}$. The grey-shaded area corresponds to a fraction of $2 \cdot 10^{-13}$ β -decay electrons. (Fig. from [KAT05].)

pass filter. The basic principle of the experiment is that electrons from a tritium source are led to a detector. The MAC-E-Filter (Fig. 2.2), has an electric retardation field parallel to the magnetic field lines. Additionally, the magnetic moment of the electrons is oriented to be parallel to the magnetic field lines at the central region by an inhomogeneous magnetic field. This allows to measure the energy of passing electrons with a resolution of $\Delta E = 0.93 \text{ eV}$. The neutrino mass can be obtained from the integral spectrum measured with this counting experiment. Many systematic effects have to be taken into account and the KATRIN experiment is on the edge of technical feasibility in order to achieve the design sensitivity.

2.1.3 Overview of the experimental setup

The entire setup of the KATRIN experiment can be seen in Fig. 2.3. The setup has a length of 70 m and consists of seven main components. These will be described in more detail in the following.

The calibration and monitoring system is at the rear end of the setup. The rear wall closes the WGTS at one end. The rear section is used to monitor the source activity and column density. The source monitoring is performed by beta induced X-ray spectrometry (BIXS) [Röl15]. For the monitoring of the column density a precision electron gun is employed [Bab14].

The windowless gaseous tritium source (WGTS) is the high luminosity β -electron source used in the KATRIN experiment. The inner beam tube, which contains the decaying tritium is 10 m long. The source emits about 10^{11} electrons per second in a magnet field of 3.6 T. Tritium is injected into the WGTS and flows from the source to the transport section. Since the WGTS and source composition monitoring are major parts of this work, the

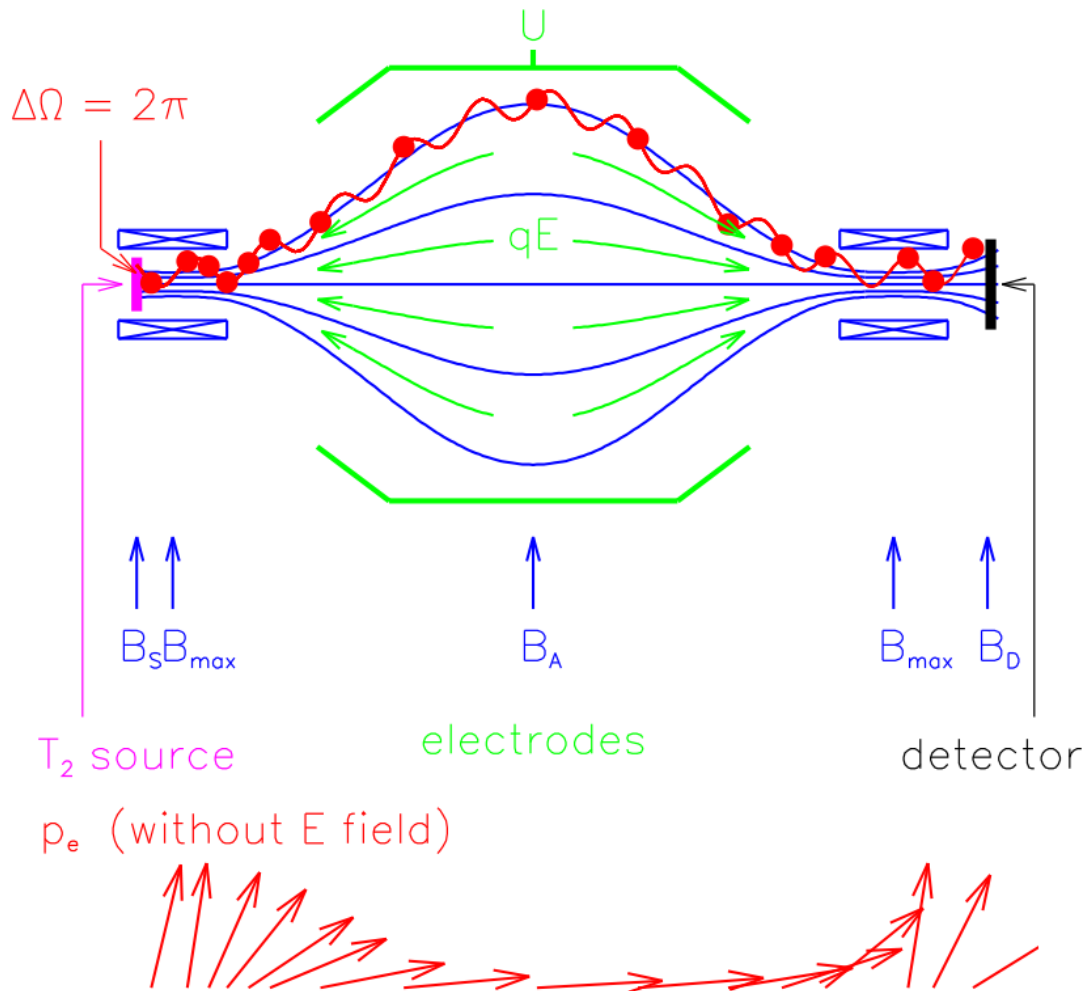


Figure 2.2: Principle of the MAC-E-Filter. *top:* Two superconducting solenoids produce a magnetic guiding field. The electrons from the ' T_2 source' side enter the spectrometer and follow the magnetic field lines on a cyclotron motion around the lines. Towards the central region of the spectrometer the magnetic field drops by many orders of magnitude. Additionally, an electric retardation field is applied. *bottom:* Illustration of the transformation of the magnetic momentum vector of the electrons by the magnetic gradient force created by the inhomogeneous magnetic field. In the central region the magnetic momentum is almost parallel to the magnetic field lines. (Fig. from [KAT05].)

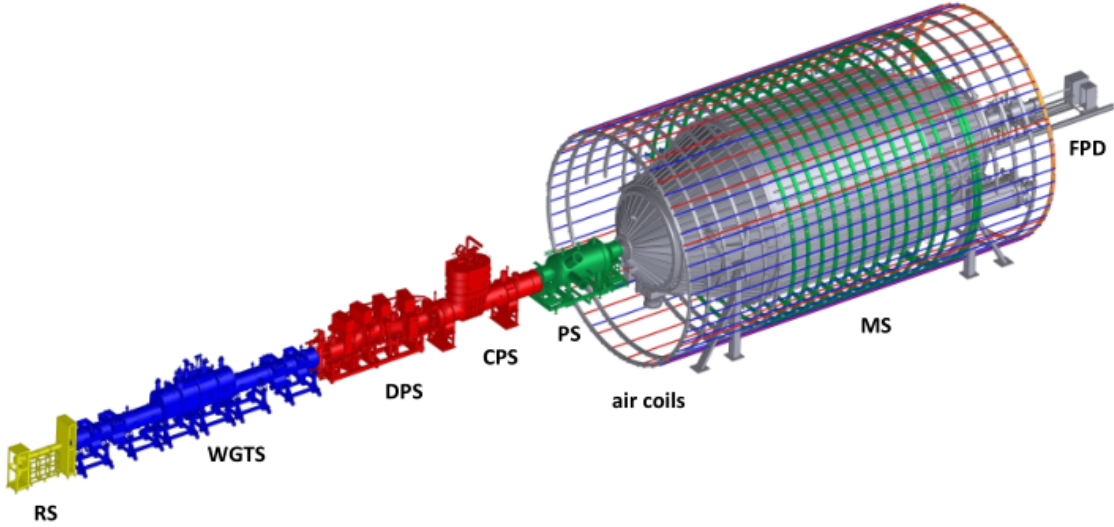


Figure 2.3: The setup of the KATRIN experiment. The setup is 70 m long and consists of seven components: (i) the rear section (RS), (ii) the windowless gaseous tritium source (WGTS), (iii) the differential pumping section (DPS), (iv) the cryogenic pumping section (CPS), (v) the pre-spectrometer (PS), (vi) the main spectrometer (MS) surrounded by air coils and (vii) the focal plane detector (FPD). Further details on each component are given in the main text. (Fig. from [Sch14b].)

details are discussed in section 2.2.

The transport system consists of two sections, the differential pumping section (DPS) followed by the cryogenic pumping section (CPS). The transport system has two main tasks: (i) the tritium flow has to be reduced by a factor of 10^{14} , so no tritium can enter the spectrometer section, and (ii) the electrons have to be guided adiabatically from the WGTS to the spectrometer section. For the first task the DPS uses turbo molecular pumps. The CPS utilises cryosorption: At a temperature of 3 K the tritium molecules are adsorbed on an argon frost layer and thus the tritium flux is reduced by seven orders of magnitude. The electrons are guided adiabatically by a magnetic field with a field strength of up to 5.7 T which is created by superconducting solenoids. The pumped tritium is cleaned in the infrastructure of the Tritium Laboratory Karlsruhe (TLK) and then returned to the WGTS.

The spectrometer system consists of a pre-spectrometer and a main spectrometer. Both are of MAC-E-Filter type. The pre-spectrometer is a first high-pass filter for the electrons. It is a 3.4 m long stainless steel cylinder with a diameter of 1.7 m and can only be passed by electrons with an energy closer than 300 eV to the end point E_0 . The low energetic electrons would only contribute to the background by impacts with residual gas atoms. The electron rate is reduced to 10^3 electrons per second. The main spectrometer (23.3 m long and 10 m in diameter) is the main analysing component. It analyses the remaining electrons with an energy resolution of $\Delta E = 0.93$ eV. It is surrounded by air coils (diameter 12.6 m) to allow for fine-tuning of the magnetic field in the centre.

The **focal plane detector** is made of silicon and segmented into 148 pixel of the same surface area for optimal spatial resolution. It detects electrons with an efficiency $> 90\%$.

At this point in time the whole beam line is assembled and was successfully tested with artificially produced electrons in 2016. This was one of KATRIN's big milestones and called *first light* [Hac17]. In addition, in the summer of 2017, a successful measurement phase with krypton was conducted.

2.2 The windowless gaseous tritium source (WGTS)

On a technical level the WGTS is made of a 10 m long and cylindrical stainless steel tube with a diameter of 90 mm (see Fig. 2.4). The source tube is connected to a closed tritium loop, called the Inner Loop [Stu10b]. The tube is surrounded by superconducting solenoids which create a magnetic field up to 3.6 T. The WGTS is operated at a nominal temperature of 27 K using a two phase liquid neon cooling system.

2.2.1 The working principle of the WGTS

Molecular tritium T_2 is constantly injected in the middle of the source tube at constant pressure. The gaseous tritium flows to both ends of the tube, where it is pumped off using turbo molecular pumps. These end sections are called DPS1-F (front-facing) and DPS1-R (rear-facing). Due to the constant injection with an injection pressure of 0.334 Pa [Kuc16] and pumping on both ends a constant longitudinal tritium density profile is formed inside the tube (see Fig. 2.4). The pumped gas is then passed trough the Inner Loop [Stu10b] and reinjected into the WGTS. This ensures a stable composition of gas in the source. The WGTS has a design throughput of 40 g d^{-1} . The tritium decays within the WGTS and emits up to 10^{11} β -electrons per second. The magnetic field guides the electrons adiabatically towards the transport section ('downstream').

In order to monitor the composition of the WGTS a laser Raman (LARA) system is part of the Inner Loop.

2.2.2 The KATRIN requirements on source composition monitoring

In order for the KATRIN experiment to reach its ambitious goal, the total systematic uncertainty budget [KAT05] for m_ν^2 has to be

$$\sigma_{\text{sys,tot}} \leq 0.017 \text{ eV}^2/c^4. \quad (2.8)$$

During the design phase of KATRIN five dominant effects were identified. This means that every individual effect should not contribute more than

$$\Delta m_\nu^2 < 7.5 \cdot 10^{-3} \text{ eV}^2/c^4 \quad (2.9)$$

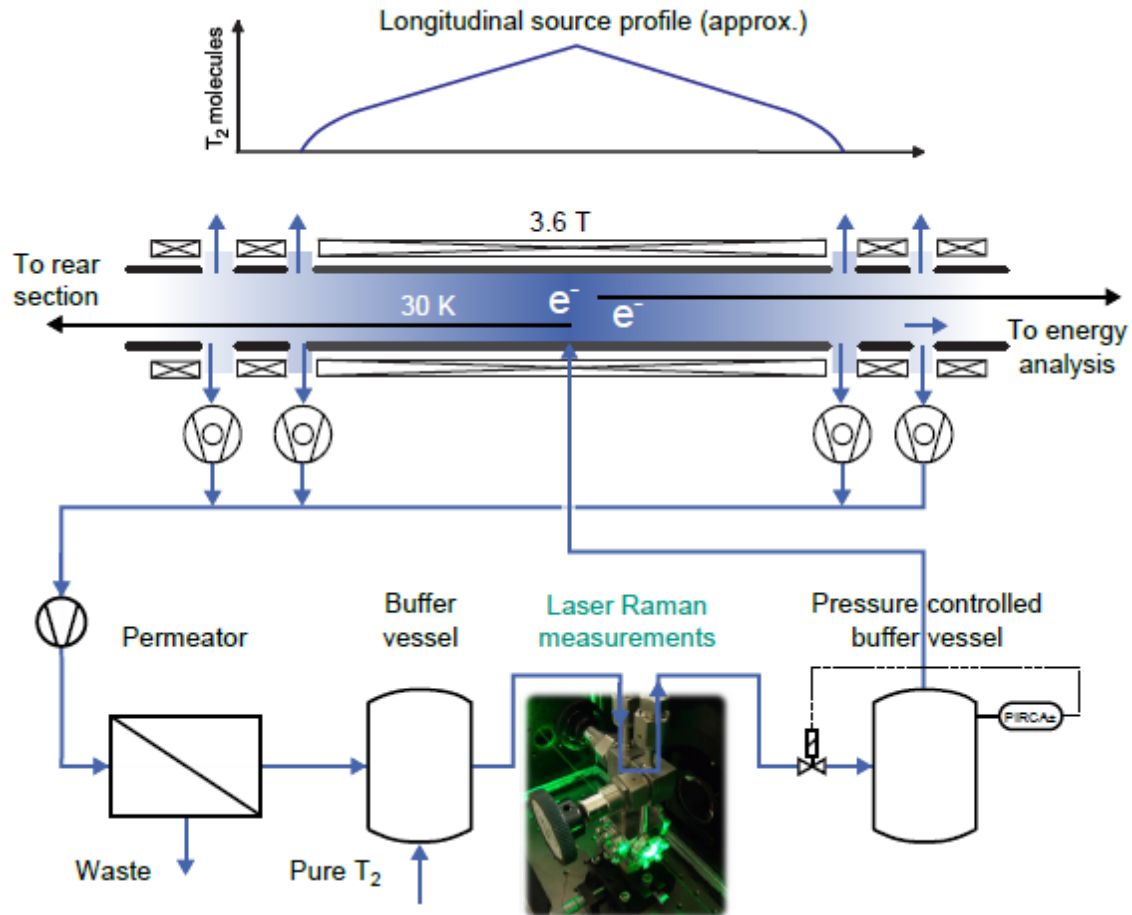


Figure 2.4: Conceptual design of the Windowless Gaseous Tritium Source and the Inner Loop. *top:* The longitudinal tritium source profile. It needs to be stable on 1 per mille level during KATRIN operation. *bottom:* The Inner Loop [Stu10b] which provides the gas circulation. A buffer vessel is filled with high purity tritium ($\epsilon_T > 0.95$) from the TLK infrastructure. The gas composition is measured by a laser Raman system while the gas flows into a pressure controlled buffer vessel. From there it is injected into the WGTS beam tube with a constant flow. The gas is pumped out by turbomolecular pumps at both sides and the impurities from the tritium decay are filtered by a permeator. The cleaned gas is fed back into the loop. Whenever necessary high-purity tritium is added from the TLK infrastructure. (Fig. from [Sch13a] reprinted with permission of Springer.)

to the neutrino mass analysis [KAT05]. Two key parameters of the WGTS have a significant influence on the systematic uncertainty: the isotopic tritium purity ϵ_T and the column density \mathcal{N} [Bab12]. They impact the source activity S

$$S = C \cdot \epsilon_T \cdot \mathcal{N}. \quad (2.10)$$

In this equation C is a constant factor dependent on detector efficiency and other experimental parameters [Bab12]. In the following section the two key parameters are presented in greater detail, mainly based on [KAT05] and [Bab12].

Column density

The column density \mathcal{N} is defined as the number of molecules per cross-section area. The nominal column density is $\mathcal{N} = 5.0 \cdot 10^{17}$ molecules/cm² and it has to be monitored and stabilized in real-time to better than 0.1 %. This is important, because the column density not only effects the source activity S , but also the energy loss from inelastic electron scattering. The stabilization is achieved by stabilizing the external WGTS operating parameters effecting the column density: (i) the beam tube temperature, (ii) the pumping speed of DPS1-F and DPS1-R and (iii) the injection rate. Additionally, the column density will be measured between neutrino mass measurement with an electron gun from the calibration and monitoring system. For in-line monitoring a combination of source activity and source composition will be employed, utilizing Eq. 2.10.

Source composition

Ideally, the source would contain pure tritium. In reality the source will contain mostly molecular tritium (mole fraction $c_{T_2} > 0.9$), some parts of DT ($c_{DT} < 0.1$) and traces of the other four hydrogen isotopologues (HT, D₂, HD, H₂). The mole fraction c_x of a constituent x is defined as

$$c_x = \frac{N_x}{\sum_i N_i}, \quad (2.11)$$

where N_x is the number of molecules of the specific isotopologue x and $\sum_i N_i$ is the number of all atoms within the WGTS. It should be noted that $\sum_i c_i = 1$. An alternative representation of the source composition can be the isotopic tritium purity ϵ_T and the HT-DT-ratio κ [Bod15]. The tritium purity is defined as

$$\epsilon_T = \frac{N_{T_2} + \frac{1}{2}(N_{HT} + N_{DT})}{\sum_i N_i}. \quad (2.12)$$

It represents the fraction of all tritium atoms relative to the total number of atoms within the source and KATRIN is designed to operate with $\epsilon_T > 95\%$ at all times [Bab12]. This maximizes the source activity (Eq. 2.10). Additionally, the HT-DT-ratio κ , which is defined as

$$\kappa = \frac{N_{HT}}{N_{DT}}, \quad (2.13)$$

has to be taken into account, since ϵ_T does not contain any information about the number of the individual isotopologues. Some systematic effects require the accurate measurement of the absolute isotopologue composition. These are discussed in the following list.

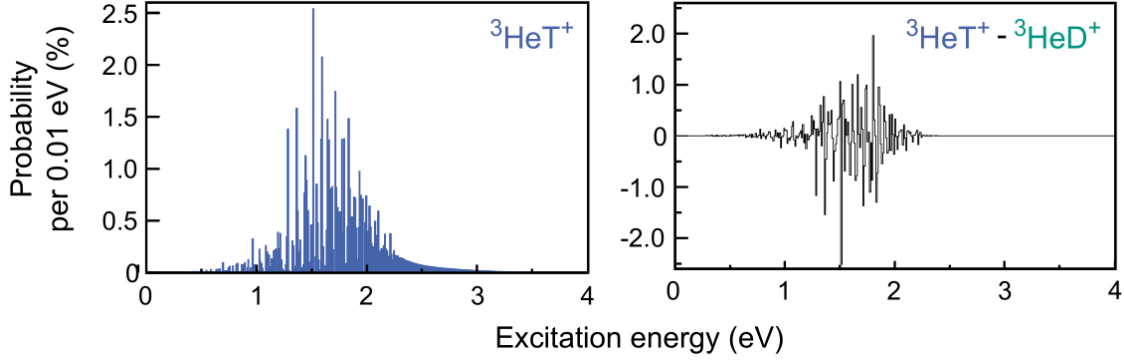


Figure 2.5: Final state distributions of different daughter molecules. *left:* Final state distribution of the $({}^3\text{HeT})^+$ daughter molecule. *right:* Difference between final state distributions of the $({}^3\text{HeT})^+$ daughter molecule and the $({}^3\text{HeD})^+$ daughter molecule. Therefore, the total spectrum has to be weighted over the contributions of the isotopologues. (Fig. from [Sch13a] based on data from [Dos06] reprinted with permission of Springer.)

- **Nuclear recoil:** Due to the emission of an electron and an electron antineutrino, recoil energy is transferred to the daughter molecule (e.g. $({}^3\text{HeT})^+$) during β -decay. This recoil energy is not available for the electron as kinetic energy and shifts the spectrum towards smaller energies. Close to the energetic endpoint, the recoil energy balances the momentum of the electron [KAT05]:

$$E_{\text{rec}} \approx E \cdot \frac{m_e}{m_X}, \quad X = \text{HT, DT, T}_2. \quad (2.14)$$

Since the recoil energy E_{rec} depends on the mass of the daughter molecule m_X , the β -spectrum is dependent on the isotopologic composition of the WGTS. In reality, the measured β -spectrum is a weighted superposition of the single spectra of T_2 , DT and HT β -decay.

- **Final state distribution:** In the explanation for Eq. 2.7 it was mentioned that the daughter molecule can be excited to different states by the recoil of the β -decay. The electronic excitations are negligible for the energy interval relevant for KATRIN [KAT05]. Nevertheless, different rotational-vibrational states are populated. As shown in Fig. 2.5, different daughter molecules have different final state distributions. Therefore the source composition as to be accounted for and the β -spectrum calculated as a weighted sum of the single spectra of T_2 , DT and HT.
- **Doppler effect:** Due to the thermal motion of molecules in the gas and the resulting Doppler effect, the electron energies of the beta-decay electrons are shifted. Additionally, within the WGTS all molecules are moving towards one of the ends in a bulk motion. In the non-relativistic approximation the correction can be described by [KAT05]:

$$\Delta E \approx m_e \cdot v_e \cdot v_{X,\parallel}, \quad (2.15)$$

where m_e, v_e denote the electron's mass and velocity (in the center-of-mass system of the molecule) and $v_{X,\parallel}$ is the velocity component of the molecule parallel to the direction of the electron. Molecular velocities at a certain temperature depend on the molecular masses, therefore the composition of the gas has to be taken into account.

- **Elastic electron scattering:** In addition to inelastic scattering, the electrons scatter elastically with the molecules. The energy loss of the electron due to elastic scattering is [KAT05]

$$\Delta E = 2 \frac{m_e}{m_X} E_e (1 - \cos \theta_s). \quad (2.16)$$

In this equation m_e , E_e denote the electron's mass and initial energy, θ_s the scattering angle and m_X the molecule's mass. Due to the dependency on m_X the knowledge of the source composition is required for a proper calculation of the elastic energy loss.

Requirements on the LARA system for source monitoring

Since the source activity (Eq.2.10) and previously listed effects depend on the source composition, a continuous composition monitoring is necessary. For the KATRIN experiment in particular a precision¹ of the isotopic composition $\epsilon_T < 0.1\%$, analogous to the stability of the activity/column density, is required. Additionally, a trueness of 3% is required to keep the systematic uncertainty well below $\sigma_{\text{sys}}(m_\nu^2) = 3 \cdot 10^{-3} \text{ eV}^2/c^4$ [Sch12a]. Also a trueness below 10% is required for the HT-DT-ratio κ [Bod15]. These requirements can be fulfilled using a laser Raman (LARA) system. The LARA system is part of the Inner Loop (Fig. 2.4).

Laser Raman spectroscopy and the LARA system itself are explained in greater detail in chapter 3.

¹Simplified: Precision is related to relative changes and trueness to the absolute values. A measurement is accurate if it is both true and precise.

Chapter 3

Laser Raman spectroscopy for KATRIN

In this chapter, the theoretical and experimental basics for understanding laser Raman spectroscopy and the laser Raman (LARA) system are presented. Section 3.1 gives an introduction to the theoretical background. In section 3.2 the experimental setup and the performance of the KATRIN LARA system are briefly described. Section 3.3 introduces possibilities for intensity calibration of the KATRIN LARA system and briefly describes the current procedure and its shortcomings.

3.1 Overview of the Raman effect

The Raman effect is the inelastic scattering of light by molecules. Already predicted by A. Smekal in 1923 [Sme23], the effect was first observed by C. V. Raman and K. S. Krishnan in 1928 [Ram28]. In contrast to infrared spectroscopy it is also possible to measure homonuclear molecules. This is one of the reasons why it is employed in the KATRIN experiment for composition monitoring. In addition, it enables real-time monitoring of the gas composition without sample taking. The brief theoretical descriptions in the following sections are based on the books of Haken/Wolf [Hak06], Long [Lon02], Demtröder [Dem07] and Atkins [Atk06].

3.1.1 Basic principles of Raman scattering and Raman spectroscopy

In contrast to elastic Rayleigh scattering, the wavelength of scattered light changes by Raman scattering. The Raman effect is $10^3 - 10^4$ times smaller than the Rayleigh scattering [Atk06]. In Fig. 3.1 the different types of photon scattering are shown. In Raman scattering, a molecule is excited into a virtual state by absorption of a photon. By emitting a photon, the molecule reaches its final state. If the energy of the emitted photon is lower than the original energy (the photon is red-shifted) and therefore the energy of the molecule is higher, the effect is called Stokes Raman scattering. In the opposite case, where the photon is blue-shifted, it is anti-Stokes Raman scattering. In the scope of this thesis only the Stokes Raman scattering is of importance. The Stokes Raman lines are more intense

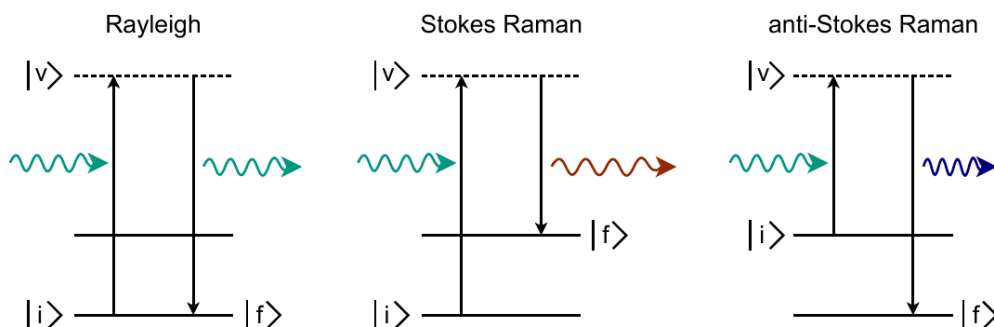


Figure 3.1: Different types of photon scattering in energy level diagrams. The photon excites the molecule from its initial state $|i\rangle$ into a virtual state $|v\rangle$. The molecule then transitions into the final state $|f\rangle$. *Rayleigh scattering*: $|i\rangle = |v\rangle$, there is no change in photon wavelength. *Stokes Raman scattering*: $E_i < E_f$, the photon is red-shifted. *Anti-Stokes Raman scattering*: $E_i > E_f$, the photon is blue-shifted. (Fig. from [Sch13a] reprinted with permission of SpringerLink.)

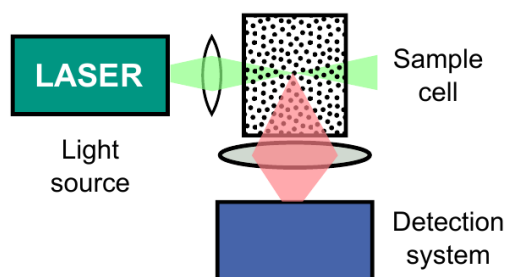


Figure 3.2: Schematic measurement setup for Raman spectroscopy. The main components of a generic Raman experiment. A light source, a sample cell and a detection system arranged in a 90° orientation. (Fig. from [Sch13a] reprinted with permission of SpringerLink.)

at low temperatures then Anti-Stokes Raman lines, because for the Anti-Stokes Raman scattering the molecules have to be in an excited state. The Raman effect can be used for spectroscopy. In a typical setup (Fig. 3.2) a laser excites the molecules in a sample cell and the scattered photons are then detected. Often a 90° geometry is chosen to reduce the light diffusely reflected from the excitation laser or fluorescence from the optical windows arriving the collection optics for the Raman light. Fig. 3.3 shows a schematic view of a typical Raman spectrum for diatomic molecules. This work will focus exclusively on the treatment of diatomic molecules, since they are relevant for the KATRIN experiment. The lines in the spectrum correspond to different molecular transitions. The quantum number J describes rotational states and v the vibrational states. Allowed rotational transitions are $\Delta J = -2, 0, +2$, represented by O, Q and S, respectively. The vibrational transitions can be $\Delta v = -1, 0, +1$, but the LARA experiment focuses on $\Delta v = 1$, since the Q₁-branches of the hydrogen isotopologues are so far apart from each other that they can be easily resolved and have the highest intensities of all the branches. The general nomenclature for the transitions is $\Delta J_{\Delta v}$.

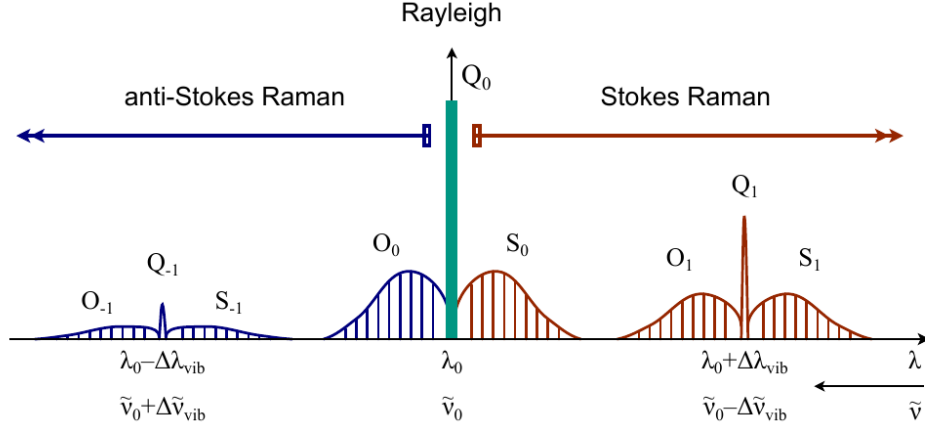


Figure 3.3: Schematic view of a typical Raman spectrum of a diatomic molecule. The diagram shows the typical distribution of Raman lines and intensities. (Fig. from [Sch13a] reprinted with permission of SpringerLink.)

3.1.2 Theory of Raman intensities

According to Long [Lon02], the intensity of light scattered on diatomic molecules is given as

$$I(\varphi, \theta)_{p^s, p^i} = k_{\tilde{\nu}} \cdot \tilde{\nu}_s^4 \cdot N_i \cdot \Phi(\varphi, \theta, a, \gamma)_{p^s, p^i} \cdot \mathcal{I}. \quad (3.1)$$

This formula is based on quantum mechanical calculations. It is only valid if the intensity is measured in units of power [McM06]. If instead the intensity is measured in number of photons, e.g. using a CCD, the wavenumber dependency changes from $I(\varphi, \theta)_{p^s, p^i} \propto \tilde{\nu}_s^4$ to $I(\varphi, \theta)_{p^s, p^i} \propto \tilde{\nu}_0 \tilde{\nu}_s^3$:

$$I(\varphi, \theta)_{p^s, p^i} = k_{\tilde{\nu}} \cdot \tilde{\nu}_s^3 \cdot \tilde{\nu}_0 \cdot N_i \cdot \Phi(\varphi, \theta, a, \gamma)_{p^s, p^i} \cdot \mathcal{I}. \quad (3.2)$$

Additionally it is often useful to use the wavelength instead of the wavenumber:

$$I(\varphi, \theta)_{p^s, p^i} = k_{\lambda} \cdot \lambda_s^{-3} \cdot \lambda_0^{-1} \cdot N_i \cdot \Phi(\varphi, \theta, a, \gamma)_{p^s, p^i} \cdot \mathcal{I}. \quad (3.3)$$

The constants and variables are described in the following list.

$(\varphi, \theta)_{p^s, p^i}$: The parameters p^s and p^i indicate the line polarisation plane of the scattered and incident light, while φ and θ describe the direction of the scattered beam relative to the scattering plane (see Fig. 3.4).

$k_{\lambda}, k_{\tilde{\nu}}$: Constants, where k_{λ} is given as

$$k_{\lambda} = \frac{\pi^2}{\epsilon_0^2} \approx 1.259 \cdot 10^{23} \text{m}^2 \text{F}^{-2} \quad (3.4)$$

with ϵ_0 being the permittivity of vacuum.

$\lambda_0, \tilde{\nu}_0$: The wavelength/wavenumber of the incident light.

$\lambda_s, \tilde{\nu}_s$: The wavelength/wavenumber of Raman scattered light with

$$\tilde{\nu}_s = \tilde{\nu}_0 - \Delta\tilde{\nu}_i \quad (3.5)$$

with $\Delta\tilde{\nu}_i$ being the Raman shift corresponding to a certain molecular state i .

N_i : The population factor, which is given as

$$N_i(E_i) = N \cdot \frac{g_i \exp\left(-\frac{E_i}{k_b T}\right)}{Z} \quad (3.6)$$

and represents the number of molecules in the initial state in thermodynamic equilibrium and is defined by a Boltzmann distribution. Here N is the total number of molecules irradiated, g_i the statistical weight of the initial state, k_b the boltzmann constant, T the temperature of the sample, E_i the energy of the initial state and Z the molecular partition function

$$Z = \sum_j g_j \exp\left(-\frac{E_j}{k_b T}\right). \quad (3.7)$$

The statistical weight consists of a rotational and a vibrational part

$$g_i = g_{J''} \cdot g_{\nu}. \quad (3.8)$$

For diatomic molecules, the vibrational states are non-degenerated and therefore $g_{\nu} = 1$, while the statistical weight $g_{J''}$ depends on the rotational quantum number J'' and the nuclear spin degeneracy g_N :

$$g_{J''} = g_N \cdot (2J'' + 1). \quad (3.9)$$

At this point a distinction between heteronuclear (e.g. HT, DT, DT) and homonuclear (e.g. T₂, D₂, H₂) molecules has to be made. For heteronuclear $g_N = 1$. In the case of homonuclear molecules g_N is J'' depended and different for molecules with two fermionic nuclei (T₂, H₂) or two bosonic nuclei (D₂). The values are

$$\text{T}_2, \text{H}_2 : \quad g_N = 1, 3 \quad \text{for } J'' = \text{even, odd}, \quad (3.10)$$

$$\text{D}_2 : \quad g_N = 6, 3 \quad \text{for } J'' = \text{even, odd}. \quad (3.11)$$

$\Phi(\varphi, \theta, a, \gamma)_{p^s, p^i}$: The line strength functions, which depend on the experiment's geometry and light polarization. The tensor invariants, the mean polarizability a and the polarizability anisotropy γ , are specific for each isotopologue and molecular transition. The four line strength functions [Lon02] are

$$\Phi(\varphi, \theta, a, \gamma)_{\perp^s, \perp^i} = a^2 \cos(\varphi)^2 + b^{(2)} \frac{\gamma^2}{45} (4 - \sin(\varphi)^2), \quad (3.12)$$

$$\Phi(\varphi, \theta, a, \gamma)_{\perp^s, \parallel^i} = a^2 \sin(\varphi)^2 + b^{(2)} \frac{\gamma^2}{45} (3 + \sin(\varphi)^2), \quad (3.13)$$

$$\Phi(\varphi, \theta, a, \gamma)_{\parallel^s, \parallel^i} = a^2 \cos(\varphi)^2 \cos(\theta)^2 + b^{(2)} \frac{\gamma^2}{45} (3 + \cos(\theta)^2 \cos(\varphi)^2), \quad (3.14)$$

$$\Phi(\varphi, \theta, a, \gamma)_{\parallel^s, \perp^i} = a^2 \cos(\theta)^2 \sin(\varphi)^2 + b^{(2)} \frac{\gamma^2}{45} (3 + \cos(\theta)^2 \sin(\varphi)^2). \quad (3.15)$$

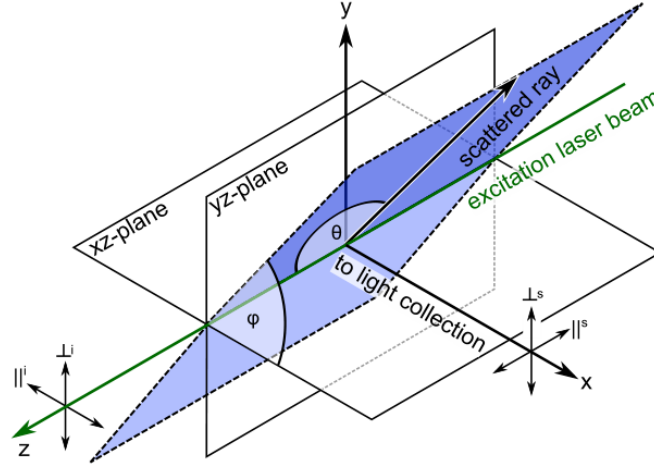


Figure 3.4: Definition of Raman scattering angles and polarization states. The incident laser beam determines the z -axis. The x -axis is defined by the direction towards the light collection. The y -axis forms a right-handed coordinate system with the z - and x -axis. The scattering plane is determined by the z -axis and the azimuth angle φ . The angle in the scattering plane between the scattered ray and the z -axis is the zenith angle θ . The polarization of linear polarized light relative to the xz -plane is denoted with \perp and \parallel . (Fig. from [Sch13a] reprinted with permission of SpringerLink.)

The factor $b^{(2)}$ is the Placzek-Teller factor and is given as

$$b^{(2)} = \frac{J(J+1)}{(2J-1)(2J+3)} \quad (3.16)$$

with the rotational state J .

\mathfrak{I} : The irradiance of the incident light. It cancels out during further calculations and has no significance.

3.2 The KATRIN laser Raman system

In this section the KATRIN laser Raman (LARA3) system is described. This system will be used for KATRIN measurements. In section 3.2.1 the experimental setup is presented. Achievements are discussed in section 3.2.2. If not stated otherwise the description follows [Fis14], where much more detailed informations can be found. The LARA3 system can be seen as a successor to two other Raman systems developed at TLK, LARA1 and LARA2. Each having there own respective advantages and disadvantages. The LARA3 system is optimized in regard to sensitivity, precision and reliability.

3.2.1 The experimental setup

The LARA3 setup is divided into three main sections. In the first section the laser beam is guided to the sample cell. The sample cell itself is the second section. In the third section

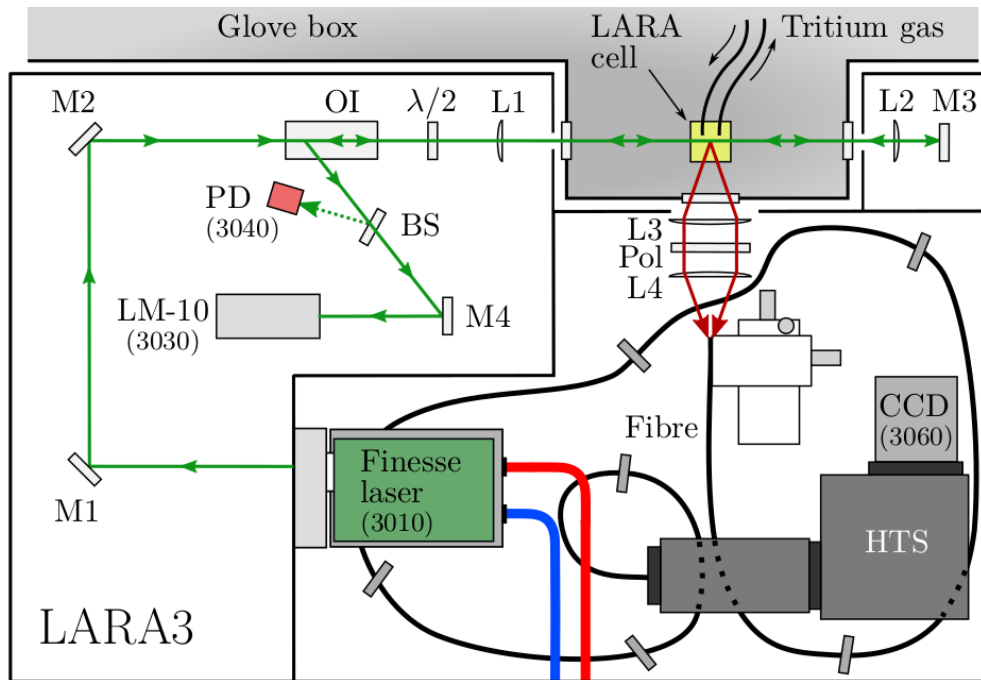


Figure 3.5: The LARA3 beam path layout. These components are installed: Finesse Laser, M_i - Mirrors, OI - Optical Isolator, PD - photo diode, LM-10 - thermopile power meter, $\lambda/2$ - Half waveplate, L_i , plano-convex lenses, Pol - linear sheet polarizer, Optical fibre, HTS - spectrometer and Pixis CCD. The numbers (nnnn) are used for KATRIN-wide identification of sensors and active devices. (Fig. from [Fis14].)

the scattered light is collected and guided to the CCD. These sections can be seen in Fig. 3.5. Additionally, a monitoring system measures the laser beam for safe long-term operation. The sample cell is located in a glovebox (see Fig. 3.6). It is either filled with a gas sample or is flowed through by gas as part of the Inner Loop. The two mirrors M_1 , M_2 guide the laser beam towards the sample cell. The mirror M_3 reflects the laser beam so it passes the sample cell a second time (double pass configuration). The optical isolator deflects the reflected beam for safe beam dumping and beam walk monitoring using the beam splitter, the photo diode and the power meter. The lens L_1 (L_2) focuses the (reflected) laser beam in the middle of the sample cell. The scattered light is focused on to the optical fibre bundle utilizing the lenses L_3 and L_4 . The fibre transmits the light to the spectrometer and the CCD. In order to maximize the line strength functions (see chapter 3.1.2) of the Q_1 branches the laser beam has to be vertically polarized with respect to the surface of the breadboard. This is achieved using a $\lambda/2$ half waveplate. The linear sheet polariser in the collection section is also aligned for transmission of vertically polarized light. A more detailed description of the setup, the components and the commissioning can be found in [Fis14].

3.2.2 Performance and achievements

The gas circulation system LOOPINO [Stu10a, Fis11] was used to test the LARA3 system in a KATRIN-like operation. The LOOPINO system can be seen as a simplified version

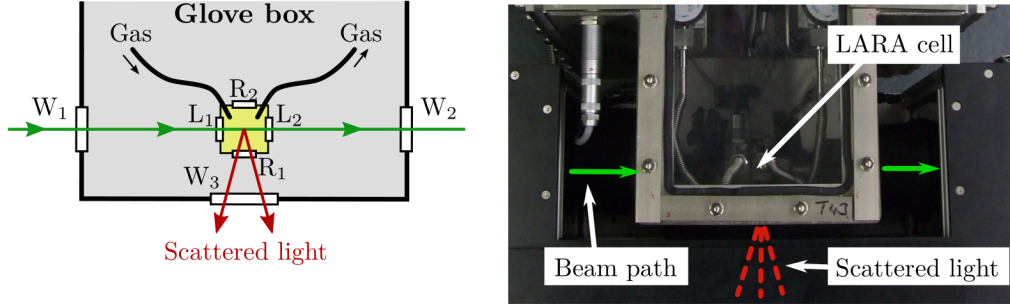


Figure 3.6: Illustration and image of the LARA cell inside the glovebox. This hardware interface is called appendix. *left*: Illustration with labelled windows. L_i are laser windows, R_i are windows for Raman scattered light and W_i are the appendix windows. *right*: Actual image of the appendix with the LARA cell and indicated light paths. (Fig. from [Fis14].)

of the inner loop. A tritium sample was circulated in LOOPINO for more than 3 weeks. Continuous measurements with LARA3 were taken for five days. In addition to important findings for the operation and improvement of LARA3, it could be shown that the KATRIN requirements for measuring precision of 0.1% could be fulfilled. A relative precision of $3 \cdot 10^{-4}$ for the relative Raman intensity of the T_2 branch at 29.5 seconds acquisition time was achieved [Fis14]. The test has also shown that the Raman system is suitable for monitoring the gas composition in the Inner Loop despite the indirect connection through the appendix.

3.3 Methods for intensity calibration of the KATRIN laser Raman system

In the following sections the possible methods for the intensity calibration of the KATRIN LARA system are described. The first possibility (section 3.3.1) is the measurement of accurate gas samples. Section 3.3.2 shows the second possible method. It is based on a combination of theoretical intensities and the measured spectral sensitivity of the given system. These calibration strategies were developed and described in [Sch13a]. The current calibration procedure is described in 3.3.3.

3.3.1 Calibration using accurate gas samples

For an accurate gas sample the mole fraction

$$y_x = \frac{N_x}{\sum_i N_i} \quad (3.17)$$

of each isotopologue x is known. By measurement of the Raman signal S_x of the gas sample the proportionality factor, the response function R_x , can be determined:

$$R_x = \frac{S_x}{N_x} = \frac{S_x}{y_x \sum_i N_i}. \quad (3.18)$$

The only unknown factor $\sum_i N_i$ cancels out when relative response functions are calculated.

To create accurate gas samples the HYDE (hydrogen deuterium) loop was developed and build at the TLK [Sei11, Sch13a]. By well controlled mixing of H₂ and D₂ and the use of a catalyst calibration mixtures containing H₂-HD-D₂ are produced. Using the calibration mixtures the response functions for non-radioactive hydrogen isotopologues could be determined with an calibration uncertainty < 0.4 % [Sch13a].

However, the transition from non-tritiated gas samples to tritiated gas samples is difficult and requires a completely new facility, TriHYDE. It is currently being set up at the TLK and is intended to produce mixtures with an uncertainty level comparable to the HYDE loop.

One main problem with the use of tritiated gas samples for the calibration is that they are not stable due to the radioactive decay of tritium to helium-3 (about 0.5 % per month). Therefore, the gas samples are only valid calibration standards for a certain period of time. Additionally, for the calibration of the KATRIN LARA system the calibration mixture has to be brought into the appendix and removed after the calibration. Nevertheless, the calibration with accurate gas samples is important for cross-checking of the second possible calibration method.

The TriHYDE facility will be available in 2018.

3.3.2 Calibration using theoretical intensities

The second possible calibration approach combines theoretical intensities from ab initio calculations with the measured spectral sensitivity in order to determine the system's response function. In the first part of this section the theoretical framework for this calibration procedure [Sch13a] is presented. In the second part the standard reference material (SRM) 2242 is presented as a way to measure the spectral sensitivity of a Raman system.

The extended theoretical framework for the calibration procedure

Equation (3.3) can also be written for a certain hydrogen isotopologue x

$$I_{\text{Raman},x}(\lambda_s, N_x) = k_\lambda \cdot \lambda_s^{-3} \cdot \lambda_0^{-1} \cdot N_x \cdot \Phi(\varphi, \theta, a, \gamma)_{p^s, p^i, x} \cdot \mathfrak{J}. \quad (3.19)$$

In order to obtain the actual Raman signal, two further aspects must be taken into account. First, this formula represents a theoretical Raman signal. The spectral sensitivity $\eta(\lambda_s)$ of the experimental setup must be included in order to obtain the measured Raman signal. The spectral sensitivity is unique for each system and setup and describes the wavelength dependent efficiency of the photon detection. The measured Raman Signal is then given as

$$S_x = \eta(\lambda_s) \cdot I_{\text{Raman},x}(\lambda_s, N_x) \quad (3.20)$$

$$= \eta(\lambda_s) \cdot k_\lambda \cdot \lambda_s^{-3} \cdot \lambda_0^{-1} \cdot N_x \cdot \Phi(\varphi, \theta, a, \gamma)_{p^s, p^i, x} \cdot \mathfrak{J}. \quad (3.21)$$

Secondly, in the previous derivation show in section 3.1.2 it was assumed that the Q_1 branches are equal to single lines. In reality, this is not the case. The Q_1 branches are unresolved single lines of different J'' initial states (can be seen in Fig. 3.7). If this is taken into account, the formula changes to

$$= k_\lambda \cdot \lambda_0^{-1} \cdot N_x \cdot \mathcal{J} \sum_{J''} \left(\eta(\lambda_{s,J''}) \cdot \lambda_{s,J''}^{-3} \cdot \Phi_{x,J''}(2J'' + 1) g_N \exp\left(-\frac{\tilde{F}(J'')hc}{kT}\right) / Q \right), \quad (3.22)$$

where Q is the molecular partition function [Lon02]

$$Q = \sum_{J''} \left((2J'' + 1) g_N \exp\left(-\frac{\tilde{F}(J'')hc}{kT}\right) \right) \quad (3.23)$$

and $\tilde{F}(J'')$ are the rotational term energies. These can be obtained by accurate measurement of the line positions and are provided by Schwartz und LeRoy [Sch87]. It is reasonable to approximate that the spectral sensitivity does not change over the width of a Q_1 branch (see Fig. 3.7) and therefore does not depend on J'' :

$$S_x = \underbrace{k_\lambda \cdot \lambda_0^{-1} \cdot \mathcal{J} \cdot N_x \cdot \eta(\lambda_s)}_{\text{const.}} \underbrace{\sum_{J''} \left(\lambda_{s,J''}^{-3} \cdot \Phi_{x,J''}(2J'' + 1) g_N \exp\left(-\frac{\tilde{F}(J'')hc}{kT}\right) / Q \right)}_{r_x}, \quad (3.24)$$

$$= C \cdot N_x \cdot \underbrace{\eta(\lambda_s) \cdot r_x}_{R_x}. \quad (3.25)$$

The spectral sensitivity $\eta(\lambda_s)$ and the theoretical intensities r_x are both necessary in order to obtain N_x from the measured Raman signal S_x . They can be combined into the response function if necessary (i.e. for cross validation of different calibration methods). The constant C cancels out during the calculation of any relative values.

The theoretical intensities r_x are calculated according to

$$r_x = \sum_{J''} \left(\lambda_{s,J''}^{-3} \cdot \Phi_{x,J''}(2J'' + 1) g_N \exp\left(-\frac{\tilde{F}(J'')hc}{kT}\right) / Q \right). \quad (3.26)$$

The spectral sensitivity $\eta(\lambda_s)$ has to be determined experimentally by measuring some kind of known/certified spectrum using the LARA system. The ratio of the measured and theoretically known spectrum defines the spectral sensitivity:

$$\eta(\lambda_s) = \frac{I_{\text{meas.}}}{I_{\text{theo.}}} \quad (3.27)$$

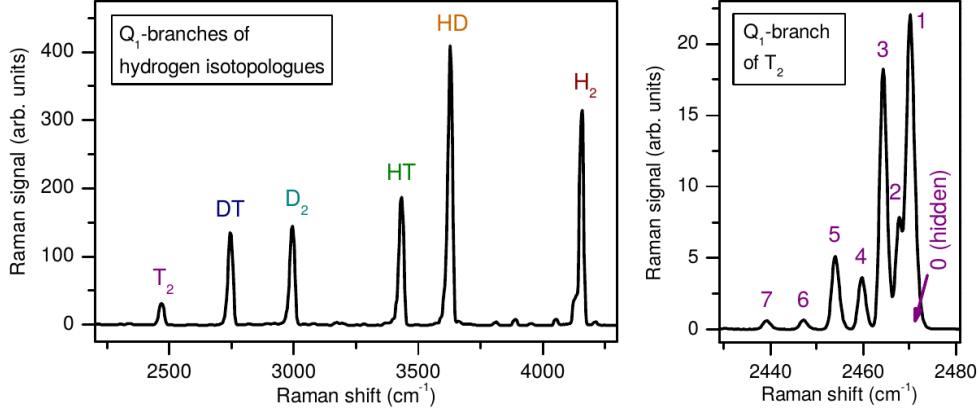


Figure 3.7: Typical Raman spectra of a gas mixture containing all six hydrogen isotopologues and a high resolution spectrum of the tritium Q₁-branch. *Left:* Overview spectrum. The Q₁-lines are assigned to the respective peaks. No individual lines in the Q₁ branches are visible. *Right:* High resolution spectrum of the Q₁-branch of T₂ showing the individual lines. (Fig. from [Sch13a] reprinted with permission of SpringerLink.)

The Standard Reference Material (SRM) 2242

The luminescence standard SRM 2242 is manufactured, certified and distributed by the National Institute of Standards and Technology (NIST) [NIS08]. The standard was developed specifically for the calibration of Raman systems. The luminescence standard is a glass plate doped with MnO₂ (Fig. 3.9). There are two different versions of the standard: The original version has one frosted front surface and measures 10.7 mm × 30.4 mm × 2.0 mm. The newer version has two polished front surfaces and is 10.7 mm × 30.4 mm × 1.6 mm in size. When the SRM 2242 is excited with 532 nm laser light it emits a broadband spectrum, which is certified between 150 cm⁻¹ and 4000 cm⁻¹. The shape of the spectrum is described by a fifth-order polynomial

$$I_{\text{SRM}}(\lambda) = \frac{10^7}{\lambda^2} \cdot \sum_{i=0}^5 A_i Y(\lambda)^i \quad \text{with} \quad Y(\lambda) = 10^7 \cdot \left(\frac{1}{532 \text{ nm}} - \frac{1}{\lambda} \right), \quad (3.28)$$

which is provided and certified by NIST. Additionally, NIST provides certified 95% confidence curves in polynomial form. For the region outside of 4000 cm⁻¹ (relevant for H₂) an extended set of measured data was requested and obtained from NIST. The data is shown in Fig. 3.8. The certification is valid for temperatures between 20 °C and 25 °C. If the SRM 2242 is employed in different conditions a corrections has to be used:

$$(\Delta\nu, T)_{\text{SRM}} = (T_{\text{meas}} - 21 \text{ °C}) \cdot (-1.9 \text{ cm}^{-1}/\text{°C}) + (\Delta\nu)_{\text{SRM}}. \quad (3.29)$$

This correction shifts the x -axis and has to be applied before Eq. 3.28.

The SRM 2242 is designed for the calibration of Raman system with a 180° scattering geometry. However, as the described in section 3.2.1 the KATRIN LARA system is a 90° configuration. In this configuration the laser beam enters the SRM 2242 through one of the lateral surfaces instead of the intended front surfaces. This causes some issues which are discussed in section 3.3.3.

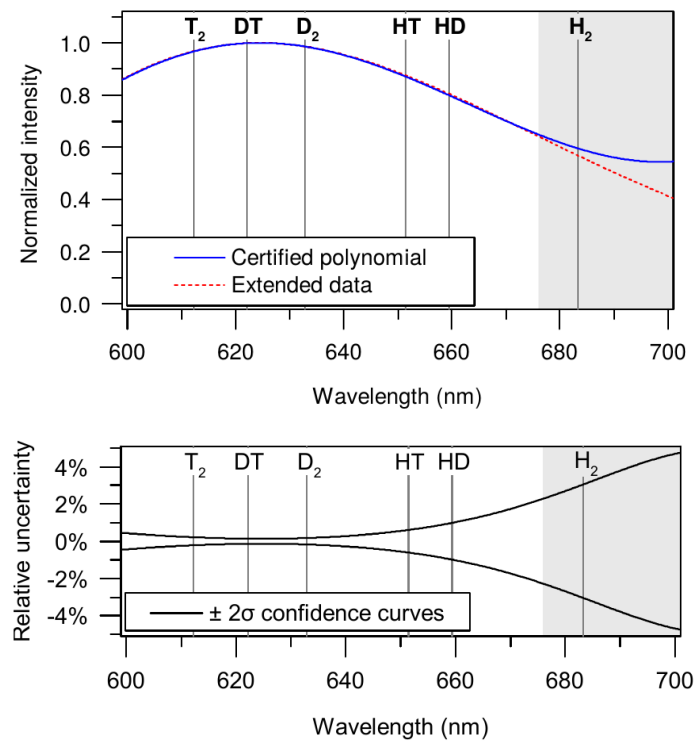


Figure 3.8: Coverage and relative uncertainty of the Q_1 -branches by the SRM 2242 certification. The vertical lines mark the positions of the Q_1 lines of the hydrogen isotopologues. The gray area indicates the extended data range. (Fig. from [Rup12].)

3.3.3 Existing calibration procedure

The calibration cell

A special calibration cell is used for the calibration with the SRM 2242. The calibration cell has the same dimensions as a standard LARA cell (Fig. 3.9). Instead of being a closed cell, it has a window installed on one side and pinholes installed on two opposite sides. The pinholes enable exact alignment of the laser beam relative to the breadboard of the LARA system. The SRM 2242 itself is mounted vertically in a holder (Fig. 3.9) and can be placed in the calibration cell from above. Additionally, the holder allows x - and y -positioning of the SRM 2242 relative to the calibration cell and therefore the laser beam. The calibration cell and the standard LARA cell are easily interchangeable without touching any other part of the system. All these measures ensure that the setup is the same during spectral calibration as for Raman measurement. If the system would be changed by the exchange of the cell, the calibration would become invalid. This also means that every time a component is changed or moved, the calibration has to be repeated.

Results of systematic investigations with the SRM 2242

The summary of all systematic studies and the calibration procedure including software analysis steps can be found in [Sch15a]. In this section the most relevant results are summarized.

(i) It was discovered that every CCD has a spectral sensitivity with a 2D structure (see Fig. 3.10). For typical Raman measurements the y -pixel of the CCD are grouped into vertical bins to reduce read-out noise. Later on, in the software routine the values along the vertical bins are summed to obtain a 1D spectrum ('binning'). Since the CCD has a different spectral sensitivity in every vertical bin, it is necessary to apply the spectral sensitivity correction before the binning step. Additionally, it is not practical to give one spectral sensitivity curve $\eta(x)$ for the whole CCD rather the spectral sensitivity has to be calculated, analysed and reported per vertical bin (i)

$$\eta^{(i)}(x). \quad (3.30)$$

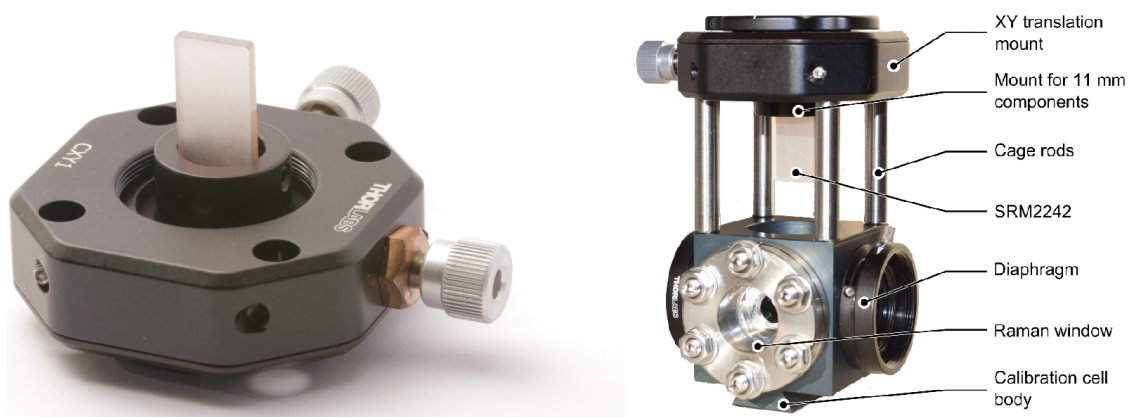


Figure 3.9: SRM 2242 in mount and calibration cell. *Left:* SRM 2242 mounted in the XY translation mount. It is important that the standard plate is oriented along the x - y -axis defined by the two screws. Only then the calibration is possible. Note that the screws have no scale on them. *Right:* Fully assembled calibration cell with labelled parts. (Fig. from [Sch15a].)

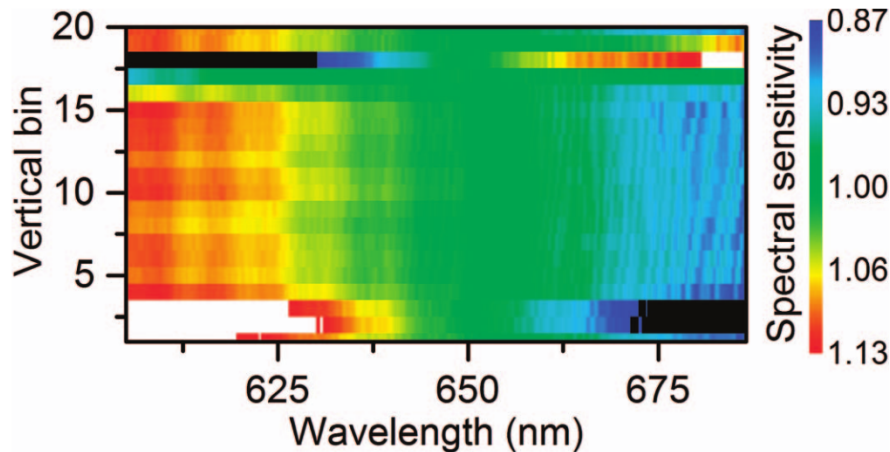


Figure 3.10: Spatial homogeneity of the spectral sensitivity of a CCD. In the black regions the spectral sensitivity is < 0.87 , while in the white regions the spectral sensitivity is > 1.13 . (Fig. from [Sch15a].)

Therefore, it is no longer possible to simply calculate the system's response function, because it is different for every vertical bin of the CCD.

(ii) In order to account for laser polarization effects, which only occur in the 90° configuration the spectrum of the SRM 2242 has to be measured twice and averaged. The measurements have to be performed with laser polarisation of $\pm 45^\circ$ relative to the polarization used for the Raman measurement.

(iii) Additionally, it has been shown that the calibration using the SRM 2242 is not reproducible for simple reinsertions if the polished side of the SRM 2242 faces the Raman collection optics and no further precautions are taken (Fig. 3.11). The frosted side does not show this behaviour, probably because the frosting averages the light coming from the SRM 2242. Further investigations of this problem have shown that the spectral sensitivity strongly depends on where the 2 mm thick standard is hit by the laser beam (Fig. 3.12). Additionally, the spectral sensitivities from the polished/frosted side only agree if the laser beam passes through the standard directly under the surface. These discoveries led to an alignment procedure for the SRM 2242 containing the following instructions.

- a) 'If a frosted SRM is available, this should be installed such that the frosted side faces the Raman collection optics.' [Sch15a]
- b) 'The SRM position should be adjusted so that the laser beam passes directly under the SRM surface (as previously discussed). This is achieved using the XY translator attached to the SRM mount to move the SRM across the laser beam laterally. To find the optimal alignment directly under the surface, we suggest moving the SRM away from the collection optics while measuring the SRM spectrum until the spectral intensity begins to reduce significantly. This corresponds to the beam passing outside of the standard. Controlled by a micrometer screw, the SRM standard is then moved slightly back again by a distance of $\approx 250 \mu\text{m}$.' [Sch15a]

Problems and open points

These instructions cause some problems, which will be discussed in the following list.

- a) Luminescence standards with one frosted and one polished side are no longer produced by NIST. Since all studies have been carried out with a standard of this kind, it is necessary to examine if the same effects occur with a double polished standard and if the proposed solutions can still be applied.
- b) The studies were performed on different LARA systems, but none of them had the sample and calibration cell placed inside the appendix. With the protective gloves on and restricted vision it will be very difficult to move the standard by a distance of $\approx 250 \mu\text{m}$. A different way of insuring that the laser beam is aligned directly under the surface is needed, which can work inside the appendix.

To solve these issues is the main task of this thesis:

- The summarized investigations show that the SRM 2242 needs to be accurately positioned relative to the laser beam. The laser beam has to hit the SRM 2242 directly below the surface. For the source monitoring of the KATRIN experiment it is crucial to develop an alignment procedure which will work inside the glove-box environment of the appendix. Only then the KATRIN LARA system can be calibrated.
- The uncertainty caused by the new alignment method has to be calculated and it has to be confirmed that the KATRIN requirements can be fulfilled. This is the main test the alignment procedure has to pass.
- A complete uncertainty budget for KATRIN LARA system needs to be calculated. Current calculations do not consider possible correlations and make assumptions about the gas composition.
- It needs to be determined how often recalibrations will be necessary.

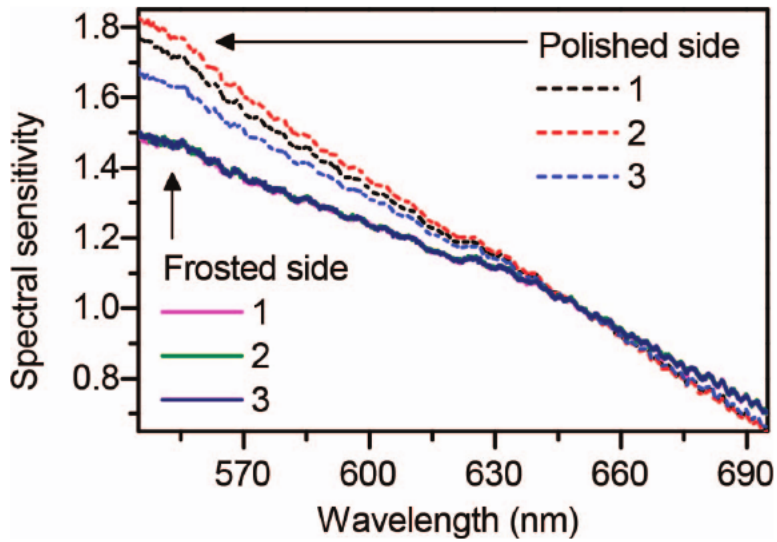


Figure 3.11: Reproducibility of the spectral sensitivity. Measurements were taken with different sides facing the collection optics. Three reinserition were performed with each side. (Fig. from [Sch15a].)

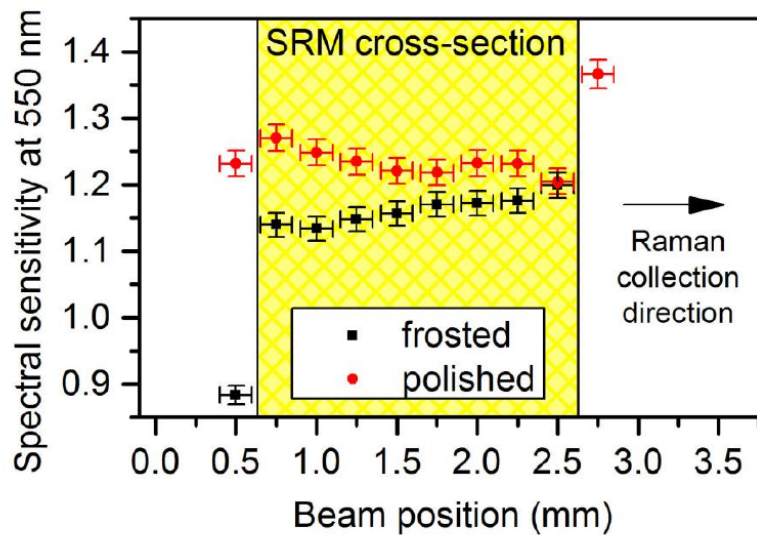


Figure 3.12: The spectral sensitivity as a function of the beam position within the SRM 2242. Measurements were taken with different sides facing the collection optics. Only the values directly under the surface agree. (Fig. from [Sch15a].)

Chapter 4

Development of a calibration procedure for the KATRIN laser Raman system

4.1 Motivation and objective

The previous chapter summarized the results for using the SRM 2242 in 90° scattering geometry. It was shown that the only missing piece for the successful calibration of the KATRIN LARA system is an alignment procedure for the SRM 2242. The alignment procedure should ensure a well reproducible lateral positioning of the SRM 2242 relative to the laser beam in the glovebox of the appendix.

If the laser beam hits the SRM 2242 directly under the surface, it is ensured that the emitted spectrum of the standard is the spectrum certified by NIST. In order to develop and test such an alignment procedure, a test system (section 4.2) was set up in the optical laboratory of the Tritium Laboratory Karlsruhe (TLK). In section 4.3 the newly developed alignment procedure is described. Additionally, it is discussed how the alignment procedure needs to be adjusted to fit the different LARA systems used. In section 4.4 the alignment procedure is used in combination with the test system to investigate various systematic effects and the achievable reproducibility with the test system is demonstrated. Lastly, in section 4.5 the alignment procedure is used for the calibration of the KATRIN LARA system. The reproducibility is quantified and the results are discussed.

4.2 Experimental setup of a laser Raman test system

Working on the KATRIN LARA system requires handling inside a glovebox environment, as the KATRIN LARA cell and calibration cell are located in the appendix. This means that if an alignment method is to be tested, which requires e.g. a modification of the calibration cell, the necessary material must be brought into the glovebox. This is very time consuming and may produce unnecessary amounts of possibly¹ contaminated material. The handling

¹According to TLK standards everything leaving the glovebox environment is treated as contaminated until measurements of the material in question prove the opposite.

inside the glovebox environment is also associated with great limitations in freedom of movement and operability. Therefore, it is more reasonable to develop and test an SRM 2242 alignment procedure independent of the KATRIN LARA system. Of course, the limitations of the glovebox must be taken into consideration during the development phase. For this purpose, a LARA test system was set up. This test system (Fig. 4.1) basically follows the experimental setup presented in section 3.2.1 and is described below.

- (i) Optical fibre bundle that is coupled to a laser². The laser generates light with a wavelength of 532 nm. A lens with a focal length of $f = 10$ mm is used to create a collimated laser beam.
- (ii) A shutter to open/close the laser source. It is connected to the interlock safety system of the optical laboratory.
- (iii) Two mirrors to guide and align the laser beam.
- (iv) A Glan-Taylor polariser to align the polarisation of the laser beam perpendicular to the breadboard surface.
- (v) A $\lambda/2$ plate to rotate the polarisation of the laser beam by a fixed angle. This is necessary, because the SRM 2242 spectrum needs to be measured at $\pm 45^\circ$ relative to the position set by the Glan-Taylor polariser.
- (vi) Focusing lens with a focal length of $f = 100$ mm.
- (vii) The calibration cell with the SRM 2242. The cell is an exact duplicate of the cell used in the glovebox and shown in Fig. 3.9.
- (viii) The collecting optics for the scattered light. The scattered light is first collimated by a lens and passes through a polariser. The polariser is used to determine the polarisation of the light before entering the fibre bundle. It is set to transmit as much light as possible. A second lens focuses the light on the optical fibre bundle. The optical fibre bundle guides the light to a spectrometer and a CCD (not shown in the picture). The fibre bundle is of type slit-to-slit unordered.

The whole system is carefully aligned and tested with the standard reference cell used at TLK. The system is wavelength calibrated using a neon lamp.

4.3 Alignment procedure for the SRM 2242 for the calibration of a laser Raman system

The alignment procedure is based on the observation of the laser beam dot after it passes through the SRM 2242. For the observation of the laser beam dot a screen is placed behind the calibration cell. In Fig. 4.2a the screen used with the test system is shown. This screen is made from anodized black aluminium. The laser dot on the screen can be recorded

²gem 532 from Laser Quantum

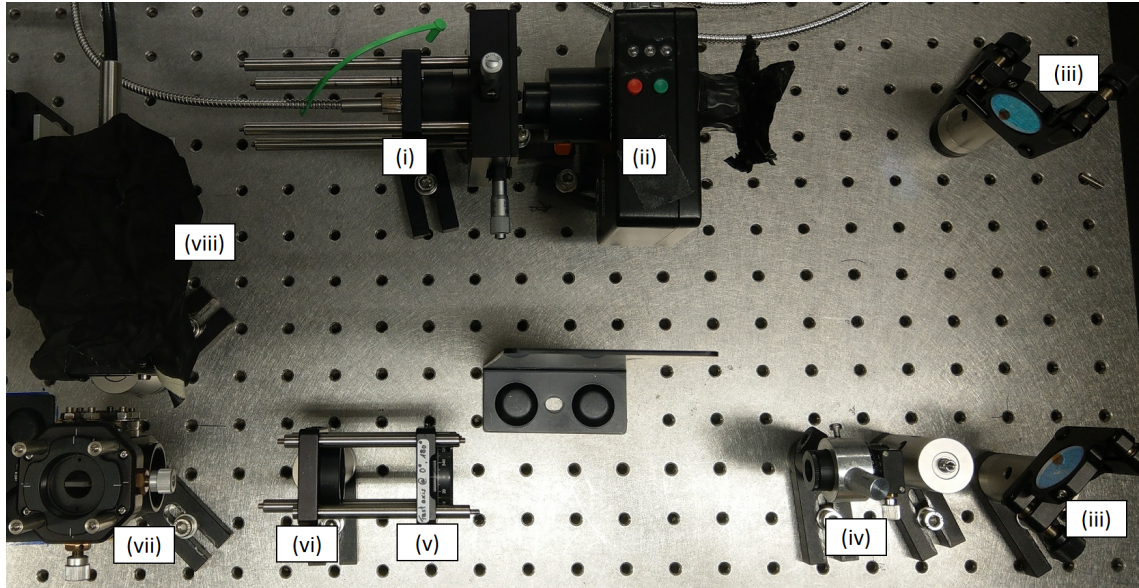


Figure 4.1: Experimental setup of the LARA test system in the optical laboratory. The system consist of (i) a laser source, (ii) the shutter, (iii) mirrors, (iv) a polarizer, (v) a $\lambda/2$ plate, (vi) a focusing lens, (vii) the calibration cell and (viii) the collection optics. More details can be found in the main text.

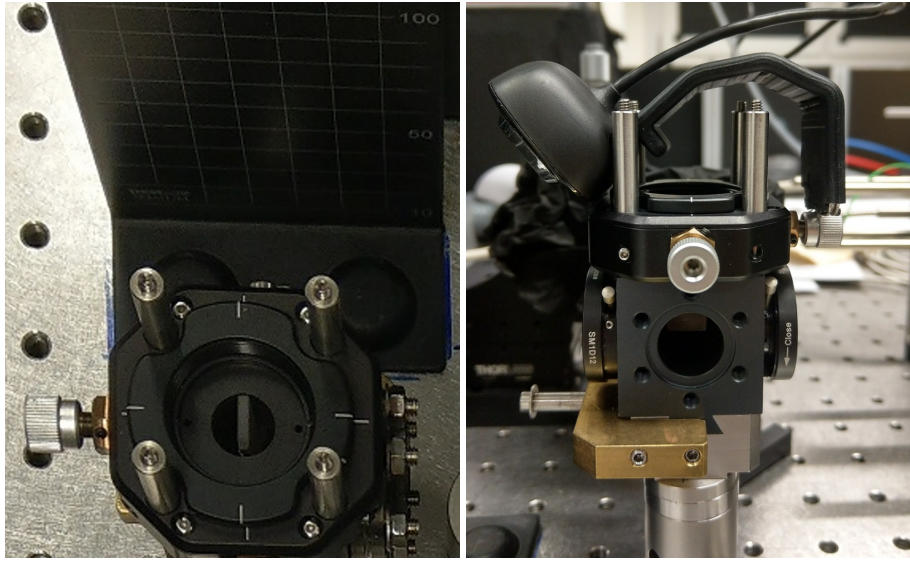
using a camera³ (see Fig. 4.2b) or observed with the naked eye. In Fig. 4.3 the actual camera images and schematic drawings for the successive movement of the SRM 2242 are shown. In Fig. 4.3a the laser hits the SRM 2242 somewhere in the centre of the plate. The SRM 2242 is then moved away from the collection optics (Fig. 4.3b) and the under the surface point is reached in Fig. 4.3c. In Fig. 4.3d the shape of the laser dot changes. While it was previously circular, the shape now appears distorted. This observation can be explained by the fact that the laser beam now slightly touches the inner edge of the SRM 2242. Thus, the under the surface spot is passed. If the SRM 2242 is moved further the laser hits the edge directly, reflections of the laser beam become visible (Fig. 4.3e).

The alignment procedure is based on the visible difference between Fig. 4.3c and Fig. 4.3d. As soon as the shape of the laser dot appears distorted the under the surface spot is passed. The SRM 2242 is then moved back until the distortions disappear. The whole procedure and setup can be summarized as follows:

The image of the laser beam passing trough the SRM 2242 is projected onto a screen and observed. The standard is positioned in such a way that the laser dot is not distorted by the proximity to the edge. In this case, the laser beam hits the SRM 2242 just below the surface.

Depending on the screen, diameter of the laser dot and laser power, the dot has to be observed with a camera, the naked eye or adjusted by a neutral density filter. If the dot appears oversaturated or faint it is difficult to observe the laser dot shape. The images in Fig. 4.3 show an optimal combination of screen choice, camera settings and laser dot size.

³Different cameras were used: A Microsoft LifeCam HD-3000 (can be seen in Fig. 4.2b), a digital microscope camera and the camera of a LG G4 smartphone. All produced the same results.



(a) Screen placed behind the calibration cell. (b) Webcam placed on top of the calibration cell.

Figure 4.2: Setup of the alignment screen and webcam in the LARA test setup. The screen is placed behind the calibration cell. The distance between the centre of the calibration cell and the screen is approximately the focal length of the focusing lens ($f = 100$ mm). The camera is placed on top of the cell, thereby it is as close to the screen as possible with little perspective distortion of the image.

KATRIN LARA system

Due to the limitations of the glovebox, the screen and camera setup for the KATRIN LARA system is different from the test system. The modified setup is shown in Fig. 4.4. The constraints can also be identified in the picture. The following issues require modification of the setup:

- (i) The laser beam is leaving the glovebox after passing through the calibration cell through a window (covered by the paper screen in Fig. 4.4). The window distorts the image of the laser dot, therefore the screen cannot be placed outside of the glovebox.
- (ii) The camera needs to be connected to a PC or at least a power source. Due to the necessary cabling, the camera cannot be placed inside the glovebox.
- (iii) The viewing angle into the glovebox is restricted. The operator can only look through the top window. Therefore, the screen cannot be placed upright in the glovebox.

These issues are solved with the following modifications:

- (i) The screen is placed in the glovebox right behind the calibration cell.
- (ii) The camera is placed outside of the glovebox on the top window.
- (iii) The screen is placed diagonally.

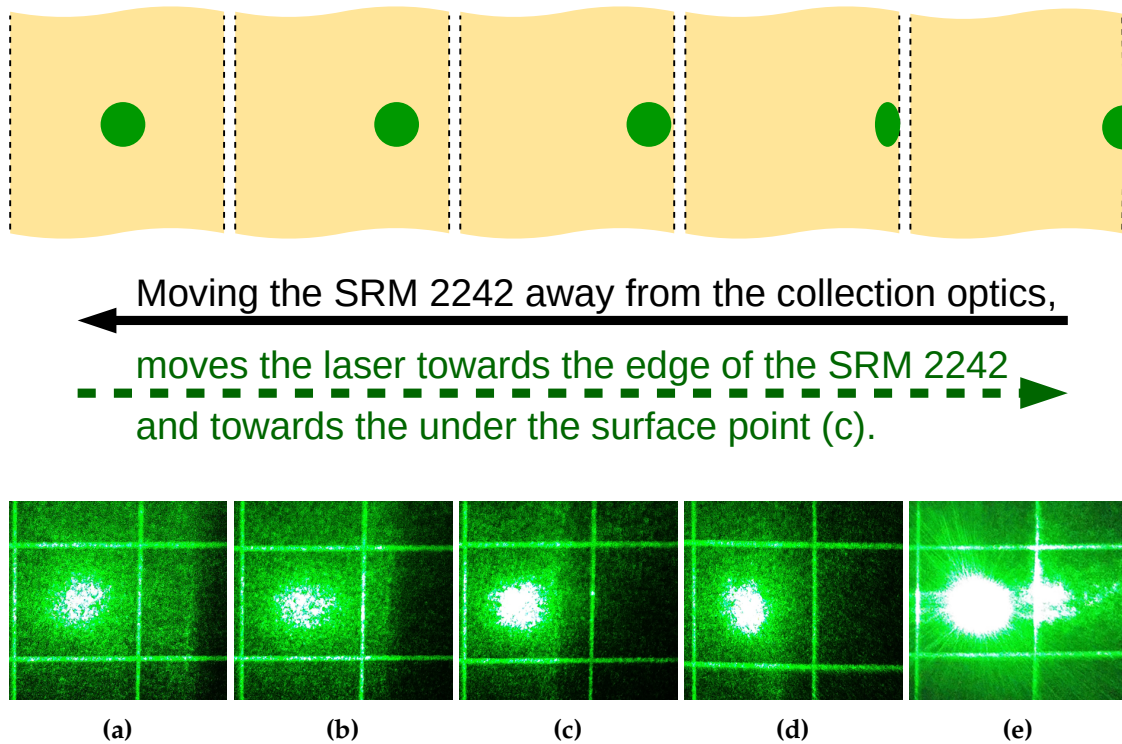


Figure 4.3: Camera images and sketches of the laser dot passing through the SRM 2242 at different lateral positions. These camera images show the successive movement of the SRM relative to the laser beam. The sketches show the whole SRM 2242 cross-section with an indication of the laser position corresponding to the camera image underneath. In the laboratory frame of reference the SRM 2242 is moved away from the collection optics. In the SRM 2242 frame of reference the laser moves towards the edge. Image (a) shows the laser passing through the centre of SRM 2242. Image (b) displays the SRM 2242 slightly moved. Image (c) corresponds to the under the surface position. In image (d) the inner edge the SRM 2242 is slightly touched by the laser beam. In image (e) the laser hits the edge of the plate directly. The images are recorded with a digital microscope and the perspective is corrected manually using image editing software.

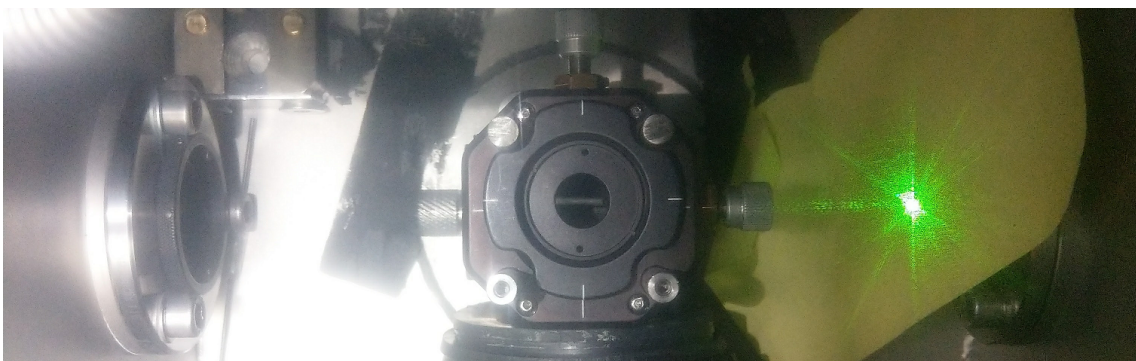


Figure 4.4: Calibration cell and the alignment screen inside the glove box. Setup of the screen (piece of paper) and calibration cell for measurements with the KATRIN LARA system. The image is taken through the top window. More details can be found in the main text.

4.4 Systematic investigations of the SRM 2242 with the test system

As described in section 3.3 the SRM 2242 is not used as intended by NIST. Instead of the front surface, the laser enters the SRM 2242 on one of the lateral sides. However, the lateral sides are not polished by NIST. The SRM 2242 lateral surfaces need to be polished at KIT⁴ in order to keep the laser beam collimated when entering the SRM 2242. At the time of this work three SRM 2242 (Fig. 4.5) are available at TLK. All three were polished, but have a different history:

- **'SRM1'** is the oldest standard and the only standard with a polished and frosted front surface. It was used for at least five years. Using this standard, the investigations in [Rup12, Sch13a, Sch15a] were performed. It was partly stored in a dry protective atmosphere, but was also exposed to the laboratory atmosphere for an indefinite period of time.
- **'SRM2'** was stored in the nitrogen atmosphere of the glovebox for at least three years for test measurements. For this work, it was removed from the glovebox and in contact with the laboratory atmosphere. Both front surfaces of this standard are polished by NIST.
- **'SRM3'** was delivered by NIST in October 2016 and has been originally packed since then. In the context of this work, it was unpacked and the lateral surfaces for the laser beam were polished. In the process, the standard was slightly damaged so that a small piece is missing. It has been exposed to the laboratory atmosphere ever since.

The polishing and the different histories of the standards raise two issues:

- NIST does not specify a height at which the laser must hit the SRM 2242, because of the high quality of their polishing. Since the laser in the KATRIN application hits the lateral surface and the lateral surfaces have been subsequently polished, a dependence on the laser height could arise. There is a possibility that the polished surface is not uniform enough for the calibration.
- NIST states that the SRM 2242 has to be kept in a dry atmosphere and handled with care. Neither of the three standards was exclusively stored in dry atmosphere and all of them were mechanically polished, SRM3 was damaged during the polishing. It has to be demonstrated that the standards can still be used for the calibration.

These issues are investigated in section 4.4.1 and section 4.4.2 using the developed alignment procedure and the LARA test system. These investigations have to be performed with the test system, because of the restricted space in the glovebox environment of the KATRIN LARA system. Additionally, in section 4.4.3 the achievable reproducibility of the alignment procedure with the test system is demonstrated.

⁴The polishing was carried out at the glass apparatus design workshop at the Institute of Catalysis Research and Technology (IKFT) at KIT.

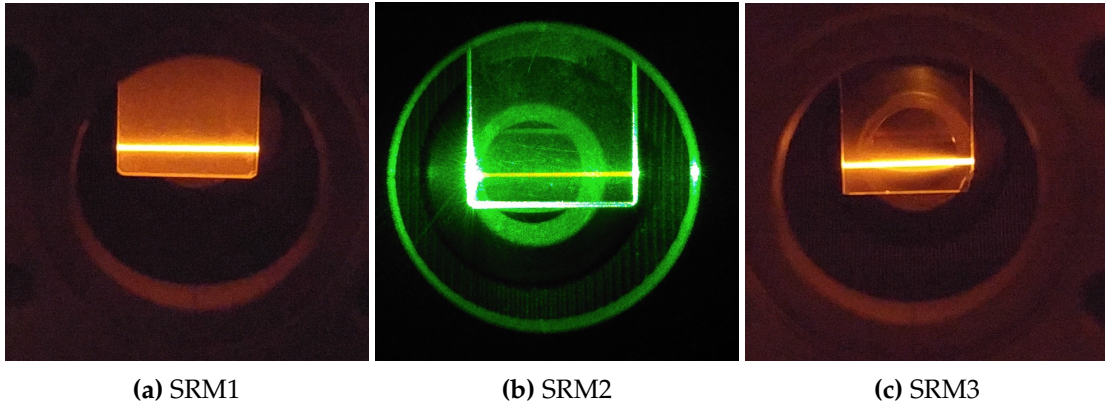


Figure 4.5: Images of three different SRM 2242 in comparison. (a) The frosted front side of SRM1 is visible. The image is taken through a filter for green wavelengths. The visible line is the emitted SRM spectrum. (b) This image of SRM2 is taken without a filter. The green line the laser beam passing through the standard. (c) The lower right corner of SRM3 is damaged, but the laser beam hits above the damaged part. The image is taken through a filter for green wavelengths. The visible line is the emitted SRM spectrum. All three standards have polished entry and exit (lateral) surfaces for the laser beam.

4.4.1 Influence of the vertical position of the SRM 2242 relative to the laser beam

In order to obtain an estimate of the influence of the relative laser height, the SRM1 was positioned with the laser beam hitting below the surface. Then the height of the SRM1 was changed twice by about 1 mm without changing the lateral positioning. The data analysis chain is shown in Fig. 4.6. First, the measured background is subtracted from the measurement of the SRM 2242. Then, from the measured intensity curves $I_{j,\text{meas}}^{(i)}(x)$ the spectral sensitivity is calculated

$$\eta_j^{(i)}(x) = \frac{I_{j,\text{meas}}^{(i)}(x)}{I_{\text{NIST}}} \quad (4.1)$$

in every CCD bin (i) with the normalization point at 624 nm. The resulting three spectral sensitivity curves $\eta_j^{(i)}(x)$ are shown in Fig. 4.7 for bin 10 and Appendix A.1 for all bins.

In addition, the relative standard uncertainty⁵ was calculated according to

$$u_{\text{rel},z}^{(i)}(\eta) = \frac{u_z(\bar{\eta}^{(i)}(x))}{\bar{\eta}^{(i)}(x)} = \frac{t_{p=68.27\%}}{\bar{\eta}^{(i)}(x)} \sqrt{\frac{1}{n \cdot (n-1)} \sum_{j=1}^n \left(\eta_j^{(i)}(x) - \bar{\eta}^{(i)}(x) \right)^2}, \quad (4.2)$$

where $\bar{\eta}^{(i)}(x) = \frac{1}{n} \sum_{j=1}^n \eta_j^{(i)}(x)$ is the average⁶ spectral sensitivity in any given bin (i), t_p is the Student's t-factor⁷ and n the number of measurements. In Fig. 4.8 the calculated

⁵An in-depth introduction to uncertainty calculation is given in chapter 5.

⁶See footnote 5.

⁷See footnote 5.

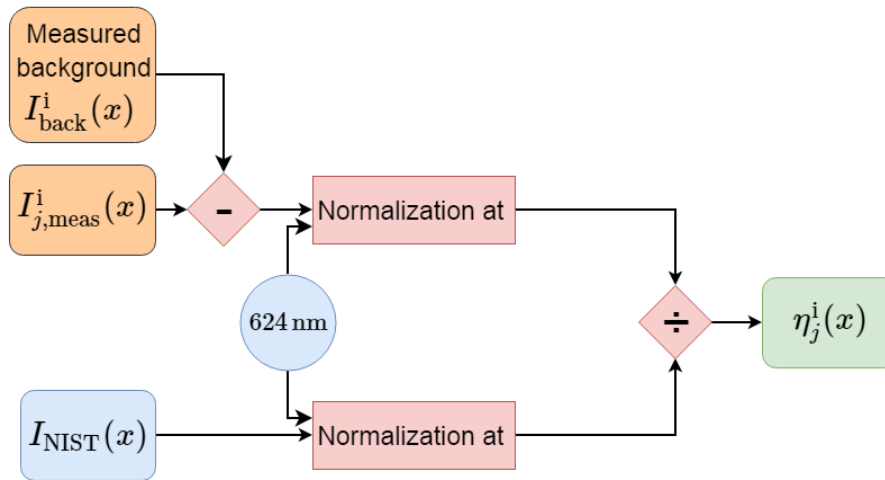


Figure 4.6: Schematic illustration of the data analysis of SRM 2242 measurements with the test system. From the measured intensity spectra the corresponding measured background is subtracted. Then, both the intensity from NIST and the measured intensity are normalized at the same wavelength. After the normalization the spectral sensitivity is calculated. This is performed for every vertical bin (i) of the CCD. Measured input quantities are shown in orange, predefined input quantities in blue, data operations in red and output quantities in green.

standard uncertainty is compared with the uncertainty data from NIST. For the three different vertical positions of the SRM 2242 the spectral sensitivity curves show a good agreement in all bins.

Discussion of the results

The relative standard uncertainty is not dependent on the CCD bin (i). This implies that the standard uncertainty is dominated by noise, rather than systematic effects. Also, the relative standard uncertainty of the measurements is in the same order of magnitude as the uncertainties specified by NIST. This is only expected, if the SRM 2242 does not show any defects on the lateral surfaces due to the polishing and handling. This means that the polishing is of sufficient quality for the calibration.

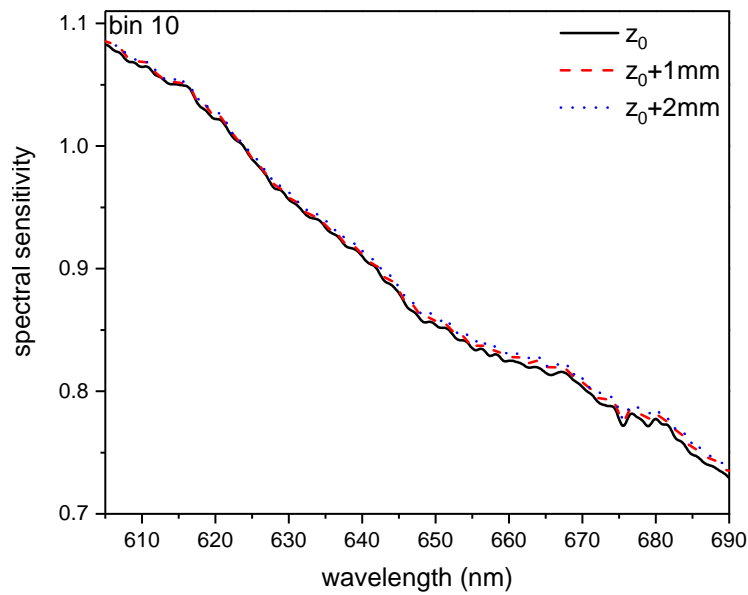


Figure 4.7: Spectral sensitivity as a function of the vertical position of the SRM 2242. Using the alignment procedure the standard was positioned with the laser beam hitting directly under the surface. Without changing the lateral position, the vertical position of the SRM 2242 was changed twice by about 1 mm. The three resulting spectral sensitivity curves show good agreement.

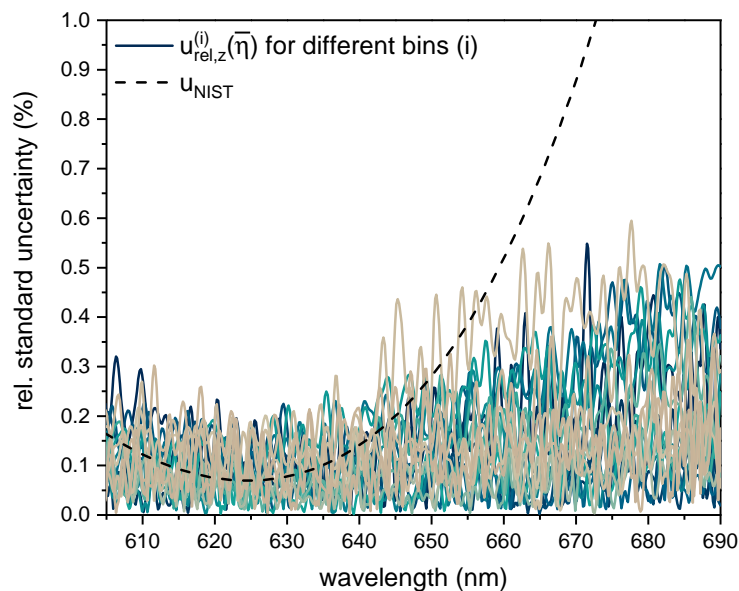


Figure 4.8: Relative standard uncertainty of the spectral sensitivity for different vertical positions of the SRM 2242 in all bins of the CCD. Calculated from the data shown in Appendix A.1 and Fig. 4.7. The relative 2σ uncertainty from NIST is corrected to correspond to relative 1σ uncertainty. The colours range from dark blue for bin 1 to grey for bin 20.

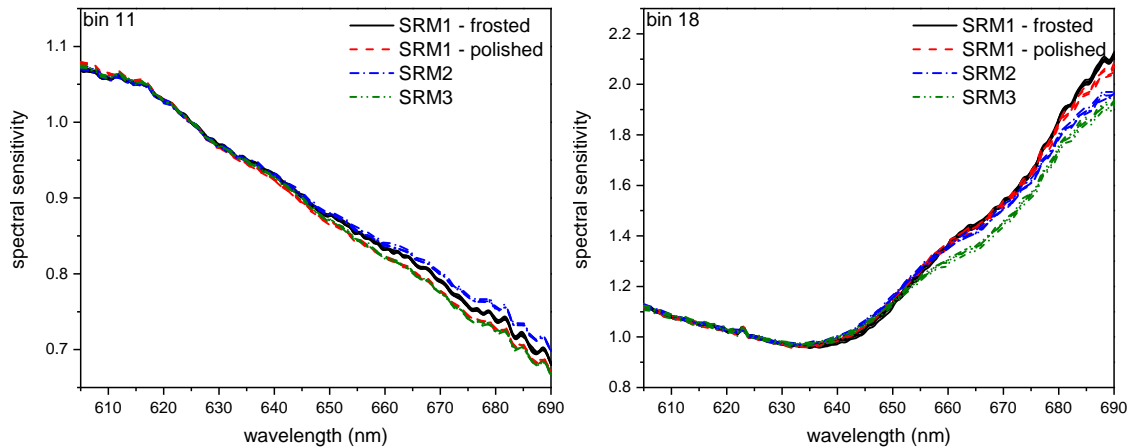


Figure 4.9: Spectral sensitivity determined with three different SRM 2242. Using the developed alignment procedure the SRM 2242 standards were positioned with the laser beam hitting directly under the surface. The resulting spectral sensitivity curves show overall good agreement. *left:* In bin 11 a systematic shift in the region about 650 nm is visible. However, the impact of the shift is negligible (See Fig. 4.10). *right:* A larger deviation is only visible in bins with insufficient irradiation like bin 18. These bins are not used for Raman measurements.

4.4.2 Comparison of three different SRM 2242

For the following measurements, each standard was positioned in the laser beam using the alignment procedure. For SRM2, SRM3 and the polished side of SRM1 four independent repositions were performed and the spectra measured. Additionally, the spectrum from the frosted side of SRM1 was measured five times. From these measurements the spectral sensitivity curves (see Eq. 4.1) were calculated with a normalization point of 624 nm (same data processing as in section 4.4.1, shown in Fig. 4.6). The comparison of the curves is shown in Fig. 4.9 for two bins and Appendix A.2 for all bins. In most bins a good agreement is visible for the spectral sensitivities determined with different standards. Only bins with a insufficient irradiation⁸ (like bin 1, 12, 18) show a stronger deviation. In some bins (like bin 11) a systematic shift is visible in the region > 650 nm. However, this shift is never associated with a relative standard uncertainty (calculated according to Eq. 4.2) bigger than 1 % (Fig. 4.10).

Discussion of the results

In case the properties of the SRM 2242 standards have not changed as a result of the polishing treatment and handling, then all three should emit the same calibration spectrum with the under the surface positioning. All possible configurations of the three SRMs show a good agreement with a relative standard uncertainty < 1 %. This is an important finding, because NIST recommends storing the SRM 2242 in a dry atmosphere. However, the properties of the three SRM 2242 plates have apparently not changed significantly due to their different pre-histories and ages. Therefore, any of the three standards can be used for the calibration. SRM2 was selected for all subsequent measurements with the KATRIN

⁸Since the used optical fibre bundle is of type slit-to-slit unordered, the bins cannot be assigned to the respective region on the CCD. Bins with insufficient irradiation are not used for any Raman measurements.

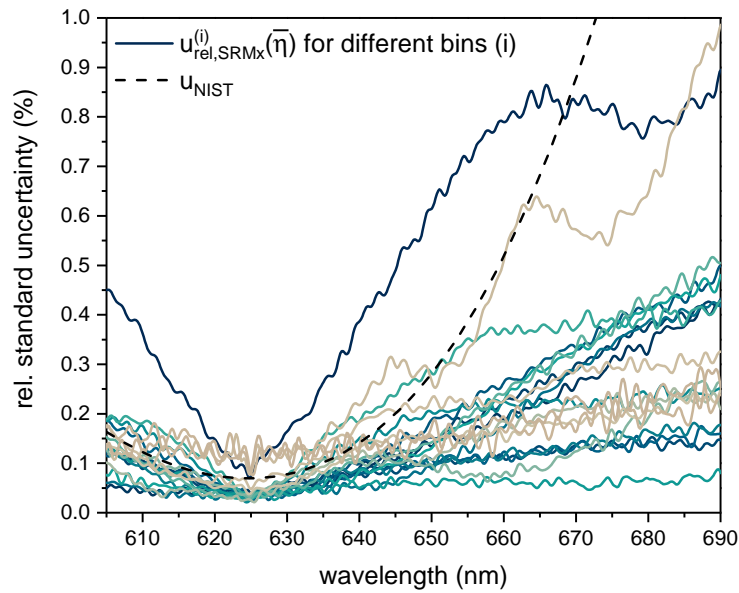


Figure 4.10: Relative standard uncertainty of the spectral sensitivity of three different SRM 2242 in all bins of the CCD. Calculated from the data shown in Appendix A.2 and Fig. 4.9. The relative 2σ uncertainty from NIST is corrected to correspond to relative 1σ uncertainty. The colours range from dark blue for bin 1 to grey for bin 20.

LARA system, because it was already radioactively contaminated, both front surfaces are polished and it is not damaged.

4.4.3 Demonstration of the achievable reproducibility

As a final measurement with the test system the achievable reproducibility of the alignment procedure is demonstrated. The SRM2 was positioned 27 times by means of the alignment procedure. Additionally, after a random number of measurements the SRM2 plate was rotated, so the other front surface faces the collections optics. The measurements are analysed according to Fig. 4.6. The spectral sensitivity curves are displayed in Fig. 4.11 for two bins and in Appendix A.3 for all bins. In some bins (like bin 6) the curves split into two groups, while in other bins (like bin 10) this effect is not visible. The relative standard uncertainty cannot be calculated according to Eq. 4.2 when the measurements are split into two groups. Therefore, the relative maximum difference

$$\Delta_{\text{rel}}^{\text{max,(i)}} = \frac{|\eta_{\text{max}}^{(i)}(x) - \eta_{\text{min}}^{(i)}(x)|}{\bar{\eta}^{(i)}(x)} \quad (4.3)$$

between the curves is calculated in every bin (i) as an estimate⁹ of the reproducibility and shown in Fig. 4.12. In bins with sufficient irradiation the relative maximum difference is well below 5%.

Discussion of the results

The spectral sensitivity curves show good agreement with a relative maximum difference smaller than 5% over the total relevant range of [610 nm : 690 nm] in all bins with sufficient irradiation. Therefore, it is verified that the calibration procedure is able to reliably and reproducibly find the point just under the surface of the SRM 2242 with the test system. The reason for the splitting into two groups in some bins is unknown. However, most probably it is caused by an effect associated with a different granularity of the optical fibre bundle and the SRM 2242 spectrum.

⁹The relative maximum difference overestimates the relative standard uncertainty.

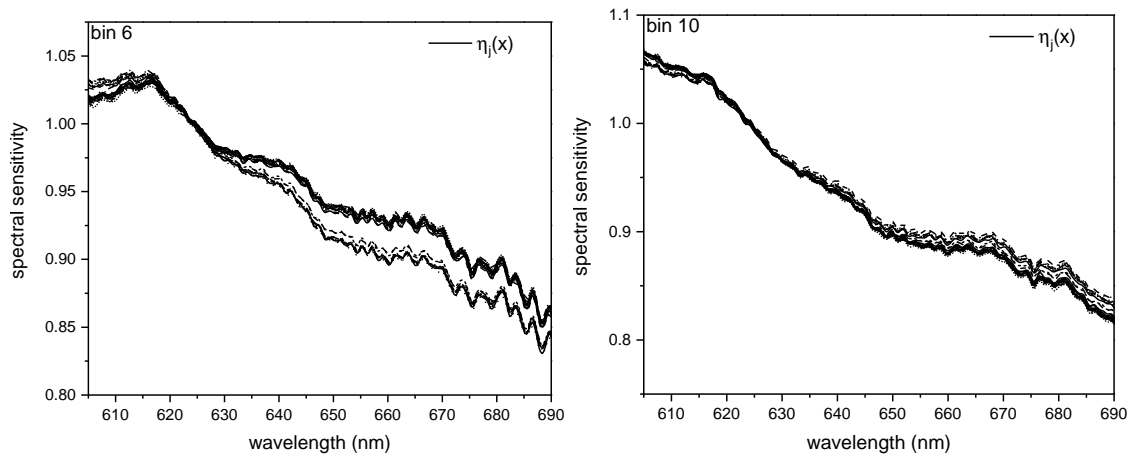


Figure 4.11: Spectral sensitivity determined with multiple repositionings of the SRM 2242. Using the alignment procedure the SRM 2242 standard was positioned 27 times with the laser beam hitting directly under the surface. *left:* In some bins the measurement curves split into two groups. *right:* Other bins show a good agreement.

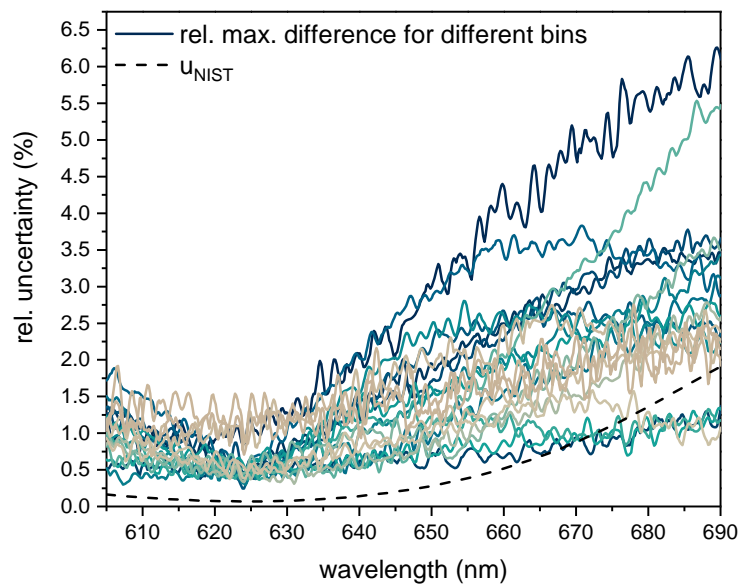


Figure 4.12: Relative maximum difference of the spectral sensitivity curves of multiple repositionings of the SRM 2242 in all bins of the CCD. Calculated from the data shown in Appendix A.3 and Fig. 4.11. The relative 2σ uncertainty from NIST is corrected to correspond to relative 1σ uncertainty. The colours range from dark blue for bin 1 to grey for bin 20.

4.5 Calibration of the KATRIN laser Raman system

For the measurements with the KATRIN LARA system, SRM2 was brought into the glovebox. The acquisition time was increased¹⁰ to 300 s in order to reduce noise. Also, for each positioning of the SRM 2242 the intensity spectrum was measured with $\pm 45^\circ$ polarizations relative to the standard polarization, which is perpendicular to the breadboard surface. This is also shown in the corresponding illustration data analysis chain (Fig. 4.13). These two intensity spectra are averaged before they are used to calculate the spectral sensitivity. The point of normalization is at 624 nm. In total 13 measurements were conducted, eight of them with a different screen (yellow paper (visible in Fig. 4.4)) in comparison to the black aluminium screen in Fig. 4.2.

4.5.1 Quantifying the reproducibility of the alignment procedure inside the glovebox

The 13 spectral sensitivity curves are displayed in Fig. 4.14 for bin 10 and bin 13 and in Appendix A.4 for all bins. In all bins the measurements split up into two groups. In some bins (like bin 10) the difference between the groups is of about 0.1, while in other bins (like bin 13) the difference is smaller than 0.01, but still visible. An analysis of the data shows that one group corresponds to the measurements with the paper screen and the other group to the measurements with the blackened aluminium screen.

Since the curves split up into two groups, they do not follow a Gaussian distribution and the determination of the standard uncertainty becomes more complicated and will be

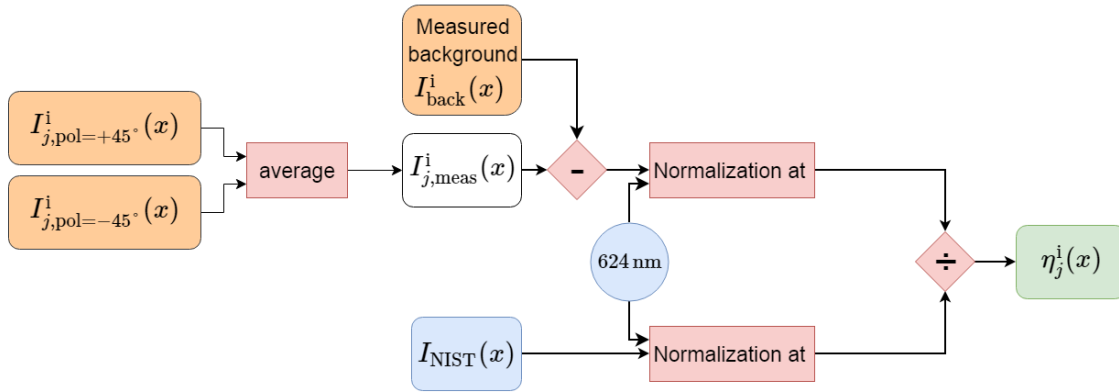


Figure 4.13: Schematic illustration of the data analysis of SRM 2242 measurements with the KATRIN LARA system. The SRM 2242 intensity is measured for two different polarisations. The average of the two measurements is calculated. From the averaged intensity spectra the corresponding measured background is subtracted. Then, both the intensity from NIST and the measured intensity are normalized at the same wavelength. After the normalization the spectral sensitivity is calculated. This is performed for every vertical bin (i) of the CCD. Measured input quantities are shown in orange, predefined input quantities in blue, data operations in red and output quantities in green.

¹⁰Compared to the acquisition time of 35 s in section 4.4.

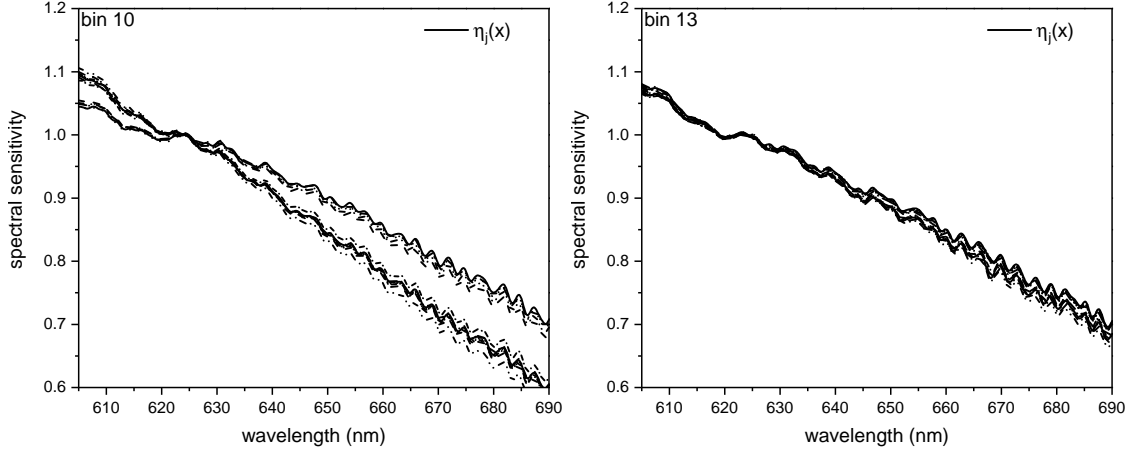


Figure 4.14: Spectral sensitivity of the KATRIN LARA system determined with multiple repositionings of the SRM 2242 inside the glove box. Using the developed alignment procedure the SRM 2242 was positioned with the laser beam hitting directly under the surface. The resulting spectral sensitivity curves slit up into 2 groups. *left:* In bin 10 the difference between the groups is up to 0.1, which is about 10 % difference. *right:* In bin 13 the maximum difference is smaller than 0.01. The origin of the difference between bins is not clear.

calculated in the next chapter. As an estimate for the reproducibility the relative maximum difference

$$\Delta_{\text{rel}}^{\text{max},(i)} = \frac{|\eta_{\text{max}}^{(i)}(x) - \eta_{\text{min}}^{(i)}(x)|}{\bar{\eta}^{(i)}(x)} \quad (4.4)$$

between the curves is calculated for every relevant bin (bin 2-17). The results are shown in Fig. 4.15 and compared with the 1σ uncertainty from NIST. For further investigation of the splitting into groups the the average spectral sensitivity of the bins 2-17 was calculated for every measurement j

$$\eta_j^{\text{bin-average}}(x) = \frac{1}{16} \sum_{i=2}^{17} \eta_j^{(i)}(x). \quad (4.5)$$

The relative maximum difference

$$\Delta_{\text{rel}}^{\text{max,bin-average}} = \frac{|\eta_{\text{max}}^{(\text{bin-average})}(x) - \eta_{\text{min}}^{(\text{bin-average})}(x)|}{\bar{\eta}^{(\text{bin-average})}(x)} \quad (4.6)$$

between these 27 bin-averaged curves is shown in Fig. 4.15.

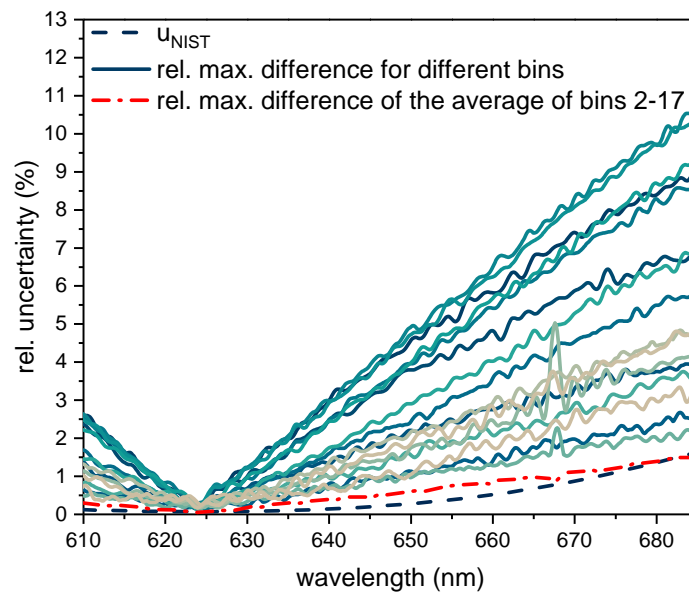


Figure 4.15: Relative maximum difference of the spectral sensitivity of the KATRIN LARA system in the relevant bins of the CCD. Calculated from the data shown in Appendix A.2 and Fig. 4.14. The relative 2σ uncertainty from NIST is corrected to correspond to relative 1σ uncertainty. The colours range from dark blue for bin 2 to grey for bin 17.

4.5.2 Discussion and consequences for the KATRIN experiment

Although the relative maximum difference of the measurements cannot be directly compared the relative standard uncertainty from NIST, it provides an estimate and can help to identify some problems. The relative maximum difference per bin (i) is about an order of magnitude bigger than the uncertainty from NIST.

The difference between the two groups as seen in Fig. 4.14 seems to be rather overwhelming (up to 10%) and connected to the type of chosen screen. However, it should be noted, that the strong difference disappears when the average over the whole chip (all relevant bins) is calculated (shown in Fig. 4.15 in red). It is assumed that the SRM 2232 emission has a small granularity which leads to a spatially pronounced emission. Apparently, the different alignment measurements sample this granularity with a small spatial offset on the optical fibre bundle, due to an optical offset. If, instead the complete SRM 2242 spectrum on all fibres is obtained by averaging (or within the full LARASoft analysis routine), this granularity is averaged out and the same total SRM 2242 spectrum is obtained. For the averaged SRM 2242 spectrum the relative maximum difference is below 1%.

In summary, the splitting into groups on the bin-level suggests that, depending on the type of screen, a slightly different point appeared to be the desired under the surface spot. However, the analysis of the average of the whole CCD shows, that the difference yields from an optical offset between the optical fibres and the SRM 2242 and will also disappear during the full LARASoft analysis routine.

(i) Nevertheless, the measurements with the paper screen were much more difficult to perform. The laser dot appeared brighter than on the blackened aluminium screen. This caused an oversaturation of the camera and the laser dot could not be observed with the naked eye. Additionally, while the blackened aluminium screen is sturdy and creates a flat and even surface for the image of the laser dot, the paper screen is flexible and causes distortions due to the uneven surface.

Recommendation: For future calibrations of the KATRIN LARA system it is strongly recommend to use an alignment screen made of black anodized aluminium. This makes the alignment procedure is easier and more reliable.

(ii) For the alignment of the SRM 2242 in the test system every tested camera proved to work. For the alignment inside the glovebox non of them were suitable. There are three main reasons:

- The distance between the screen and the camera cannot be changed. Obviously, the camera cannot get closer than the top window of the appendix. However, the camera cannot be moved further away either, because the window is scratched heavily. This fixes the distance between camera and screen to about 20 cm and it has to be place directly on top of the window. In the test system the distance could be adjusted as desired and the optimal setting was much closer to the screen.
- The angle of the screen in the glovebox causes the shape of the laser dot to be distorted due to the perspective when viewed directly from the top down. It is not easy to adjust the camera angle respectively and still get a usable image, due to the scratches on the appendix window.

- The diameter of the focussed laser beam of the KATRIN LARA system is significantly smaller than the diameter achieved in the test system. Additionally, there is no space in the glovebox to place the screen at a distance corresponding to the focal length of the focussing lens ($f = 250$ mm) or further. Therefore, the image of the laser dot on the screen is smaller and brighter, when compared to the image that can be seen with the test system. Every used camera is oversaturated by the brightness of the dot and a brightness adjustment with a neutral density filter does not help with the smallness of the dot.

Recommendation: The observation of the laser dot shape can be performed with the naked eye¹¹ and works well as shown by the measurements in section 4.5.1. However, a suitable camera would make the observation easier and recordable. It should be considered to find a suitable camera with consideration to the three points mentioned above.

(iii) In order to obtain a statistically meaningful result and calculate the standard uncertainty, the alignment procedure and spectral sensitivity measurement should be performed multiple times.

Recommendation: At least $n = 10$ repositionings and measurements of the SRM 2242 should be performed for the calibration of the KATRIN LARA system.

(iv) One of the unanswered question of this work is whether the calibration is stable over time or whether it needs to be redone repeatedly. Immediately after the measurements in section 4.5.1 a long time¹² stress test of the KATRIN LARA system was started to ensure that the KATRIN LARA system is ready for the KATRIN measurements starting in summer 2018. After the stress test the system can be recalibrated and the results compared to the shown results.

Recommendation: As for now the KATRIN LARA system should be calibrated once in every maintenance phase of KATRIN.

(v) The SRM 2242 is certified for use in a temperature range of $20^{\circ}\text{C} - 25^{\circ}\text{C}$. During the measurements in this work it was ensured from time to time that the temperature in the glovebox is within this range. However, the temperature sensor is not close to the appendix, where the calibration cell is located.

Recommendation: The temperature value needs to be checked, when the system is calibrated and the shift from NIST applied, if the temperature is not within the given range. It could be considered to add a temperature sensor which is closer to the appendix inside the glove box to get a more accurate temperature measurement.

Finally, it should be noted that in section 4.5.1 only the relative maximum difference of the spectral sensitivity measurements was calculated. The standard uncertainty of the alignment procedure has to be calculated. In addition, it is not clear how the uncertainty of the alignment procedure effects the KATRIN relevant measurands. In the next chapter it will be determined if the achieved reproducibility is sufficient to fulfil the KATRIN requirements under consideration of the full analysis routine.

¹¹With the paper screen a neutral density filter has to be used to adjust the brightness.

¹²A duration of two months is planned.

Chapter 5

Calculation of the uncertainty budget of the laser Raman source monitoring system

5.1 Motivation

In the previous chapter it could be shown that the developed alignment procedure provides results with a relative maximum difference better than 10 % in the relevant wavelength range from 610 nm to 685 nm across all CCD bins (i). However, it is necessary to investigate whether the KATRIN requirements for trueness can be met regarding the relevant quantities:

$$\frac{\Delta\epsilon_T}{\epsilon_T} \leq 0.03 \hat{=} 3\% \quad (5.1)$$

and

$$\frac{\Delta\kappa}{\kappa} \leq 0.1 \hat{=} 10\%. \quad (5.2)$$

In addition to the previously introduced physical uncertainty sources, the data analysis by the software, as well as possible correlations need to be taken into account. Only then it is possible to make a statement for the KATRIN operation requirements.

In section 5.2 the 'Guide to the Expression of Uncertainty in Measurement' (GUM), the nomenclature it contains and the procedure used for uncertainty calculation, are described briefly. The GUM process is then used in section 5.3 to calculate the standard uncertainty of the spectral sensitivity measurements shown in section 4.5.1. In section 5.4 the uncertainty budget of the KATRIN LARA system is determined. First, in section 5.4.1 the measurement and the analysis chain is described. Second, the uncertainties and correlations caused by the spectral sensitivity correction (section 5.4.2) are examined in detail. Third, in section 5.4.3 other possible sources for uncertainties of the LARA measurement are identified and discussed. Finally, in section 5.4.4 follows a summary of the results and the uncertainty budget.

5.2 Introduction to uncertainty calculation according to the Guide to the Expression of Uncertainty in Measurement

The GUM describes standardised and internationally recognised methods and procedures for handling uncertainties and proper uncertainty propagation. The nomenclature relevant to this work and the basics of the procedure will be briefly described in this section. Further information can be found in [JCG08], [Sch15b].

Based on [Sch15b] the calculation of the uncertainty budget according to the GUM can be described as a seven-step process. The basics of the process are summarized in Fig. 5.1.

- **Step 1:** The basic description of the measurement procedure.
- **Step 2:** Description of the model for the evaluation. The model will typically contain a formula combining all the input quantities.
- **Step 3:** Every available information about the input quantities is collected. The GUM framework distinguishes between two types of uncertainties, called type A and type B. Type A uncertainties are all uncertainties determined by repeated measurements. The necessary measurements for all type A uncertainties should be performed in this step. All other uncertainties, from e.g. calibration certificates, previous measurements and general knowledge, are of type B. There is no difference in nature of the two types of uncertainties, but they require different statistical treatments.
- **Step 4:** The acquired information is used to calculate the standard uncertainty of each input quantity following a fixed set of rules.

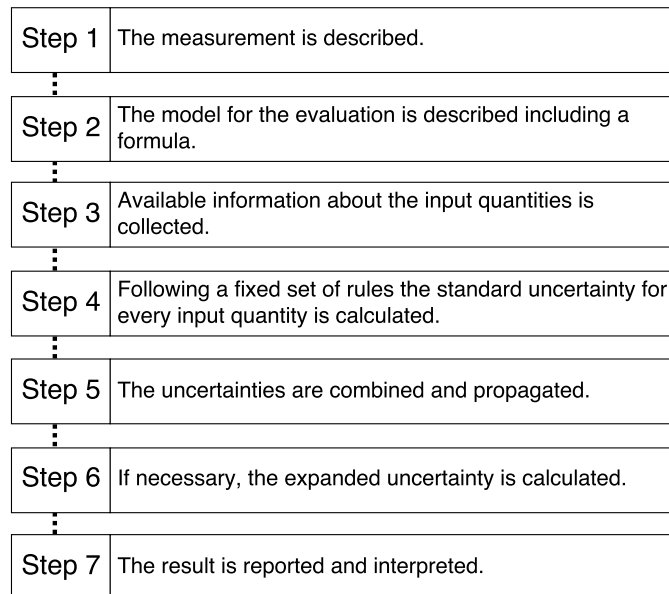


Figure 5.1: Illustration of the GUM seven-step process for uncertainty calculation. Detailed information on every step can be found in the main text. Based on [Sch15b].

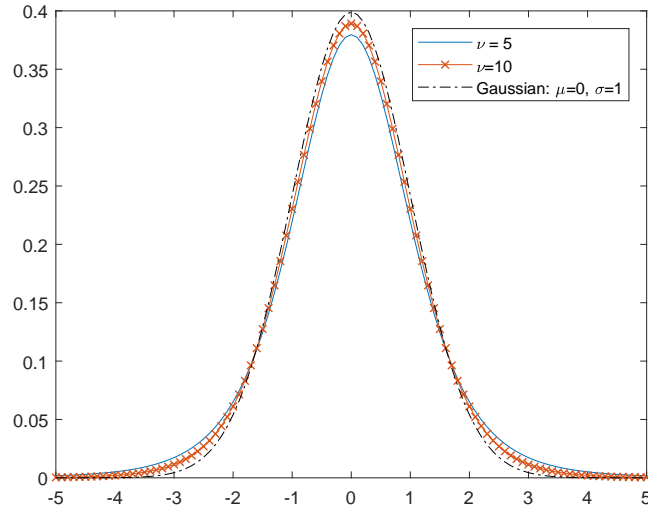


Figure 5.2: Comparison of the Student's distribution for different degrees of freedom and a Gaussian distribution. For large degrees of freedom $\nu = n - 1$ the Student's distribution approaches the Gaussian distribution. The plots are created using Matlab R2017a.

First, for uncertainties of type A the arithmetic mean/average \bar{q} of the measurements q_j is calculated by

$$\bar{q} = \frac{1}{n} \sum_{k=1}^n q_k. \quad (5.3)$$

Here, n is the number of measurements q_j . Second, the standard uncertainty¹ of the mean is calculated

$$u(\bar{q}) = \sqrt{\frac{1}{n \cdot (n - 1)} \sum_{j=1}^n (q_j - \bar{q})^2}. \quad (5.4)$$

However, generally measurements follow the Student's distribution for small $n < 40$. The Gaussian distribution is the function limit of the Student's distribution for large $n \rightarrow \infty$. For visualization the Student's distribution for different degrees of freedom $\nu = n - 1$ and a Gaussian distribution are shown in Fig. 5.2. Third, the standard uncertainty needs to be corrected with the $t_p(\nu)$ - factor from the Student's distribution

$$u(\bar{q})_t = t_p(\nu) \cdot u(\bar{q}). \quad (5.5)$$

The $t_p(\nu)$ - factor can be found in various tables [Sch15b] or calculated² (see Tab. 5.1). It depends on the coverage probability p and the degrees of freedom ν . The coverage probability is the percentage of times that the true value Y_{true} lies within the

¹The given formula is only valid, if the measured q_j follow a Gaussian/Student's distribution. In case they do not a different approach has to be used.

²Many programs for data analysis have an implemented function for the calculation e.g. Microsoft Excel, Matlab or LibreOffice Calc.

confidence interval defined by

$$\bar{y} \pm u(\bar{y})_t. \quad (5.6)$$

For the calculation of type B uncertainties often calibration certificates will provide the standard uncertainty. However, the given uncertainty can be an expanded uncertainty

$$U_p = k_p(\nu) \cdot u \quad (5.7)$$

with a coverage factor $k_p \neq 1$. The k_p -factor extends the given standard uncertainty to different coverage probabilities (e.g. $k = 1$ corresponds to a coverage probability of $p = 68.27\%$ and $k = 2$ to $p = 95\%$). Additionally, in some cases the uncertainty is given for e.g. a rectangular distribution rather than a Gaussian distribution and needs to be corrected

$$u_{\text{Gaussian}} = \frac{1}{\sqrt{G}} \cdot u_{\text{non-Gaussian}} \quad (5.8)$$

with the appropriate weighting factor G [Sch15b]. These corrections ensure that every calculated standard uncertainty corresponds to the same coverage interval of a Gaussian distribution.

- **Step 5:** The uncertainties of the input quantities x_i are propagated to the relevant output quantity y . Uncorrelated uncertainties can be combined according to

$$u_c(y) = \sqrt{\sum_i (c_i \cdot u(x_i))^2}, \quad (5.9)$$

where c_i is the sensitivity coefficient

$$c_i = \frac{\partial f}{\partial X_i}. \quad (5.10)$$

- **Step 6:** If necessary the expanded uncertainty is calculated

$$U_p(y) = k_p(\nu) \cdot u_c(y) \quad (5.11)$$

- **Step 7:** Finally, the result is reported in the form

$$Y = y \pm U \quad \text{with} \quad k, \quad (5.12)$$

where Y is the measurand and y the best estimate of the measurand, which is typically the average.

Table 5.1: Student's $t_p(\nu)$ -factor for different degrees of freedom and coverage probabilities. Calculated using the T.INV.2S-function in Microsoft Excel.

Degrees of freedom ν	$t_p(\nu)$			
	$p = 68.27\%$	$p = 90\%$	$p = 95\%$	$p = 99.73\%$
1	1.84	6.31	12.71	235.78
10	1.05	1.82	2.23	3.96
40	1.01	1.68	2.02	3.20
100	1.01	1.66	1.98	3.08

5.3 Uncertainty of the spectral sensitivity

In this chapter the uncertainty $u(\eta)$ of the spectral sensitivity η will be calculated following the framework provided by GUM. The measurements described in section 4.5.1 are used.

First, a short summary of the measurement and the evaluation model is given (steps 1 and 2 from the GUM process). Next, the collected information about the sources of uncertainty is presented, the standard uncertainties are calculated and combined (steps 3, 4 and 5). Finally, results are summarized and discussed (steps 6 and 7).

General description and model of the measurement

Since an in-depth description is already presented in section 4.5.1 and Fig. 4.13, only a short summary is given here. The measurement are performed with the KATRIN LARA system. By the means of the developed alignment procedure the SRM 2242 is placed in the laser beam path within the glovebox environment. The laser beam hits the SRM 2242 plate directly under the surface. Without moving the SRM 2242 two intensity spectra of the standard with different polarization settings of the $\lambda/2$ wavelength plate are measured. Every vertical bin (i) of the CCD is read out separately. These two spectra are averaged per bin

$$I_{\text{meas}}^{(i)}(x) = \frac{1}{2} \left(I_{+45^\circ}^{(i)}(x) + I_{-45^\circ}^{(i)}(x) \right). \quad (5.13)$$

This averaged spectrum corresponds to the certified spectrum from NIST and can be used for the spectral calibration of the laser Raman system. Therefore, the influence on the uncertainty of the polarisation and the positioning will not be considered separately. Every deviation from the correct position of either the SRM 2242 or the $\lambda/2$ wavelength plate will result in an uncertainty of the averaged emitted spectrum and finally the spectral sensitivity.

The measured spectrum and the spectrum provided by NIST are then both normalized at the same wavelength (624 nm) and the spectral sensitivity is calculated according to

$$\eta^{(i)}(x) = \frac{I_{\text{meas}}^{(i)}(x)}{I_{\text{NIST}}(x)}. \quad (5.14)$$

In total the SRM 2242 was repositioned and measured $n = 13$ times as described.

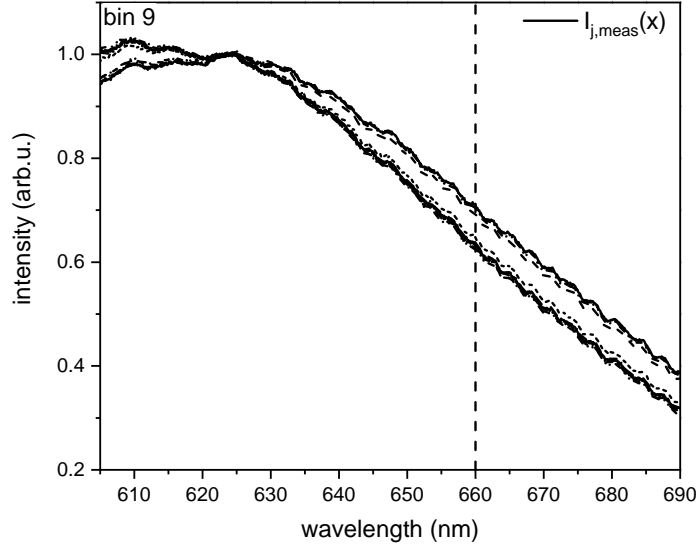


Figure 5.3: Measured and normalized intensity curves of the SRM 2242. The curves are normalized at 624 nm. Using the alignment procedure the standard was positioned with the laser beam hitting directly under the surface. The curves split up into two groups. The values along the dotted line at 660 nm are shown in Fig. 5.4.

Uncertainties of input quantities and combination of uncertainties

Calibration procedure For bin 9 the measured, averaged and normalized intensity is shown in Fig. 5.3. For the other bins in Appendix A.5. The distribution of the intensity spectra $I_{j,\text{meas}}(x)$ needs to be taken into account in order to calculate the standard uncertainty. As Fig. 5.4 and Appendix A.6 clearly shows, the intensity values do not follow a Gaussian distribution. The distribution is better described by a u-/arcsine-shape. According to [Sch15b] the standard uncertainty of a arcsine-distribution is given as:

$$u_x = \frac{\Delta a}{\sqrt{8}} = \frac{a_+ - a_-}{\sqrt{8}}, \quad (5.15)$$

where a_{\pm} are the minimum/maximum values of the arcsine-shape. Considering that $n = 13$ measurements were taken, the degree of freedom is $\nu = 12$ and therefore $t_{p=68.27\%} = 1.04$. The standard uncertainty of the measured intensity is

$$u_{I_{\text{meas}}}(x) = t_{p=68.27\%} \cdot \frac{|I_+(x) - I_-(x)|}{\sqrt{8}} = 1.04 \cdot \frac{|I_+(x) - I_-(x)|}{\sqrt{8}} \quad (5.16)$$

Using this equation the standard uncertainty is calculated for every bin and displayed for the bins 2-17³ in Fig. 5.5.

Uncertainty provided by NIST The only other input quantity is the NIST certified intensity spectrum. NIST provides relative 2σ uncertainty curves in polynomial form. From this

³As discussed in section 4.5 the bins 1, 18, 19 and 20 of the CCD used with the KATRIN LARA system are not illuminated sufficiently to be used for measurements.

information it is safe to assume that the uncertainty stems from a Gaussian distribution. The 2σ uncertainty corresponds to a coverage probability of $p = 95\%$ and a coverage factor $k_{p=95\%} = 2$. Using eq. 5.11 the relative standard uncertainty can be calculated

$$u_{I_{\text{NIST,rel}},k_{p=68.27\%}}(x) = \frac{1}{2} \cdot U_{I_{\text{NIST,rel}},k_{p=95\%}}(x). \quad (5.17)$$

To calculate the absolute standard uncertainty the averaged data \bar{I}_{meas} from the measurements in Fig. 5.3 is used. The absolute standard uncertainty is shown in Fig. 5.6 for the bins 2-17.

Combination of uncertainties These two input quantities for the spectral sensitivity cover different sources of uncertainties. NIST provides standard uncertainties, which occur in a 180° operation of the SRM 2242, while the uncertainties of the measured intensity determined in section 5.3 occur only in 90° operation. Therefore, there is no reason for the uncertainties to be correlated. They can be propagated to the spectral sensitivity by Eq. 5.4

$$u_{\eta,\text{comb}}(x) = \bar{\eta} \cdot \sqrt{\left(\frac{u_{I_{\text{NIST}}}(x)}{\bar{I}_{\text{meas}}}\right)^2 + \left(\frac{u_{I_{\text{meas}}}(x)}{\bar{I}_{\text{meas}}}\right)^2} \quad (5.18)$$

The combined uncertainty, for the bins 2-17 is shown in Fig. 5.7.

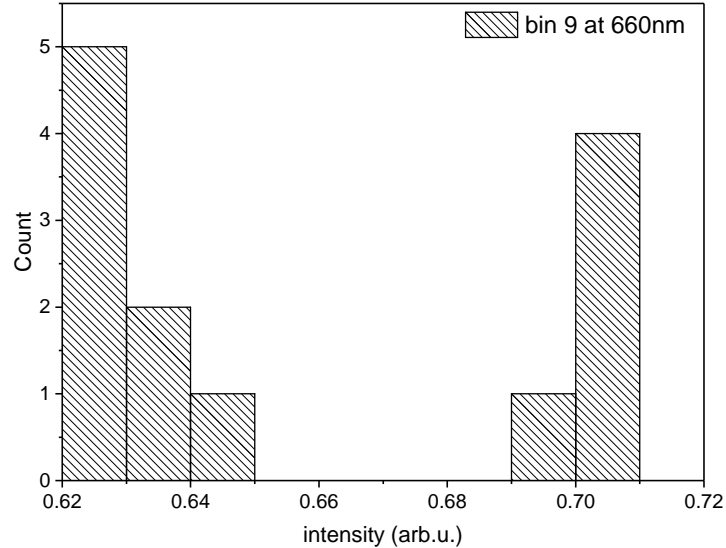


Figure 5.4: Histogram of the intensity values of the measured and normalized intensity curves of the SRM 2242 at 660 nm. The intensity values clearly do not follow a Gaussian distribution. The distribution can be described as u-/arcsine-shaped. The values are taken at the dotted line in Fig. 5.3.

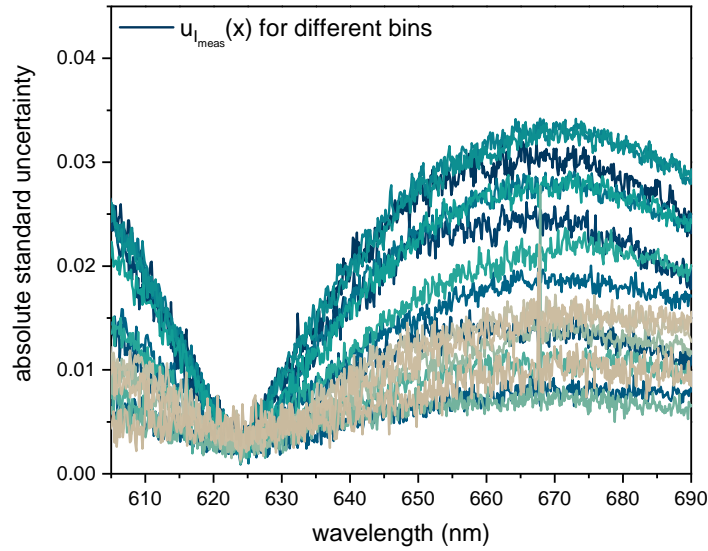


Figure 5.5: Standard uncertainty of the measured intensity in different bins. Calculated from the data shown in Fig. 5.3 using Eq. 5.15. The colours range from dark blue for bin 2 to grey for bin 17.

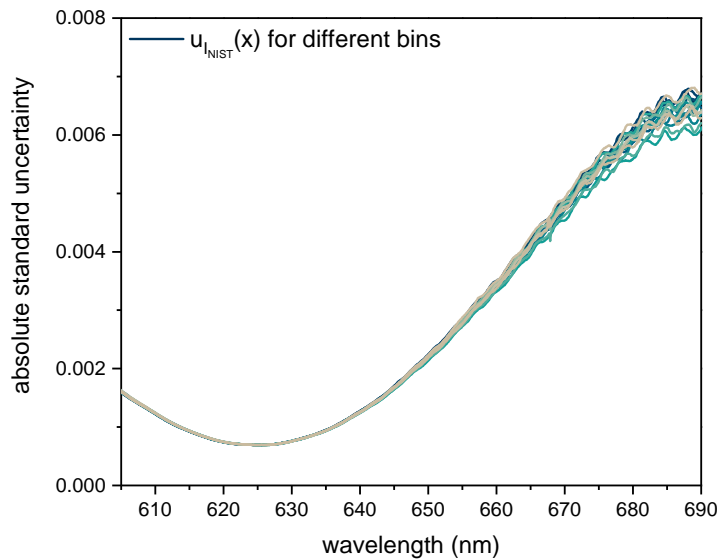


Figure 5.6: Standard uncertainty of the NIST certified intensity in different bins. The 2σ relative uncertainty from NIST is corrected to 1σ and using the mean \bar{I}_{meas} from Fig. 5.3 the absolute uncertainty is calculated for each bin. The colours range from dark blue for bin 2 to grey for bin 17.

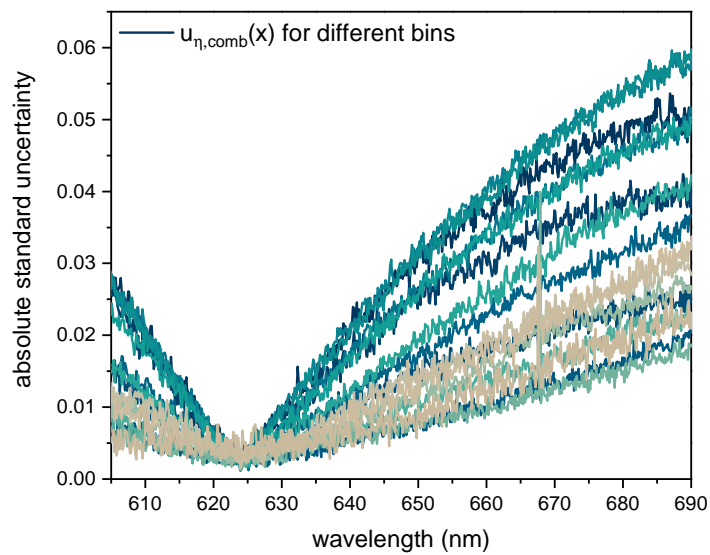


Figure 5.7: Standard uncertainty of the spectral sensitivity in different bins. Calculated from Fig. 5.5 and Fig. 5.6 and the mean $\bar{\eta}$ from the data shown in Appendix A.4. The colours range from dark blue for bin 2 to grey for bin 17.

Result and discussion

The spectral sensitivity

$$\eta(x) = \bar{\eta}(x) \pm u_{\eta,\text{comb}}(x) \quad (5.19)$$

is shown in Fig. 5.8 for one bin and in Appendix A.7 for all other bins. For KATRIN purposes a $p = 68.27\%$ coverage probability is sufficient, therefore the result does not need to be expanded. Comparing Fig. 5.5 and Fig. 5.6 shows that the uncertainty caused by the calibration procedure of the SRM 2242 surpasses the uncertainty provided by NIST by a order of magnitude and is the dominating uncertainty.

However, there are no direct requirements from KATRIN on the spectral sensitivity uncertainty. Therefore, in the next chapter it will be determined if the KATRIN requirements can be fulfilled with the achieved uncertainty of the spectral sensitivity.

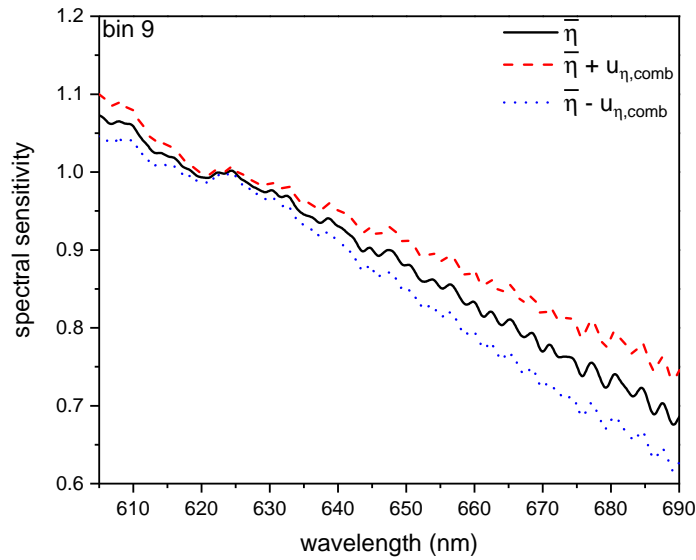


Figure 5.8: Spectral sensitivity with the combined standard uncertainty confidence interval in bin 9. Calculated using Fig. 5.7 and $\bar{\eta}$ from the data shown in Appendix A.4.

5.4 Uncertainty budget for the KATRIN laser Raman system

In the following chapter it will be determined how the uncertainty of the spectral sensitivity affects the KATRIN LARA results. This requires an in-depth look at the data analysis routine. Additionally, other possible sources of uncertainties are discussed.

5.4.1 General description of the measurement and model for the evaluation

The measurement task is to determine the gas composition in a measurement cell using the KATRIN LARA system. The measurand

$$N_x = \frac{S_x}{C \cdot \eta_x \cdot r_x} \quad (5.20)$$

is the number of atoms of a single constituent x and defined in Eq. 3.25. S_x is the measured Raman signal of each constituent, C is a constant, $\eta(x)$ is the spectral sensitivity of the Raman system and r_x is the theoretical intensity of every constituent as defined in Eq. 3.26. Using N_x the KATRIN relevant measurands are calculated:

$$c_x = \frac{N_x}{\sum_j N_j} \quad \text{the concentration of a single constituent,}$$

$$\epsilon_T = \frac{N_{T_2} + \frac{1}{2}(N_{DT} + N_{HT})}{\sum_j N_j} \quad \text{the tritium purity and}$$

$$\kappa = \frac{N_{HT}}{N_{DT}} \quad \text{the HT-DT-ratio.}$$

The definition shown in Eq. 5.20 implies that, apart from the constant C , there are three independent input quantities for N_x , namely S_x , η_x and r_x . This implication is only valid for the theoretical intensity values r_x . They are calculated independent of any Raman measurement according to Eq. 3.26 for each constituent x . However, it is not possible to measure the Raman signal S_x without consideration of the system's spectral sensitivity $\eta(x)$. This can be explained by a closer examination of the LARAsoft analysis routine, which arises from the vertical sub-structure of the spectral sensitivity of the CCD.

In order to obtain N_x the raw 2D Raman signal is recorded on a CCD and processed using LARAsoft. An illustration of the analysis routine implemented in LARAsoft is depicted Fig. 5.9. LARAsoft, the processing steps and implemented algorithms are described in [Sch13a].

The first two processing steps allow to chose a region of interest (ROI) and remove dead pixels (DP) on the CCD and signals caused by cosmic rays (CR). This is necessary because signals from DP and CR would mimic Raman signal peaks. The next step is the correction of astigmatism effects. Afterwards, the background is subtracted using a Savitzky-Golay coupled advanced rolling circle filter (SCARF) algorithm [Sch13a, Jam13a]. Then, the spectral sensitivity correction is applied. In the binning step the 2D data is summed along the vertical axis and a 1D spectrum is created. Optional next steps are a second baseline subtraction using the SCARF algorithm and a median background subtraction.

Afterwards, the shape fit algorithm [Sch13a] is performed. The shape fit algorithm returns absolute scaling factors F_x for every peak at the wavelength x , which are proportional to $\frac{S_x}{\eta_x}$ from Eq. 5.20. At last these values F_x are corrected with the theoretical intensity values r_x . The results are proportional to $\frac{S_x}{\eta_x \cdot r_x}$ and therefore to N_x , but are calculated from two independent input quantities

$$\frac{F_x}{r_x} \propto N_x = \frac{S_x}{C \cdot \eta_x \cdot r_x}. \quad (5.21)$$

The other relevant measurands c_x , ϵ_T and κ are then calculated from the values N_x . The uncertainty of r_x is determined in [Sch13a]. Therefore, only the uncertainty of the shape fit factor F_x needs to be determined. However, there is no formula describing how F_x is calculated. The shape fit factor F_x is a result of successive processing of the raw CCD data. Therefore, a sensible way to determine the uncertainty $u_{F(x)}$ is to introduce the uncertainties at each processing step and investigate how $F(x)$ values change. For example using $\bar{\eta}(x) + u_{\eta, \text{comb}}(x)$ for the spectral calibration would result in a different shape fit factor F_x than using $\bar{\eta}(x)$ or $\bar{\eta}(x) - u_{\eta, \text{comb}}(x)$.

For these systematic investigations LARA cell #6, filled with $\epsilon_T > 95\%$ in 2012, was measured.

5.4.2 Uncertainty and correlations caused by spectral sensitivity correction

The spectral sensitivity $\eta(x) = \bar{\eta}(x) \pm u_{\eta, \text{comb}}(x)$ of the Raman system is determined by prior measurements of the SRM 2242 spectrum. The result of these measurements is given in section 5.3. During the main measurement every read out pixel value is multiplied with a correction value (Fig.5.9, Step 6).

Correlations

On all measurements of the KATRIN LARA system's spectral sensitivity it was observed that in the relevant range [610 nm:685 nm] the spectral sensitivity (Fig. ??) causes correlations. In order to describe the correlations the spectral sensitivity is approximated in first order by a straight line

$$f(x) = m(x - x_0) + y_0 \quad (5.22)$$

with $x_0 = 624$ nm and $y_0 = 1$ due to the normalization.

In Fig. 5.10 the measurements from chapter 4.5.1 are shown. Each spectral sensitivity curve has a function $f_j(x)$ fitted to it. It can be seen that the normalization point acts as a pivot point and the linear functions $f_j(x)$ for different $\eta_j(x)$ curves are tilted. This means that some pairs of $(\eta(x_j), \eta(x_k))$ are correlated and others anti-correlated, depending on their relative position to the normalization point. This is indicated by the arrows in Fig. 5.10 For example, if the value of $\eta(612$ nm) becomes larger, the value of $\eta(683$ nm) becomes smaller, although by a different amount. Therefore, it is not possible to simply use the $\bar{\eta}(x)$ and $\bar{\eta}(x) \pm u_{\eta, \text{comb}}(x)$ curves to determine the uncertainty.

Spectral sensitivity curves, which take the correlations into account need to be constructed from the data. These curves are shown in Fig. 5.11 and calculated according to

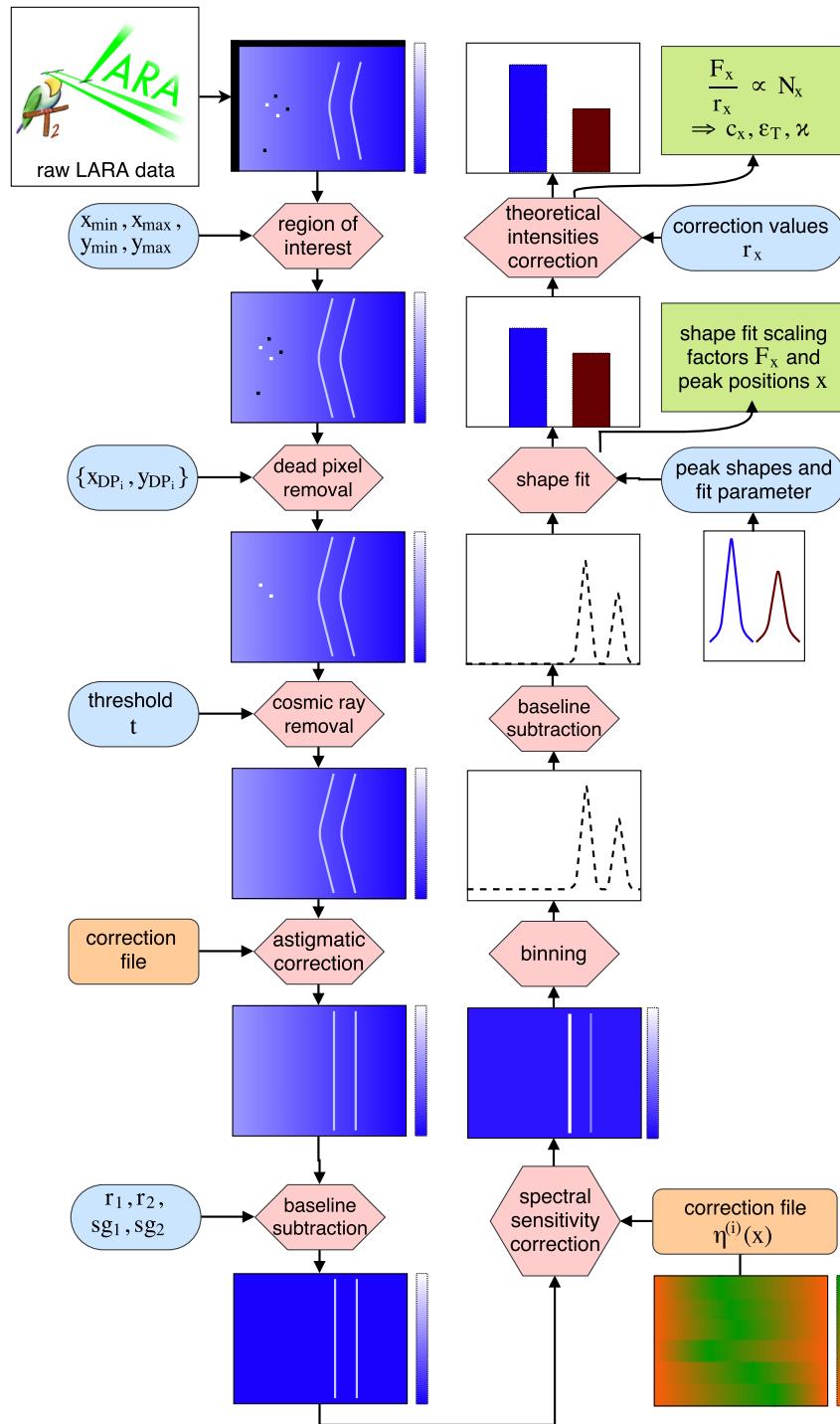


Figure 5.9: Illustration of the LARASoft analysis routine. The software version used is 1.1.1 – 150429. The raw data is processed in 10 steps in order to obtain the gas composition. The red hexagons visualize the processing steps. Blue ovals show input parameters that have to be determined by the operator at the start of the main measurement, while orange rounded squares are input parameters or files that have to be determined by prior measurements. Squares indicate output spectra, files or parameters from processing steps. A detailed explanation of each processing step can be found in the main text.

Table 5.2: Uncertainty caused by the spectral calibration. Measurements were performed on LARA cell #6.

Quantity	T ₂	DT	D ₂	HT	HD	H ₂
\bar{F}_x	5 960 612	330 884	104 074	2 029 101	58 005	99 213
$u_\eta(\bar{F}_x)$	59 199	1 157	724	42 872	1 847	5 013
$u_c(\bar{F}_x)/\bar{F}_x$ in %	0.99	0.35	0.70	2.11	3.18	5.05

$$\eta_1(x) = \begin{cases} \bar{\eta}(x) + u_{\eta,\text{comb}}(x) & \text{for } x \leq 624 \text{ nm,} \\ \bar{\eta}(x) - u_{\eta,\text{comb}}(x) & \text{for } x > 624 \text{ nm,} \end{cases} \quad (5.23)$$

and

$$\eta_2(x) = \begin{cases} \bar{\eta}(x) - u_{\eta,\text{comb}}(x) & \text{for } x \leq 624 \text{ nm,} \\ \bar{\eta}(x) + u_{\eta,\text{comb}}(x) & \text{for } x > 624 \text{ nm.} \end{cases} \quad (5.24)$$

These constructed curves take the observed correlations into account. The curves are used to create three different spectral calibration files: $\bar{\eta}(x)$ and $\eta_{1/2}(x)$. The files are used for the spectral calibration in LARASoft. In this way for every peak three different values are obtained. The standard uncertainties u_η for every fitted peak can then be calculated

$$u_\eta(F_x) = \frac{1}{2}(|F_x^{(\eta_1)} - F_x^{(\eta_2)}|). \quad (5.25)$$

The resulting standard uncertainties with LARA cell #6 are summarized in Tab. 5.2.

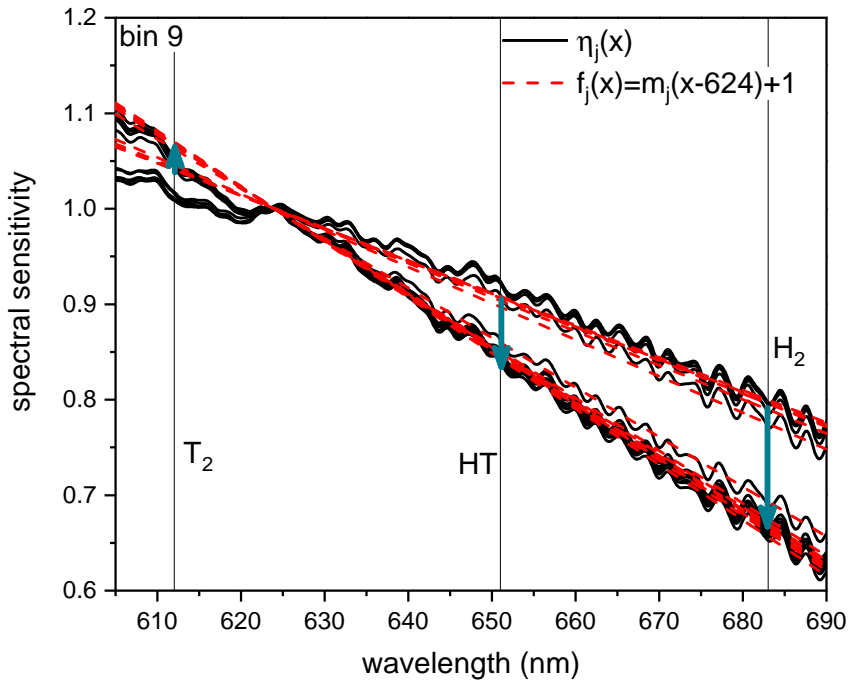


Figure 5.10: Multiple measurements of the spectral sensitivity $\eta_j(x)$ with fitted linear functions. The linear functions $f_j(x) = m_j(x - x_0) + y_0$ are fitted using $x_0 = 624$ nm and $y_0 = 1$ in the range [610 nm:685 nm]. The linear part tilts relative to the normalization point. The fit is performed with OriginLab.

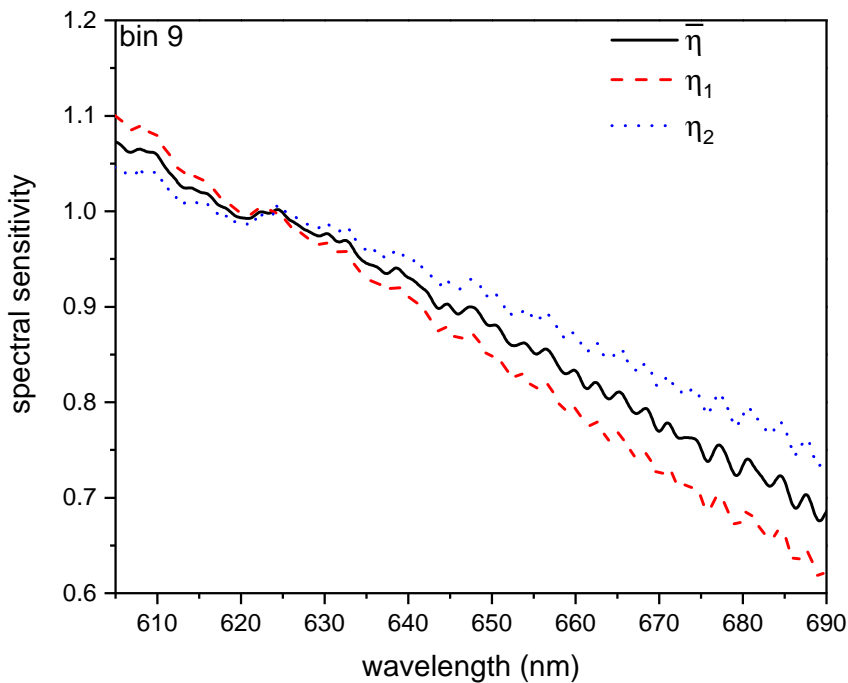


Figure 5.11: Averaged spectrum $\bar{\eta}(x)$ and two spectra $\eta_{1,2}(x)$, which take the observed correlations into account. Plot of the three η -files used for the measurement and the determination of the uncertainty $u(\bar{F}_x)$.

5.4.3 Determination of other uncertainty sources in laser Raman measurements

In principle each processing step shown in Fig. 5.9 can introduce uncertainties. Additionally, there are some other possible sources of uncertainties. All possible sources are discussed in the following.

Region of interest (ROI)

Regions of the CCD which are not properly illuminated or not of interest can be removed. Hence, reducing the raw readout to relevant data only. This does not introduce any uncertainty.

Dead pixel removal (DPR)

Every dead pixel on the CCD has to be flagged by the operator prior to the measurement. DP can be identified by inspection of an acquired test spectrum. The value of the DP is replaced by the average value of two neighbour pixels. There are two distinct possible cases: (i) *DP are missed*. These would appear as 'inverse peaks' and cause problems with the baseline subtraction algorithm. However, DP can be easily identified by the operator and therefore flagged. (ii) *DP are flagged and removed*. If the DP is not close to a peak in the spectrum, it can be assumed that the neighbouring pixels have an average with insignificant standard uncertainty and the uncertainty is negligible. By a slight modification of the optical setup it can always be achieved that there are no DP close to peaks. This is ensured for all Raman measurements.

Cosmic ray removal (CRR)

Measured CR are removed in LARASoft during the measurement by comparison of two consecutive spectra. If the difference d for a given pixel is larger than a set threshold t the pixel contains a CR. For this pixel the smaller of the 2 values is then taken as the pixel value. Else, if the difference is smaller than the threshold the pixel value is calculated as the average of the 2 values. This would introduce an uncertainty if CR are missed. A detailed discussion can be found in [Sch14a]. The uncertainty does depend on the threshold t . If t is chosen carefully the uncertainty is assumed to be negligible.

Astigmatic correction (AC)

By prior measurements of a broad spectrum with many lines (e.g. Neon) the astigmatism correction is determined [Jam12] and provided as an input file for the main measurement. To determine an estimation for the uncertainty $u_{AC}(\bar{F}_x)$ from different Ne-spectra 10 AC-files were created and used for the correction of the same raw data in order to quantify the impact on the signal (see Fig. 5.12). The result is summarized in Tab. 5.3. The full calculation can be found in Appendix B.1. The uncertainty $u_{AC}(\bar{F}_x)$ is smaller by an order of magnitude than $u_{\eta}(\bar{F}_x)$ and can therefore be neglected.

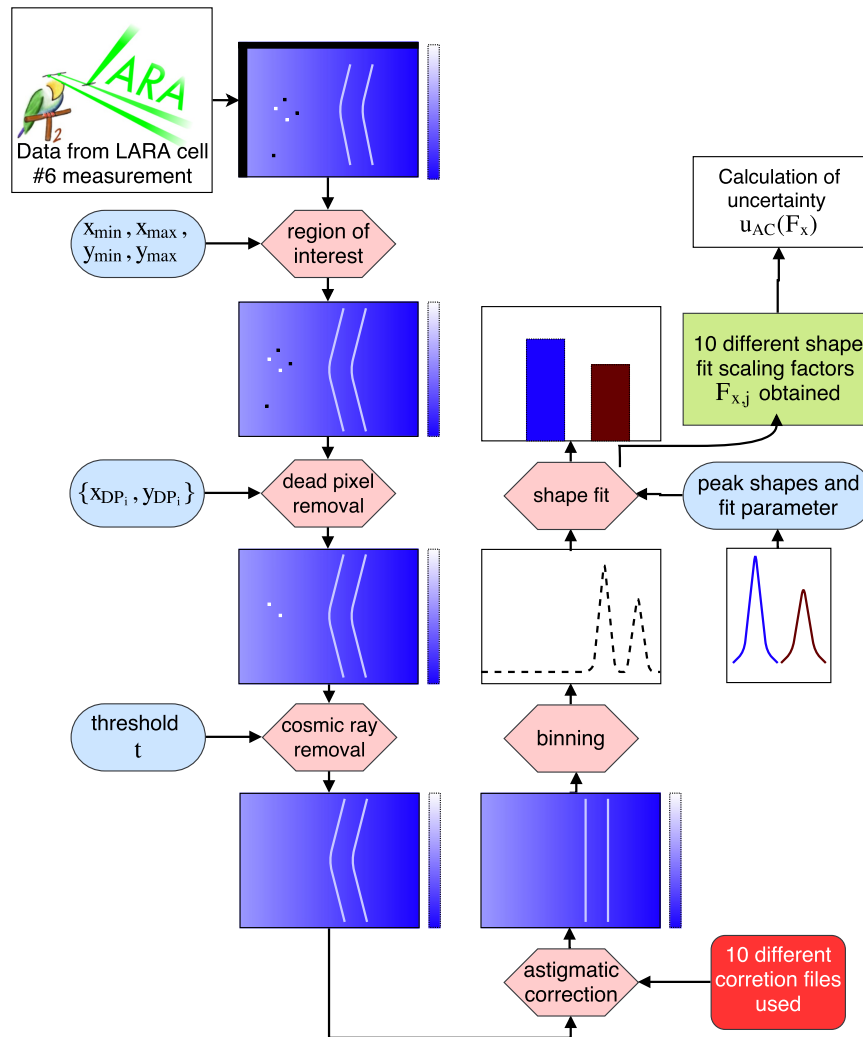


Figure 5.12: Illustration of the LARASoft workflow for the astigmatism correction uncertainty calculation. The red hexagons visualize the processing steps. Blue ovals show input parameters that have to be determined by the operator at the start of the main measurement, while orange rounded squares are input parameters or files that have to be determined by prior measurements. Squares indicate output spectra, files or parameters from processing steps. All steps and input parameters except the input astigmatic correction factor file (marked red) remained unchanged between runs. For every run the shape fit scaling factor is noted in order to calculate the uncertainty introduced by the astigmatic correction.

Table 5.3: Comparison of different uncertainty sources. The results for the uncertainties of the different hydrogen isotopologues in comparison. Measurements were performed on LARA cell #6. Clearly, the combined uncertainty $u_c(\bar{F}_x)$ is dominated by the uncertainty of the spectral sensitivity correction $u_\eta(\bar{F}_x)$.

Quantity	T ₂	DT	D ₂	HT	HD	H ₂
\bar{F}_x	5 960 612	330 884	104 074	2 029 101	58 005	99 213
$u_{AC}(\bar{F}_x)$	2 384	231	52	1 015	116	85
$u_{BS}(\bar{F}_x)$	40	18	212	16	19	17
$u_\eta(\bar{F}_x)$	59 199	1 157	724	42 872	1 847	5 013
$u_c(\bar{F}_x)$	59 247	1 180	726	42 884	1 851	5 013
$u_c(\bar{F}_x)/\bar{F}_x$ in %	0.99	0.36	0.70	2.11	3.19	5.05

Baseline subtraction

A Savitzky-Golay coupled advanced rolling circle filter (SCARF) algorithm [Sch13a, Jam13a] is used to determine and remove the baseline during live measurements. The algorithm depends on several input parameters (two rolling circle radii r_1, r_2 and two numbers of fit points sg_1, sg_2), which need to be optimized by the operator at the beginning of a measurement. However, there is a set of standard parameters that is suitable for most Raman measurements of hydrogen spectra. The selection of parameters does introduce an uncertainty u_{BS} , because there is a range of possible parameters which can be chosen and there is no set of ‘perfect’ parameters. To estimate the uncertainty different, plausible settings for the SCARF algorithm were used and the impact on the signal quantified (Fig. 5.13). The result is shown in Tab. 5.3, while the full calculation and range of parameters can be found in Appendix B.2. Compared to the other uncertainties, the uncertainty u_{BS} can be neglected if the chosen parameters

Binning

The vertical bins of the CCD are summed. This does not introduce any uncertainty, but can cause problems with uncertainty propagation, so caution is necessary. It should be avoided to propagate uncertainties through every step of LARASoft and rather evaluate the effect on the signal after fitting.

Shape fit

A fitting algorithm which uses peak shapes of the different peaks as an input. Does introduce shot noise σ_{shot} , background noise σ_{bkg} and read-out noise σ_{read} . In [Sch09, Sch13a] it was shown that the setup is capable of achieving a precision of better than 0.1 % for ϵ_T under consideration of the uncertainties by noise. These uncertainties are well understood and controlled. However, the calculation of the shape fit uncertainty is currently not implemented in LARASoft.

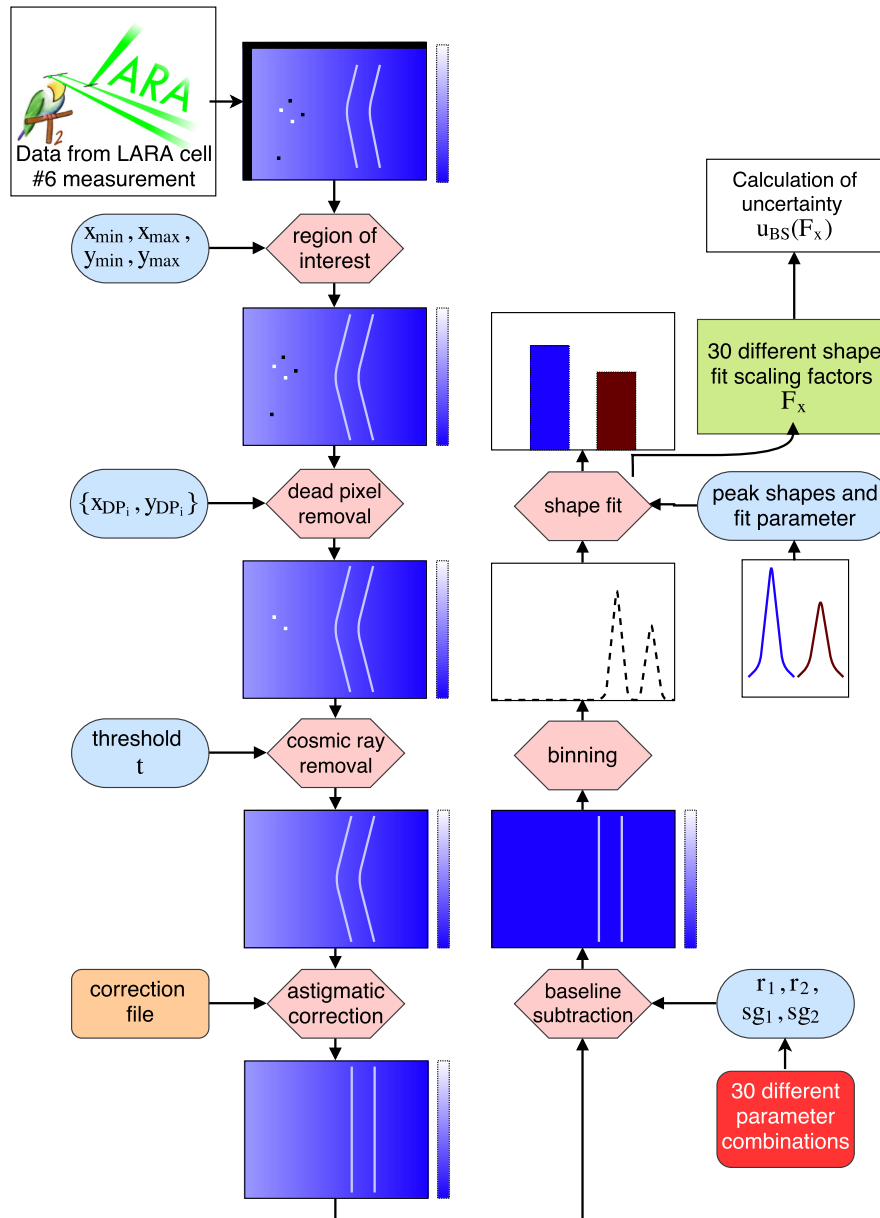


Figure 5.13: Illustration of the LARASoft workflow for the baseline subtraction uncertainty calculation. The red hexagons visualize the processing steps. Blue ovals show input parameters that have to be determined by the operator at the start of the main measurement, while orange rounded squares are input parameters or files that have to be determined by prior measurements. Squares indicate output spectra, files or parameters from processing steps. All steps and input parameters except the input parameters for the SCARF algorithm (marked red) remained unchanged between runs. For every run the shape fit scaling factor is noted in order to calculate the uncertainty introduced by the baseline subtraction.

Intensity correction by theoretical Raman transition matrix elements

The intensity results of the shape fit algorithm are multiplied with the respective correction value. This does introduce an uncertainty of about $u_{\text{theo}} \approx 3\%$. The uncertainty estimate originates from depolarization measurements [Sch13a, Sch13b], which were conducted to confirm the ab initio calculations from Schwartz and LeRoy [Sch87, LeR11], since the ab initio calculations contain no estimate of uncertainties.

In the last years, new calculations for transition matrix elements in optical spectroscopy have become available which feature theoretical uncertainties. Two of the leading groups in this field are those by K. Pachucki and J. Komasa (e.g. see [Cam12, Puc17, Pac15, Pac14]). For that reason, contact between K. Pachucki and the KATRIN-LARA group was established in order to obtain new calculations including a reliable uncertainty value. Currently, calculations are ongoing and it is assumed that an accuracy of about 0.1% is achievable for the Raman transition matrix elements.

The impact of the theoretical intensities uncertainties will be considered at the end of section 5.4.4.

Temperature

The NIST certificate for the SRM spectrum is only valid in a temperature range of [20 °C, 25 °C]. If the SRM spectrum is measured outside this range an additional shift needs to be applied to the certified SRM spectrum. The presented measurements were taken at a temperature of about 25 °C inside the glovebox. Therefore, a shift was not applied.

5.4.4 Results and discussion

In order to obtain an estimate of the uncertainties for the KATRIN operation, the measurements of the LARA cell # 6 were evaluated with the described methods. In Tab. 5.4 the results are summarized. For simplicity, the theoretical intensity values are set to $r_x = 1$. All results are calculated with a coverage factor $k = 1$, because the KATRIN requirements are also given with $k = 1$. The cell is filled with about 70 % T₂, 24 % D₂, 4 % DT and 1 % of the other isotopologues HT, HD and H₂ (Tab. 5.4). This results in a tritium purity of (only considering the uncertainty from the spectral sensitivity correction)

$$\epsilon_T = 0.832 \pm 0.002 \quad \text{with} \quad \frac{\Delta\epsilon_T}{\epsilon_T} = 0.24 \% \quad (5.26)$$

and a HT-DT-ratio

$$\kappa = 6.133 \pm 0.131 \quad \text{with} \quad \frac{\Delta\kappa}{\kappa} = 2.1 \% \quad (5.27)$$

These results are better than the KATRIN requirements by a factor of 5 for ϵ_T and κ .

However, the uncertainties depend on the source composition, since the sensitivity coefficients directly depend on the absolute values of N_x . In order to obtain the results for a KATRIN-like operation a source with $\epsilon_T > 0.95$ and $\kappa \approx 0.1$ needs to be measured and evaluated. Such a source is not available at the time of this thesis. Under the assumption that the uncertainties will stay in the same range for KATRIN operation this would result in (Tab. 5.4)

$$\epsilon_T = 0.9780 \pm 0.0002 \quad \text{with} \quad \frac{\Delta\epsilon_T}{\epsilon_T} = 0.02 \% \quad (5.28)$$

Table 5.4: Uncertainties of relevant measurands for the LARA cell#6 measurement results and for a KATRINlike measurement scenario. The dominant uncertainties u_η and u_{theo} propagated to the concentrations c_x , the tritium purity ϵ_T and the HT-DT-ratio κ . The possible future uncertainty $u_{\text{theo}}^{\text{future}}$ for the theoretical intensity uncertainty is shown in comparison to the current value. Currently the total uncertainty is dominated by the theoretical intensity uncertainty u_{theo} . It should be noted that the uncertainty of each quantity strongly depends on the measured gas composition.

Quantity	LARA cell #6				KATRIN-like scenario			
	value	$\pm u_\eta$	$\pm u_{\text{theo}}$	$\pm u_{\text{theo}}^{\text{future}}$	value	$\pm u_\eta$	$\pm u_{\text{theo}}$	$\pm u_{\text{theo}}^{\text{future}}$
c_{T_2}	0.695	0.003	0.008	0.0002	0.9561	0.0004	0.002	<0.0001
c_{DT}	0.012	0.005	0.019	0.0005	0.0400	0.009	0.036	0.0001
c_{D_2}	0.236	0.005	0.019	0.0005	0.0004	0.009	0.036	0.0001
c_{HT}	0.007	0.006	0.020	0.0005	0.0040	0.009	0.036	0.0001
c_{HD}	0.011	0.005	0.019	0.0005	0.0004	0.009	0.036	0.0001
c_{H_2}	0.832	0.005	0.019	0.0005	0.0004	0.009	0.036	0.0001
ϵ_T	0.832	0.002	0.005	0.0002	0.978	0.0002	0.001	<0.0001
κ	6.133	0.131	0.296	0.0014	0.1	0.002	0.005	0.0014

and

$$\kappa = 0.1 \pm 0.002 \quad \text{with} \quad \frac{\Delta\kappa}{\kappa} = 2.0\%. \quad (5.29)$$

In this case the relative tritium purity uncertainty would improve by an order of magnitude, while the relative HT-DT-ratio uncertainty would remain the almost unchanged. If additionally, the current uncertainties of about 3 % for the theoretical intensity correction are considered [Sch13d] the results change to

$$\epsilon_T = 0.832 \pm 0.006 \quad \text{with} \quad \frac{\Delta\epsilon_T}{\epsilon_T} = 0.72\% \quad (5.30)$$

and a HT-DT-ratio

$$\kappa = 6.133 \pm 0.324 \quad \text{with} \quad \frac{\Delta\kappa}{\kappa} = 5.3\% \quad (5.31)$$

for the measurement of LARA cell#6. For a KATRIN-like scenario the values are

$$\epsilon_T = 0.9780 \pm 0.001 \quad \text{with} \quad \frac{\Delta\epsilon_T}{\epsilon_T} = 0.1\% \quad (5.32)$$

and

$$\kappa = 0.1 \pm 0.005 \quad \text{with} \quad \frac{\Delta\kappa}{\kappa} = 5.0\%. \quad (5.33)$$

It becomes clear that the theoretical intensity uncertainty is the biggest contribution. However, in both scenarios the KATRIN requirements can be surpassed.

With the claimed achievable uncertainty for the theoretical intensities of about 0.1 % the result for a KATRIN operation would improve to

$$\epsilon_T = 0.9780 \pm 0.0002 \quad \text{with} \quad \frac{\Delta\epsilon_T}{\epsilon_T} = 0.02\% \quad (5.34)$$

and

$$\kappa = 0.1 \pm 0.002 \quad \text{with} \quad \frac{\Delta\kappa}{\kappa} = 2.1\%. \quad (5.35)$$

These results would be completely dominated by the uncertainty of the spectral sensitivity measurement and are nearly identical to the results without consideration of the theoretical intensity uncertainty in Eq. 5.28, Eq. 5.29.

Chapter 6

Conclusion and outlook

The KATRIN experiment aims to measure the electron antineutrino mass with a sensitivity of

$$m_{\bar{\nu}_e} = 0.2 \text{ eV}/c^2 \text{ (90 \% C.L.)}.$$

In order to reach this ambitious goal, systematic uncertainties have to be well understood and minimized in every part of the experiment. One of these systematic effects is the source composition in the WGTS. In the KATRIN experiment the source composition is measured and monitored in real-time using laser Raman spectroscopy. The main two measurands are the isotopic tritium purity ϵ_T and the HT-DT-ratio κ . The isotopic tritium purity ϵ_T needs to be measured with a trueness better than 3 % and a precision of 0.1 %, while for κ a trueness of 10 % has to be achieved. In order to achieve the trueness requirement the LARA system needs to be calibrated.

One possible method of calibration is to use theoretical intensities from ab initio calculations and combine them with the measured spectral sensitivity of the LARA system. The spectral sensitivity can be measured using a standard reference material (SRM) 2242 from NIST (see chapter 3.3.3, Fig. 3.9). However, the SRM 2242 is used in a configuration for which it was not designed and certified.

In order to use the SRM 2242 for the calibration of the KATRIN LARA system it must be positioned so that the laser beam hits it directly under the surface. For this purpose an alignment procedure is necessary. The main challenge arises from the fact that the SRM 2242 has to be positioned accurately on the 100 μm level in the glovebox environment of the KATRIN LARA system. Only if this problem can be solved, the LARA system can fulfil the KATRIN requirements. Such an alignment procedure was developed and tested within the scope of this work.

It was shown that by observing the shape of the laser dot passing through the SRM 2242 onto a screen, the SRM 2242 can be positioned accurately. Using this alignment procedure the SRM 2242 was measured at different vertical positions. Additionally, three different SRM plates with different usage histories and ages were compared. The measured spectral sensitivities showed agreement within a standard uncertainty of 3 %. Therefore, it can be assumed that the polishing of the lateral surfaces and the storage over years did not change the properties of the SRM 2242 standards. Despite the modifications the SRM 2242 standards can be used for the calibration. These measurements were performed with a

test system outside of the glovebox. With the test system a reproducibility of better than 5 % could be demonstrated.

Measurements with the KATRIN LARA system, when the alignment was performed within a glovebox, could confirm the good performance of the alignment procedure with a standard uncertainty well below 6 % in the relevant wavelength range across the whole CCD. Following the principles of the 'Guide to the Expression of Uncertainty in Measurement' (GUM), a method was established to calculate the standard uncertainty of the alignment procedure and the calibration method as a whole on the tritium purity ϵ_T , the HT-DT-ratio κ and the isotopologue concentrations c_x , while accounting for correlations caused by the spectral sensitivity correction.

For a KATRIN-like scenario with $\epsilon_T > 0.95$ and $\kappa \approx 0.1$ the alignment procedure causes uncertainties of

$$\frac{\Delta\epsilon_T}{\epsilon_T} = 0.02 \% \quad \text{and} \quad \frac{\Delta\kappa}{\kappa} = 2.0 \%$$

The calibration method as a whole results in uncertainties of

$$\frac{\Delta\epsilon_T}{\epsilon_T} = 0.1 \% \quad \text{and} \quad \frac{\Delta\kappa}{\kappa} = 5.0 \%$$

This shows not only the good accuracy of the alignment procedure, but also that the calibration method in total can easily fulfil the KATRIN requirements of $\frac{\Delta\epsilon_T}{\epsilon_T} \leq 3 \%$ and $\frac{\Delta\kappa}{\kappa} \leq 10 \%$. The biggest contribution to the uncertainty originates from the theoretical intensity uncertainties, which surpass the uncertainties from the spectral sensitivity by an order of magnitude. However, it should be noted that the uncertainties are this small because of the high isotopic tritium purity. For lower values of ϵ_T the uncertainties are higher.

With the newly developed alignment procedure the KATRIN LARA system can be calibrated successfully and surpass the KATRIN requirements.

Outlook A major unanswered question is the time-stability of the calibration. This can be investigated after the LARA stress test and before the KATRIN measurement start in June, 2018. As for now, the KATRIN LARA system should be calibrated once during every KATRIN maintenance phase. The calibration requires one day of measurements with the LARA system.

However, before the start of the KATRIN measurements the established calculation of the uncertainties has to be implemented in LARASoft, the used data acquisition and processing software.

Regarding further improvement of the calibration method, there are some points to consider:

- **The alignment procedure** could be optimised and automated. It would be possible to record the image of the laser dot with a camera and evaluate the shape using a dedicated software. This would most certainly further improve and facilitate the alignment procedure. However, this is not a priority, because the uncertainty of the calibration method is dominated by the theoretical intensities.

- **The theoretical intensities** will maybe be recalculated by groups of K. Pachucki and J. Komasa, which will possibly improve the uncertainties to about 0.1 %. Contact between K. Pachucki and the KATRIN-LARA group was already established.
- **TriHYDE**, the gas-mixing facility for T₂-D₂-H₂ will be available in 2018. This will enable cross-checking of the calibration with accurate gas samples. This could further confirm the calibration and alignment procedure.

With these developments the current accuracy of the KATRIN LARA system could be improved, thus further reducing the uncertainties impacting the KATRIN neutrino measurement.

Appendix A

Spectral sensitivity measurements in every CCD bin

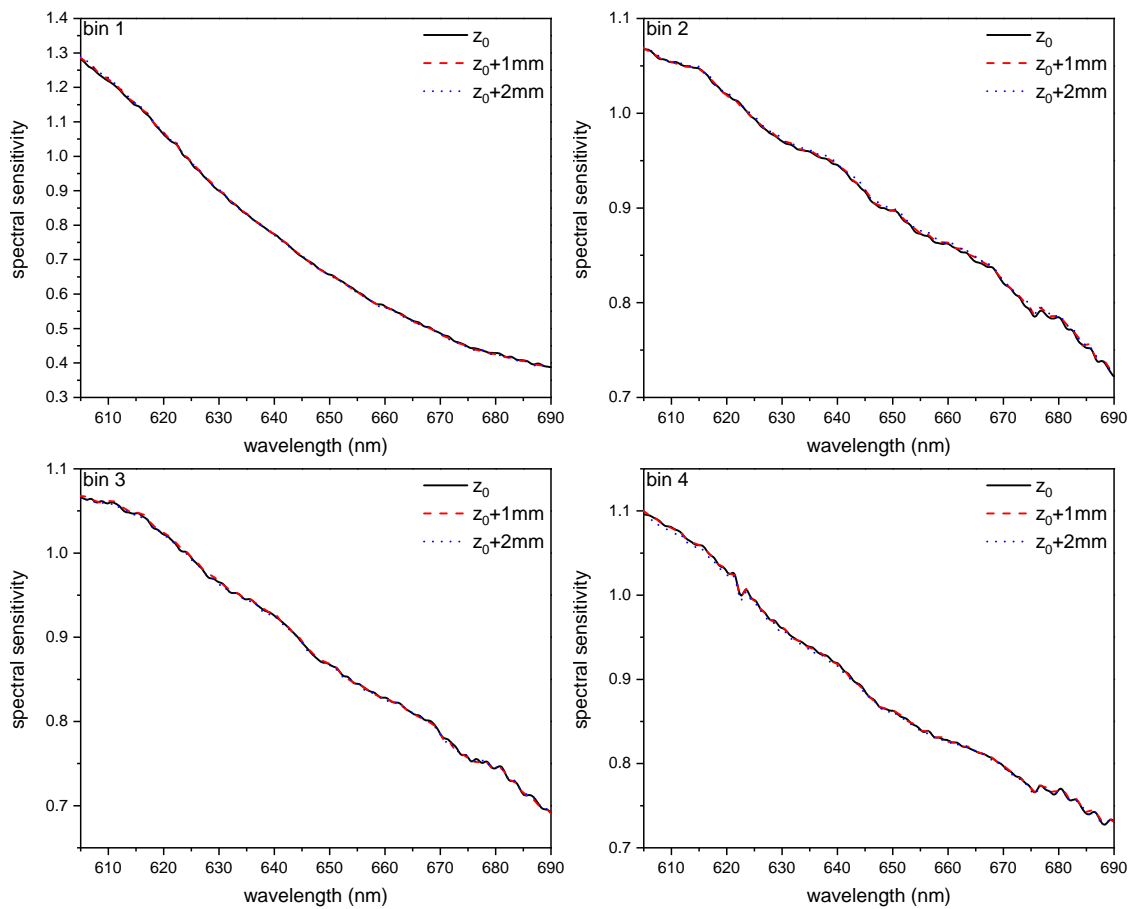
The investigations published in [Sch15a] and summarized in section 3.3.3 have shown that the spectral sensitivity of the CCDs has a 2D structure. Therefore, it is necessary to determine and apply the spectral sensitivity correction before the summation of vertical pixels/bins. For typical LARA measurements the vertical pixel of the CCD are summarized in 20 vertical bins.

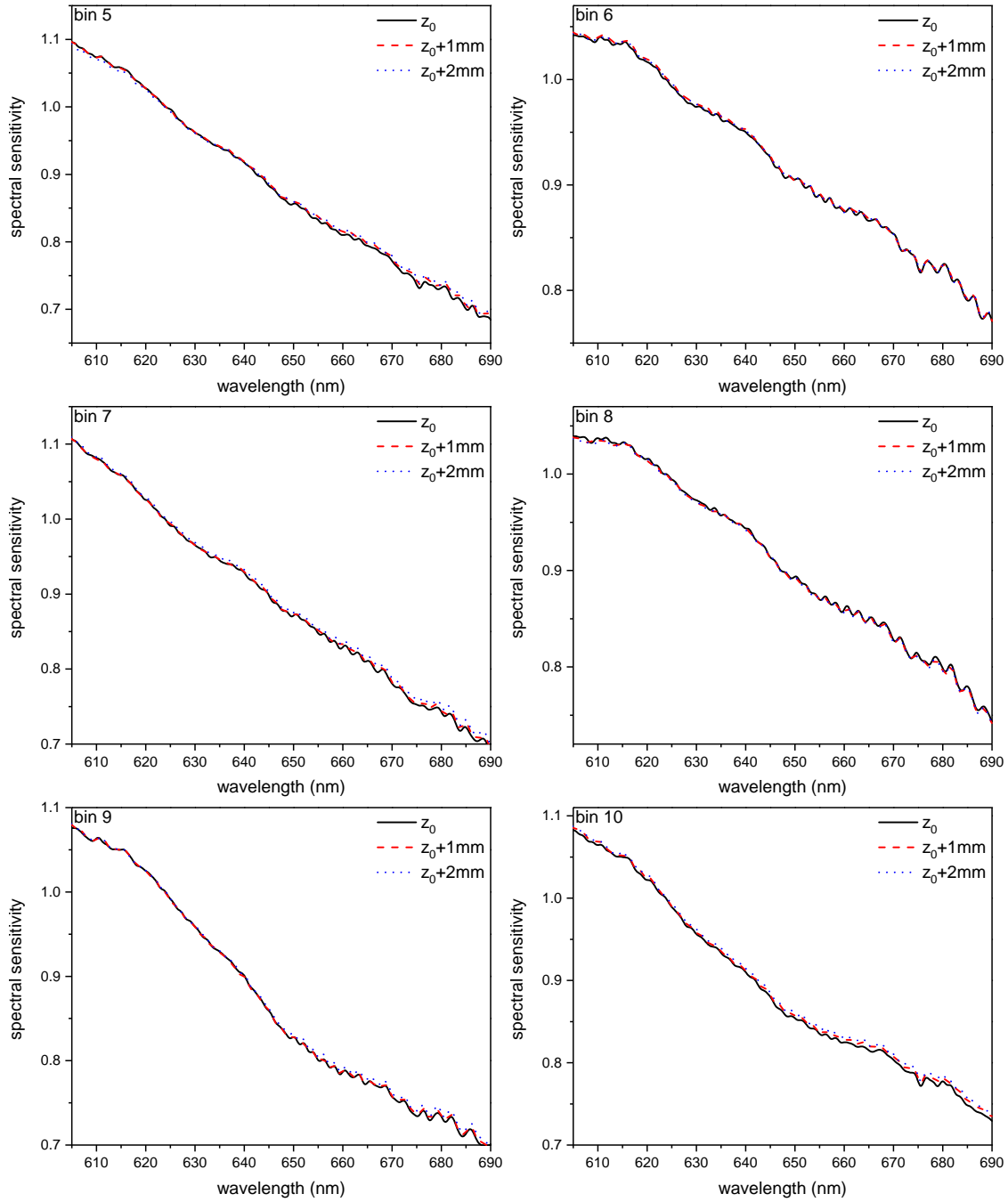
In the main section of this work for the different measurements of the spectral sensitivity one or two bins are shown for illustration. Often, most bins show similar behaviour and discussing one bin is sufficient. Here, the following results for all 20 bins are shown.

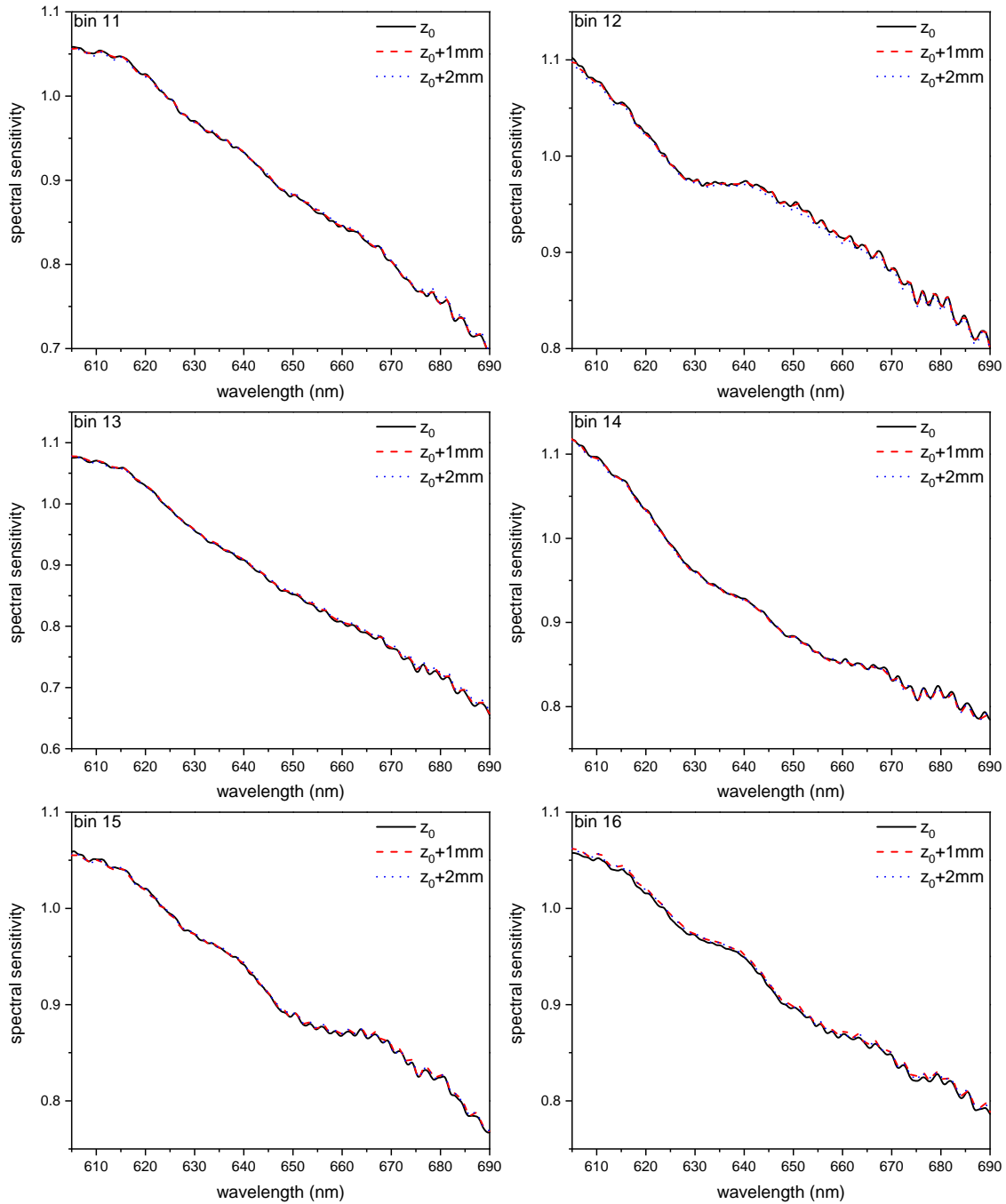
- **Section A.1:** The SRM 2242 is measured in the test setup at different vertical positions without changing the lateral position, which is determined with the developed alignment procedure. A complete description of the measurements and the discussion of the result is shown in section 4.4.1 of the main text.
- **Section A.2:** Using the alignment procedure the three different available SRM 2242 positioned with the laser beam hitting directly under the surface. Multiple measurement with every standard where conducted and compared. These measurements were performed using the test system. Section 4.4.2 contains the discussion of the results.
- **Section A.3:** One SRM 2242 was positioned 27 times in the test system using the alignment procedure and the spectral sensitivity calculated. The results can be found in section 4.4.3.
- **Section A.4:** The SRM 2242 was positioned multiple times using the alignment procedure in the glovebox environment of the KATRIN LARA system. An in-depth description and discussion is contained in section 4.5.
- **Section A.5:** The measured and normalized intensity curves, which are used for the spectral sensitivity calculation shown in section A.4 displayed. The data is used in section 5.3 for the calculation of the spectral sensitivity standard uncertainty.

- **Section A.6:** The intensity values of the data in section A.5 at 660 nm. Also, discussed section 5.3.
- **Section A.7:** The spectral sensitivity curves with the calculated standard uncertainty from section 5.3.

A.1 Spectral sensitivity as a function of the vertical position of the SRM 2242







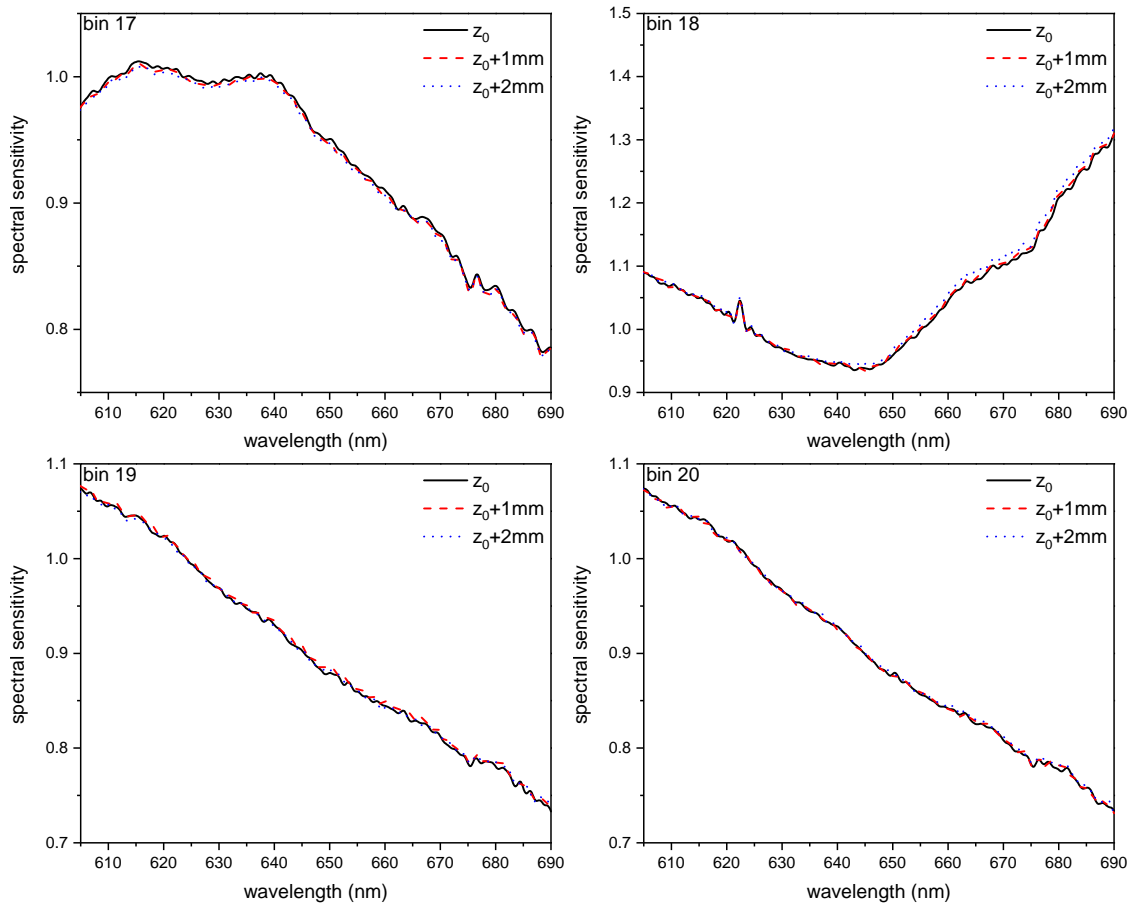
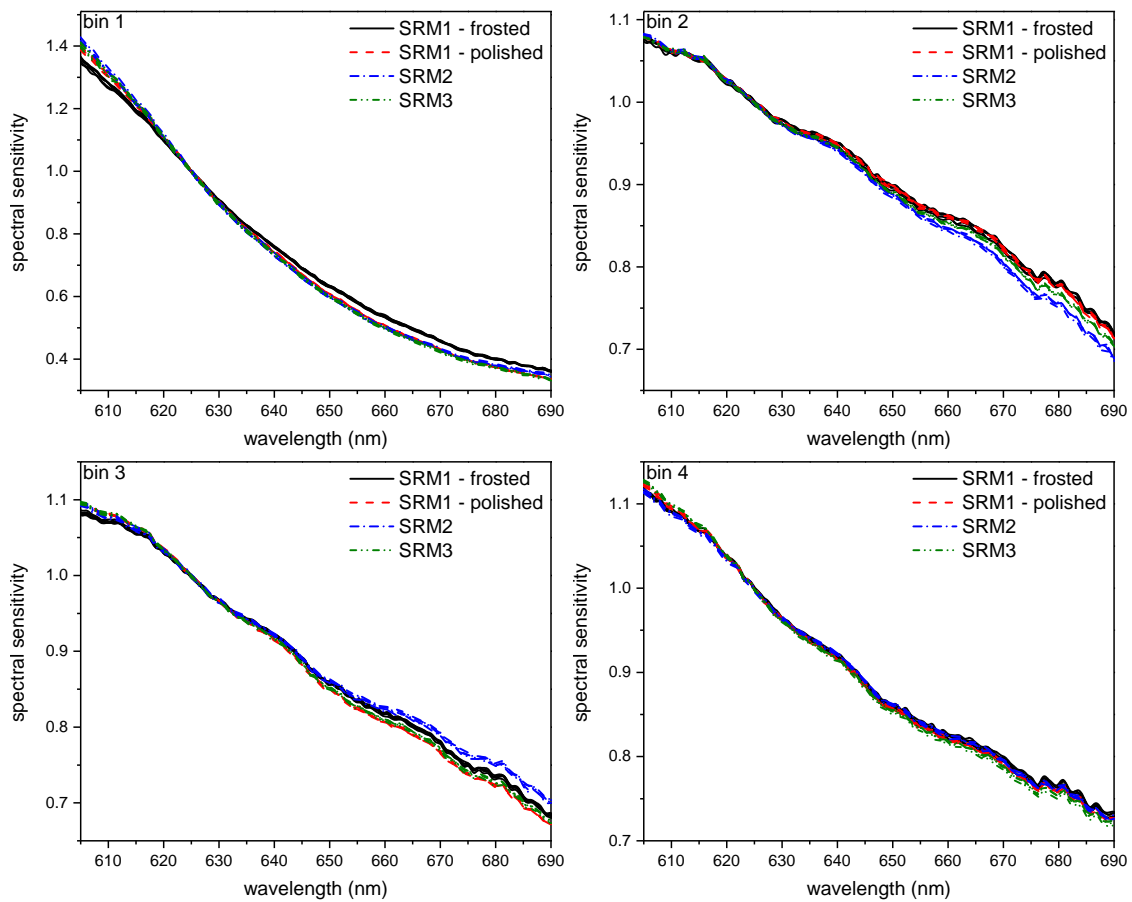
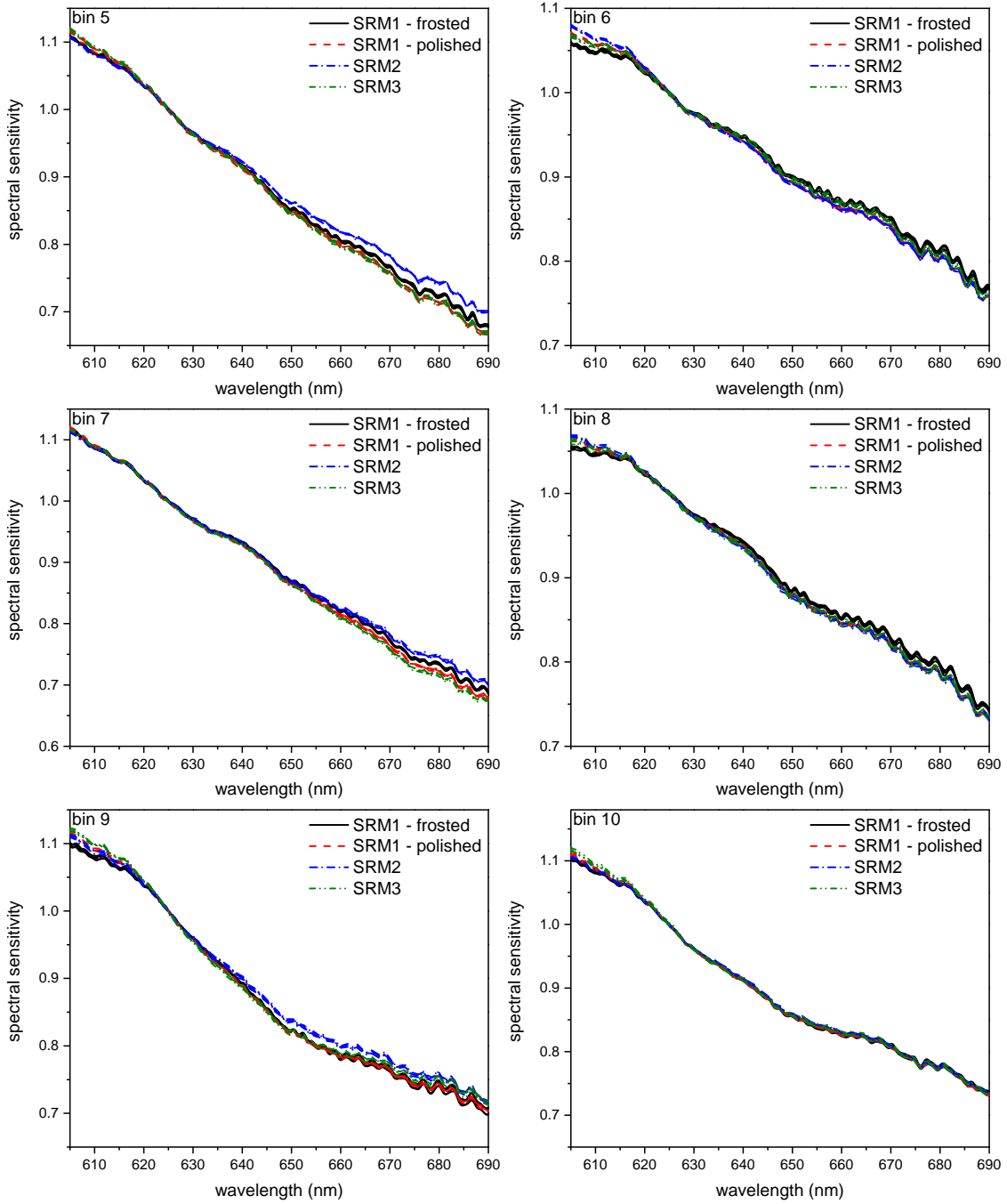
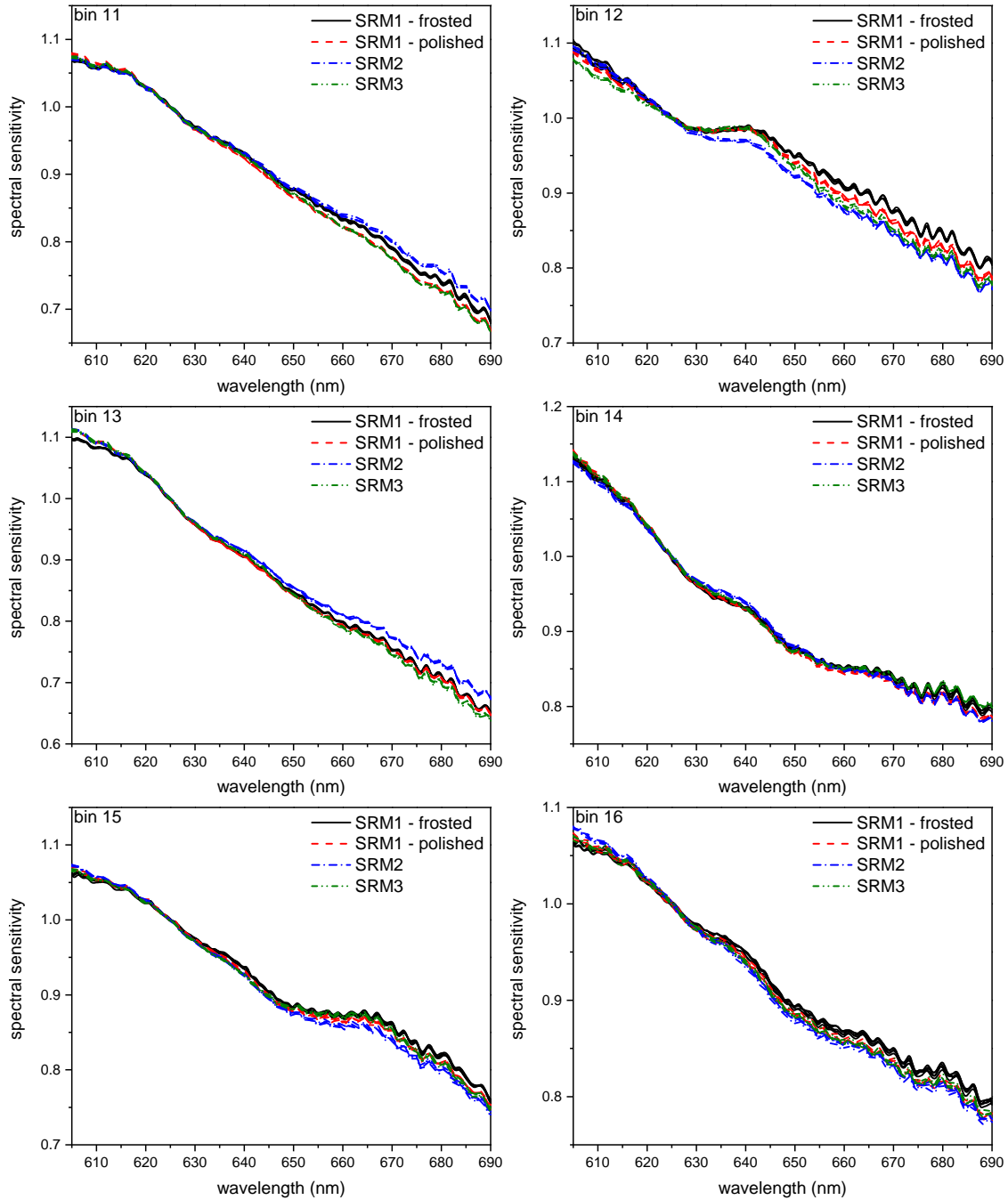


Figure A.1: Spectral sensitivity in every CCD bin as a function of the vertical position of the SRM 2242. Using the alignment procedure the standard was positioned with the laser beam hitting directly under the surface. Without changing the lateral position, the vertical position of the SRM 2242 was changed twice by about 1 mm. The three resulting spectral sensitivity curves show good agreement in every bin of the CCD.

A.2 Spectral sensitivity determined with three different SRM 2242







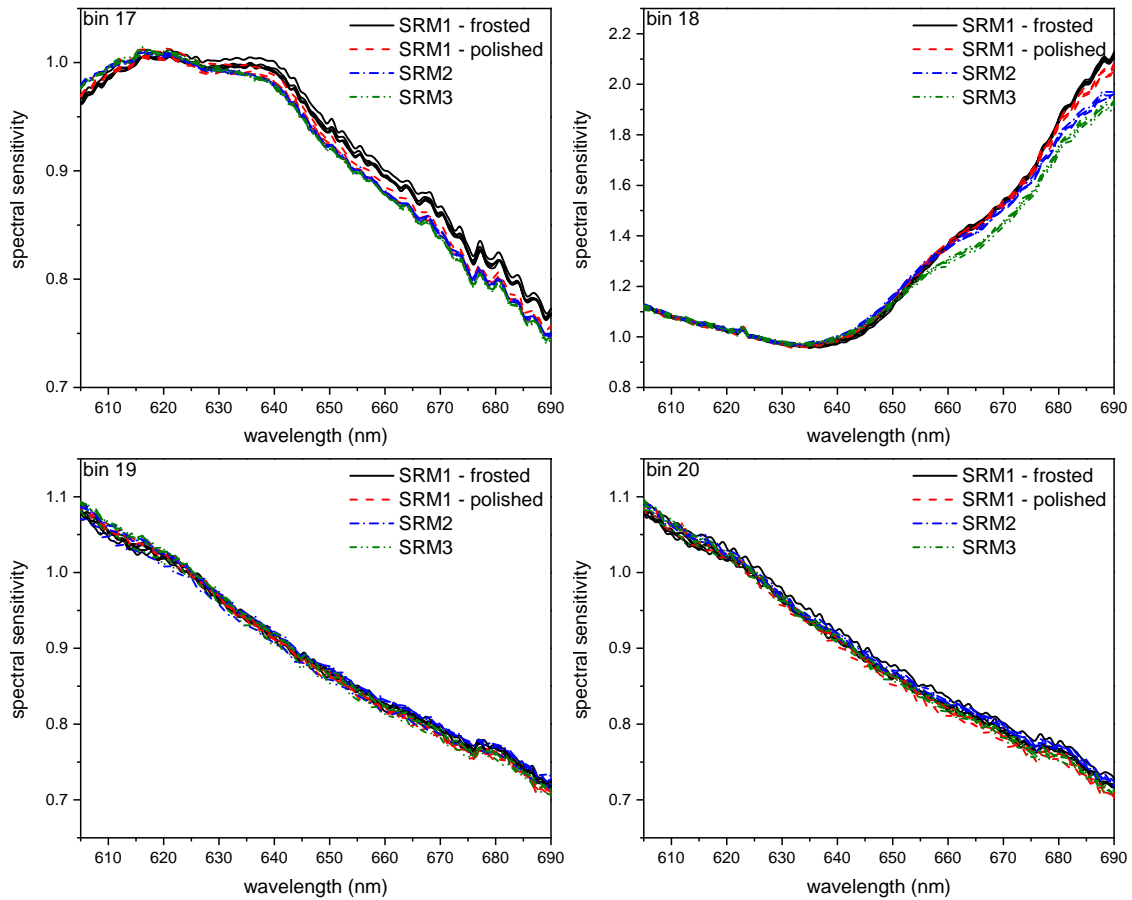
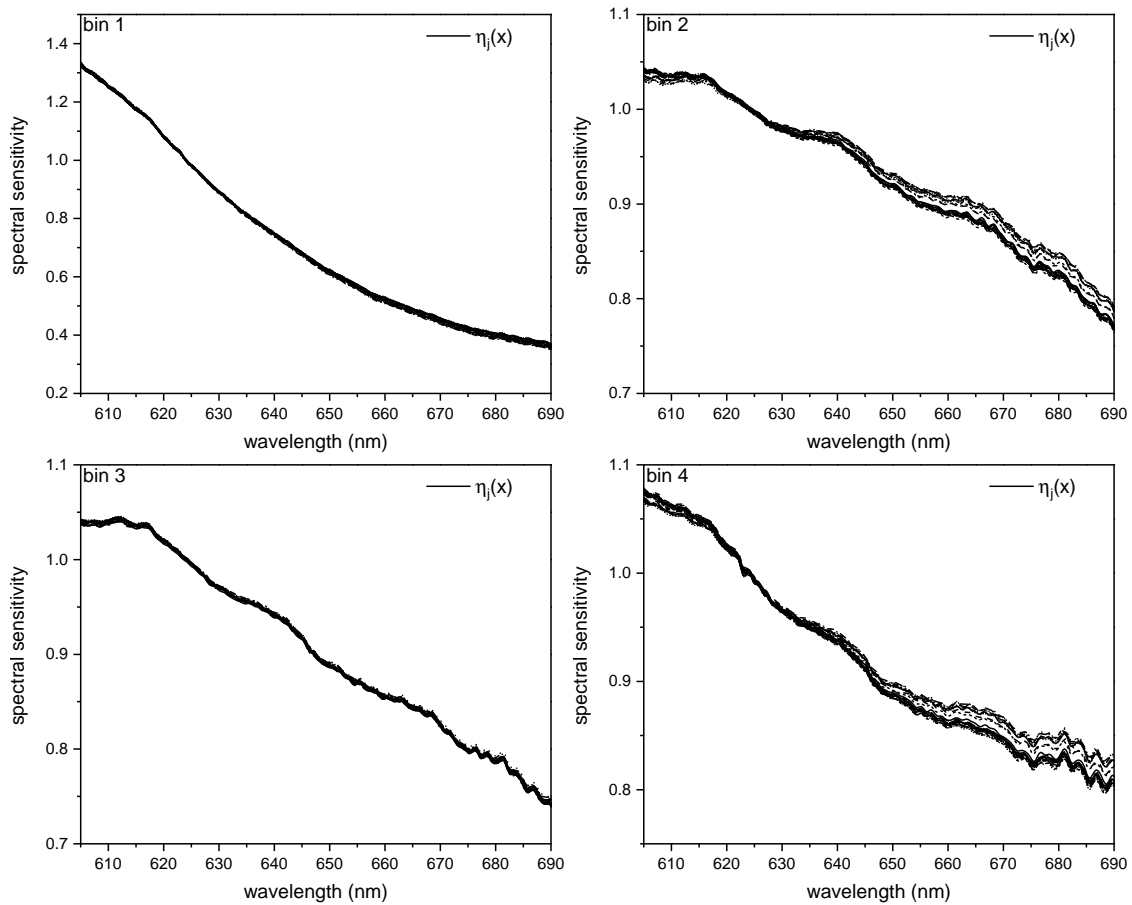
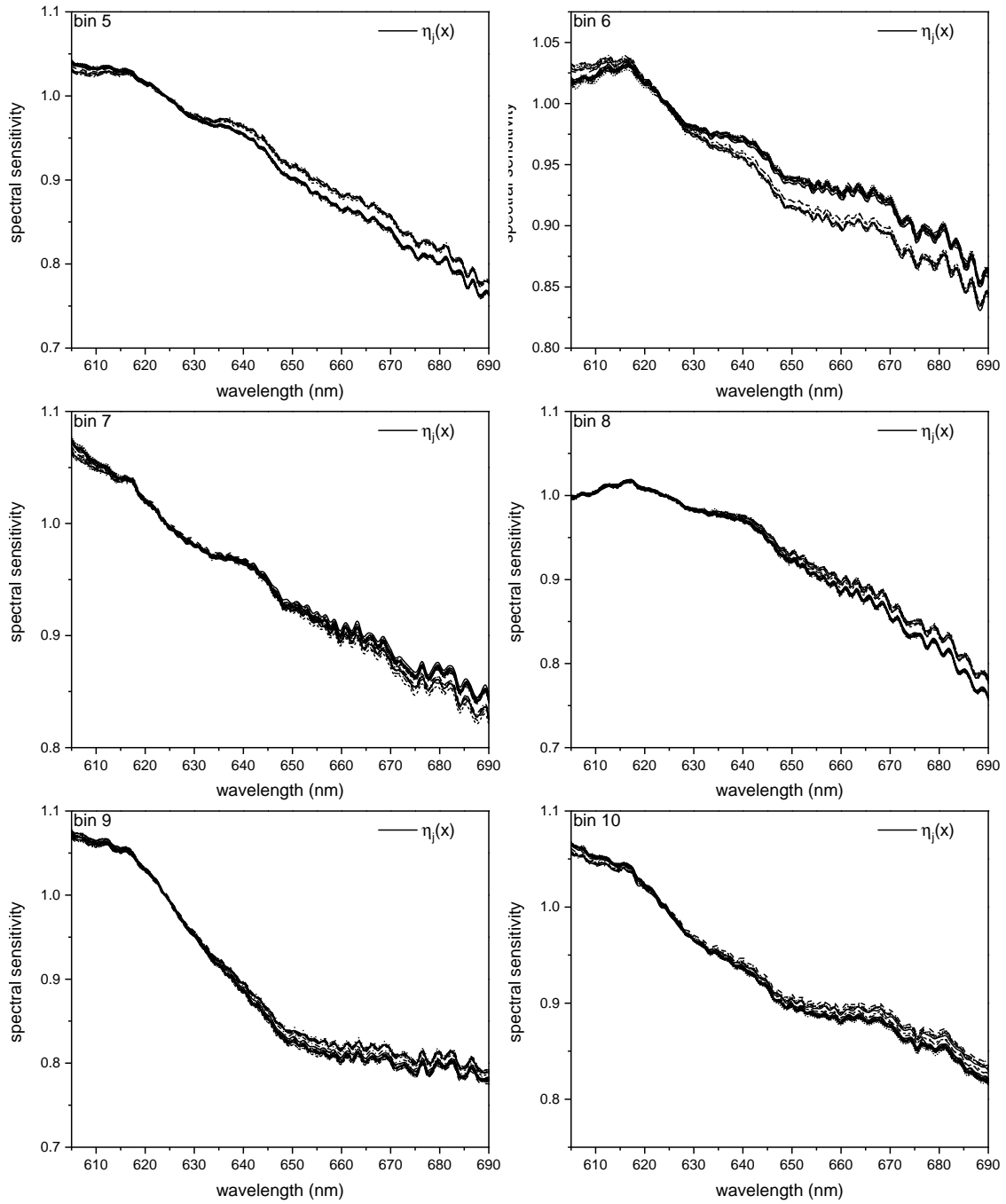
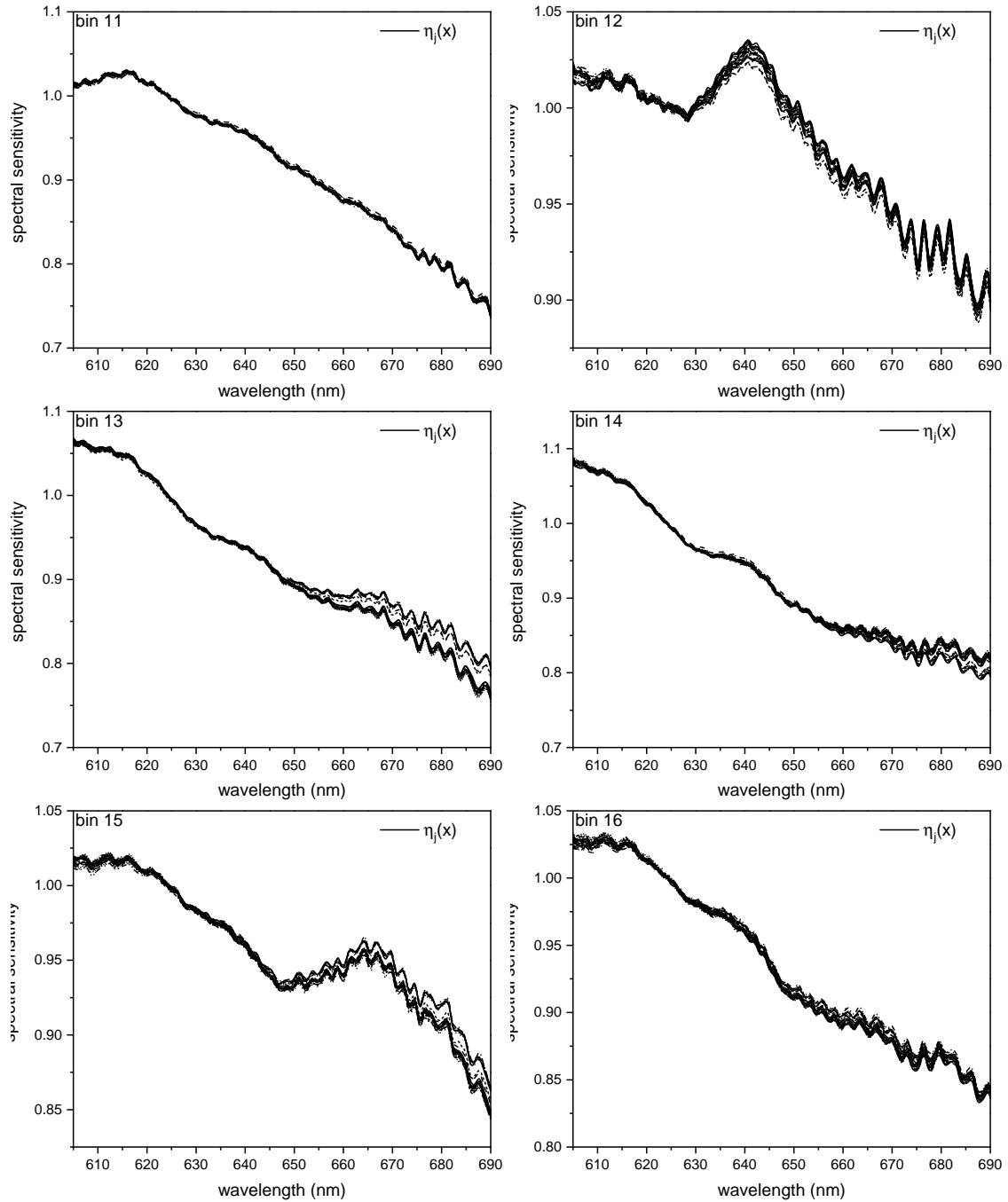


Figure A.2: Spectral sensitivity in every CCD bin determined with three different SRM 2242. Using the developed alignment procedure the SRM 2242 standards were positioned with the laser beam hitting directly under the surface. The resulting spectral sensitivity curves show overall good agreement, although in some bins a shift in the region above 650 nm is visible.

A.3 Spectral sensitivity determined with multiple repositionings of the SRM 2242







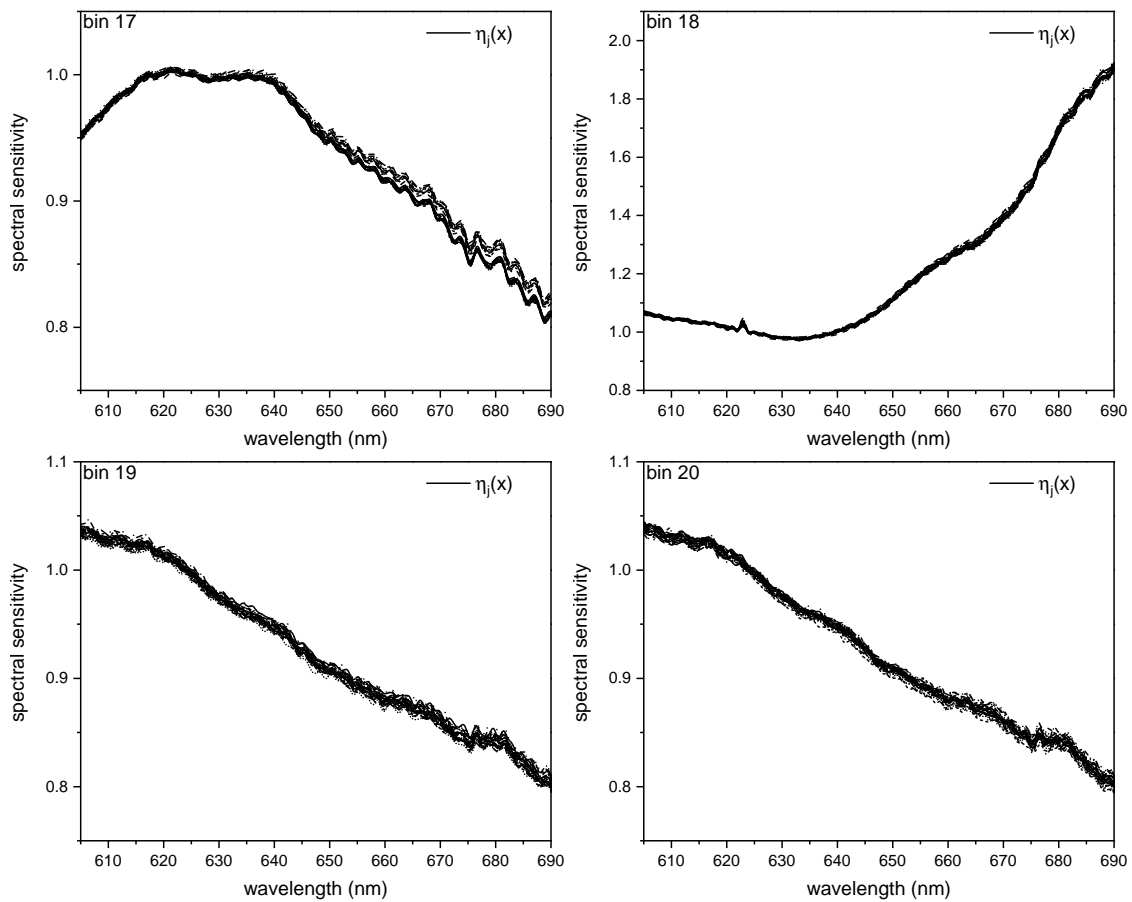
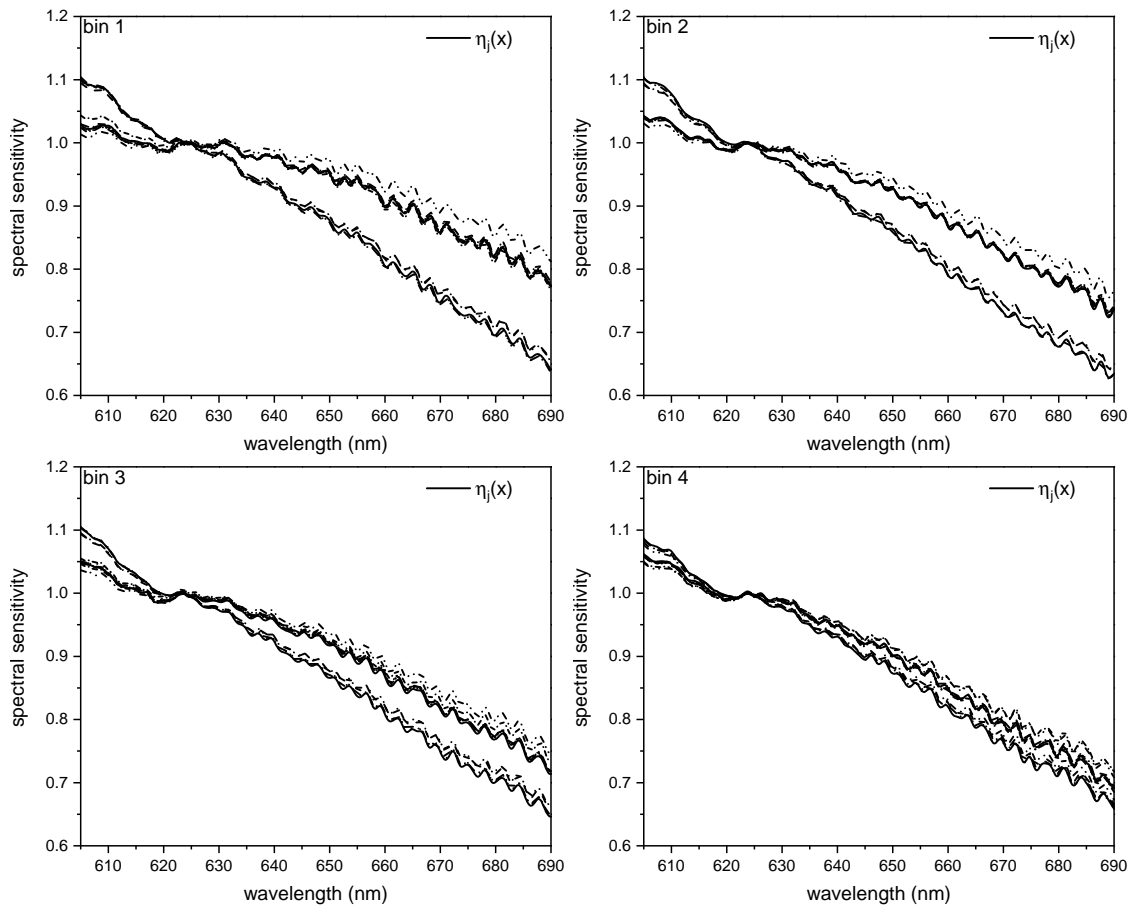
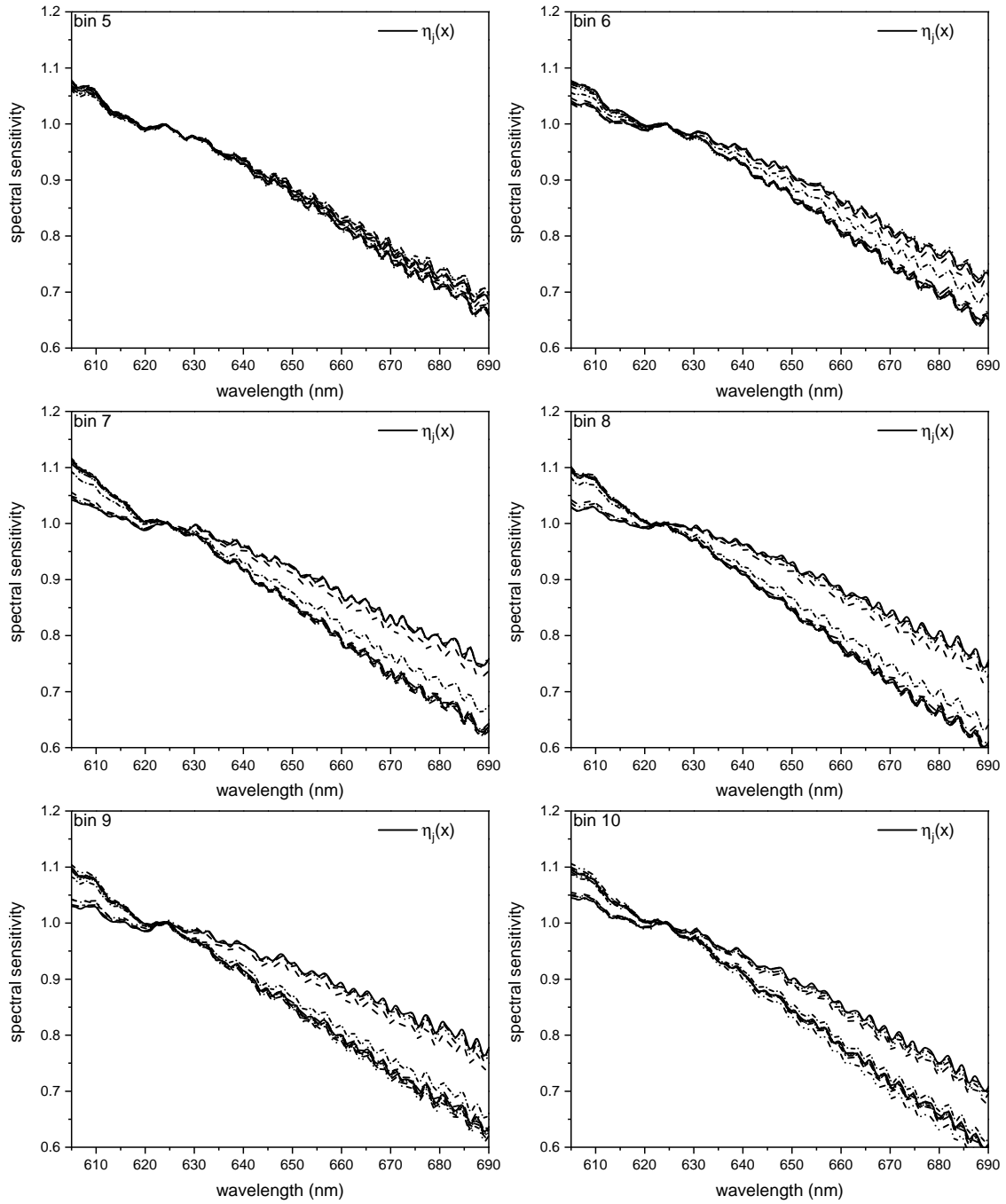
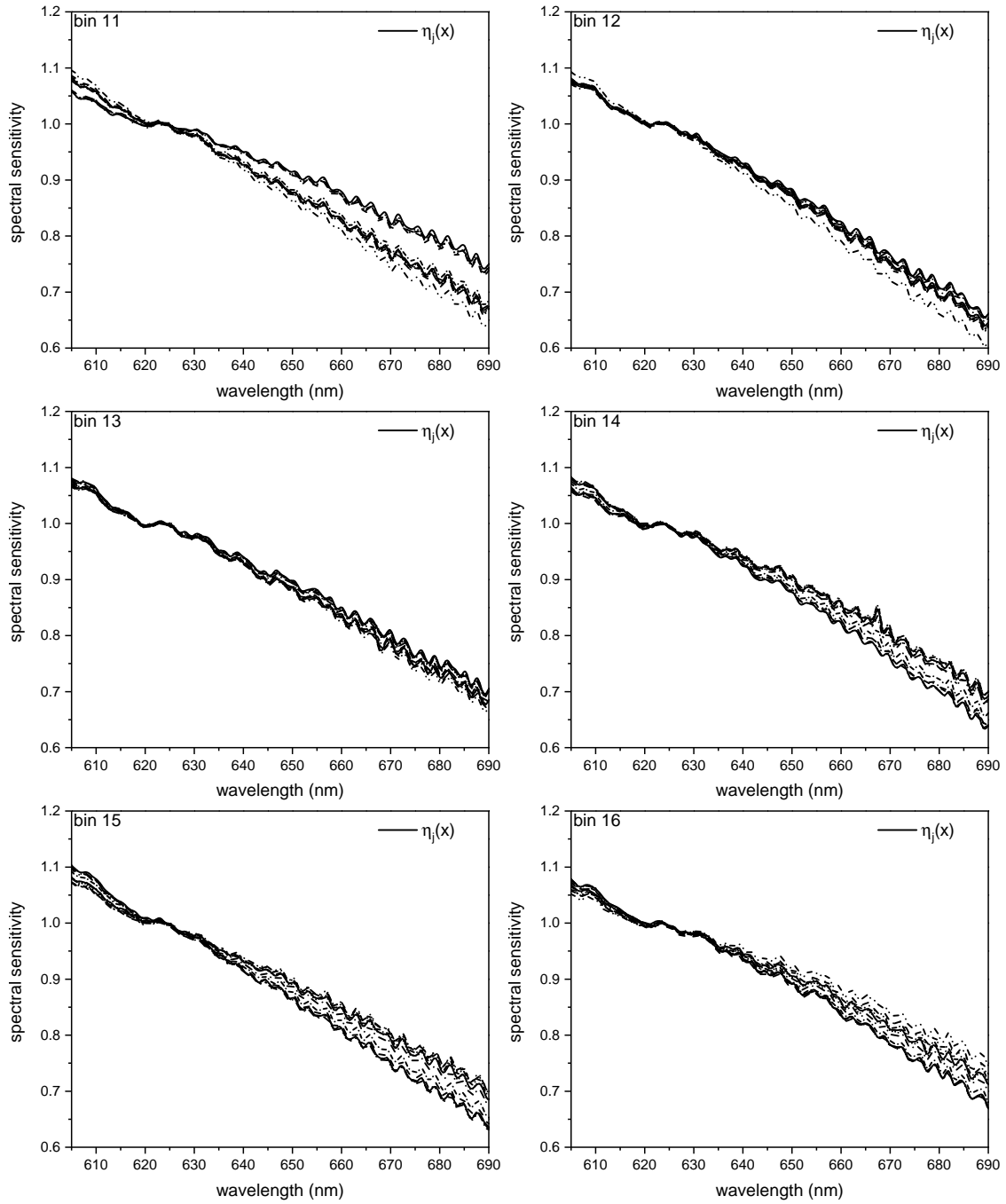


Figure A.3: Spectral sensitivity in every CCD bin determined with multiple repositionings of the SRM 2242. Using the alignment procedure the SRM 2242 standard was positioned 27 times with the laser beam hitting directly under the surface. In some bins the measurement curves split into two groups, while other bins show a good agreement.

A.4 Spectral sensitivity of the KATRIN LARA system determined with multiple repositionings of the SRM 2242 inside the glovebox







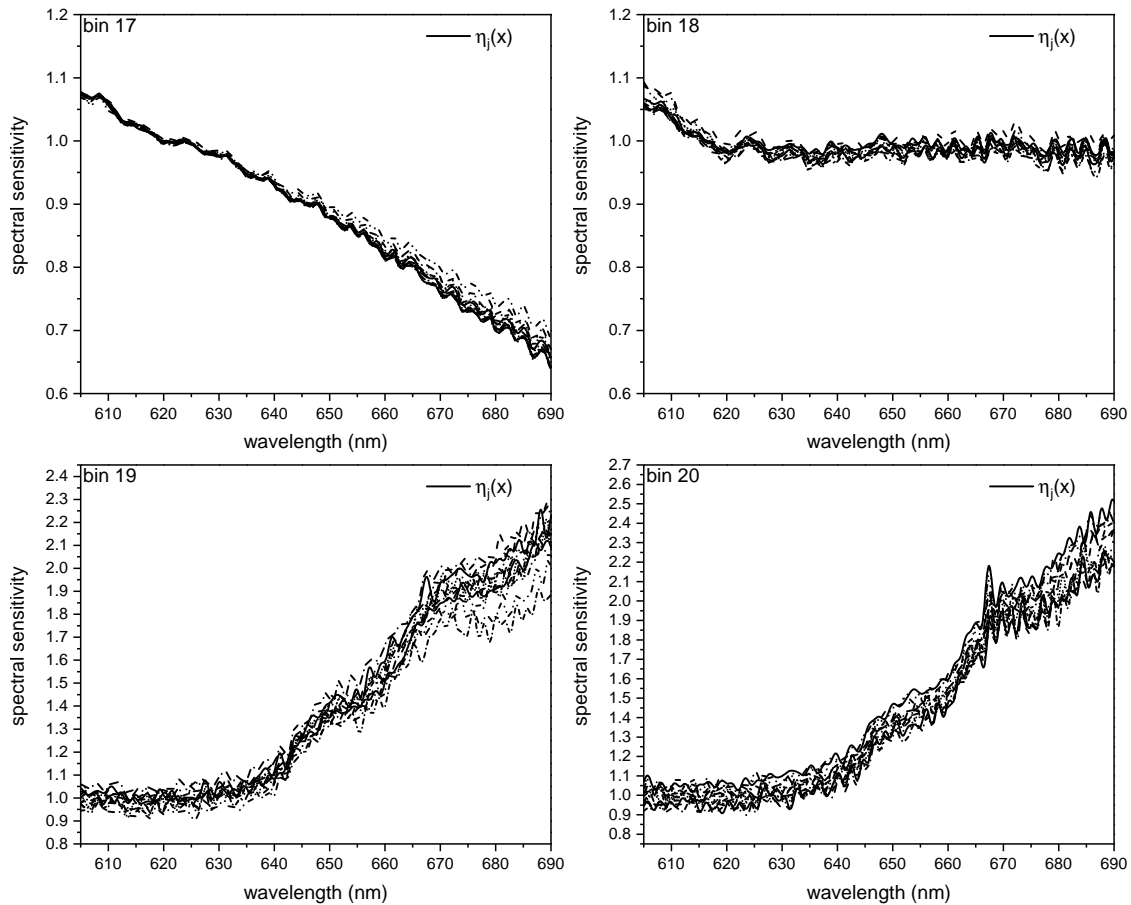
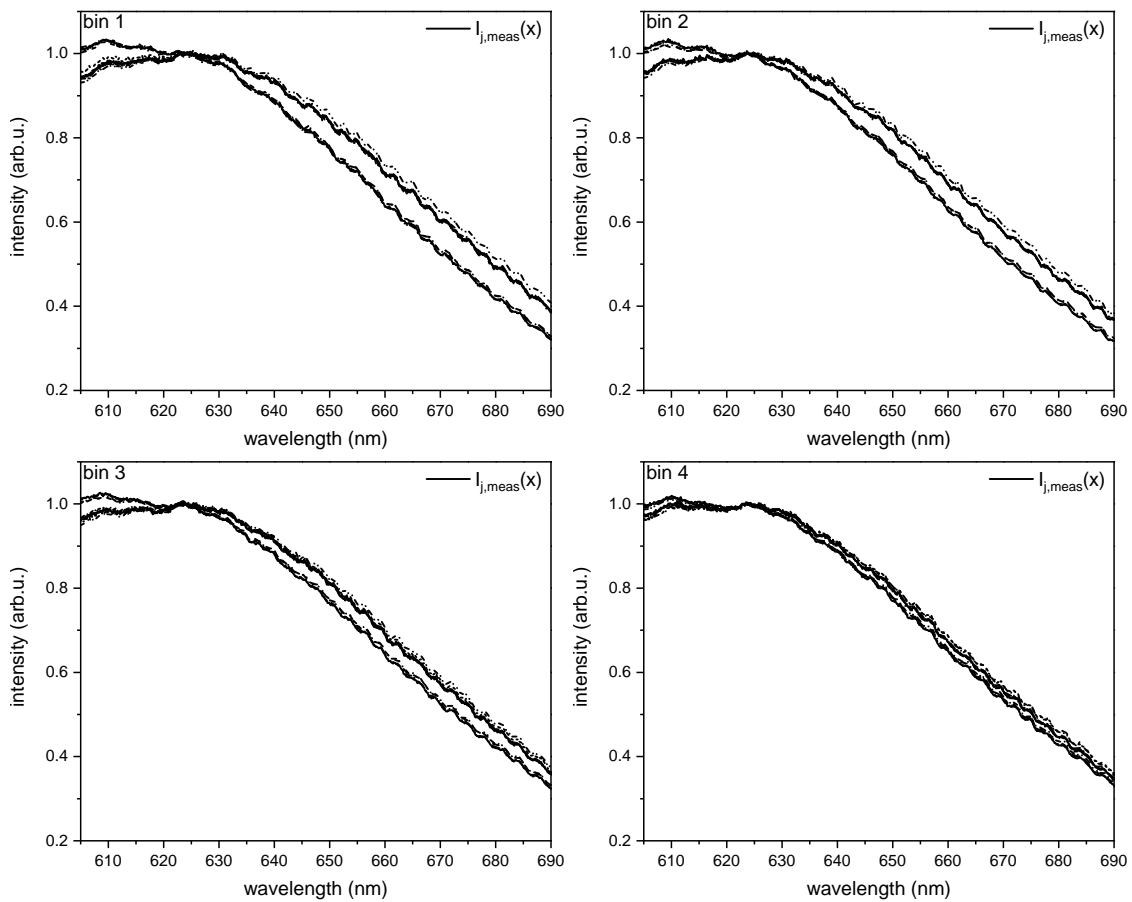
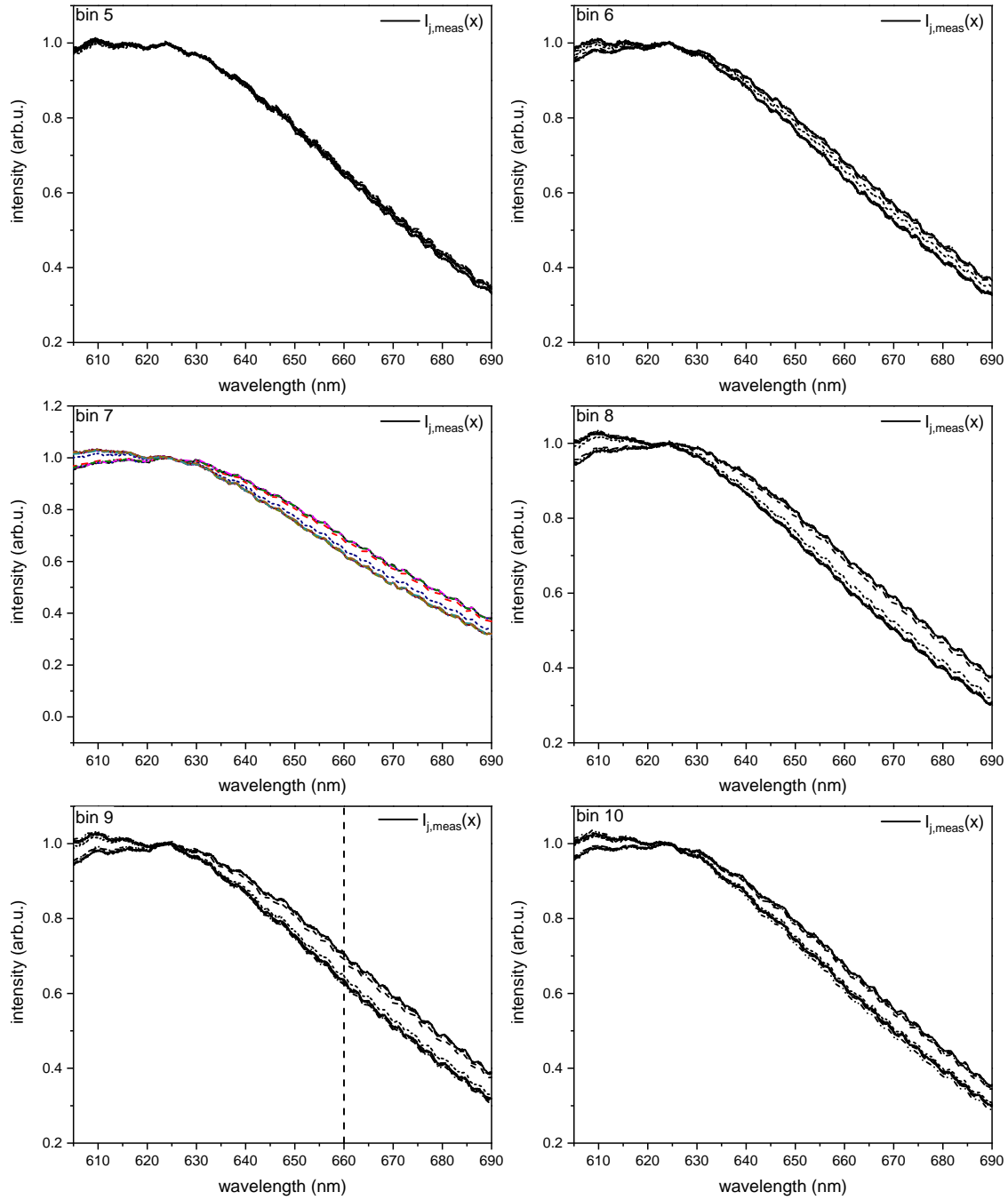
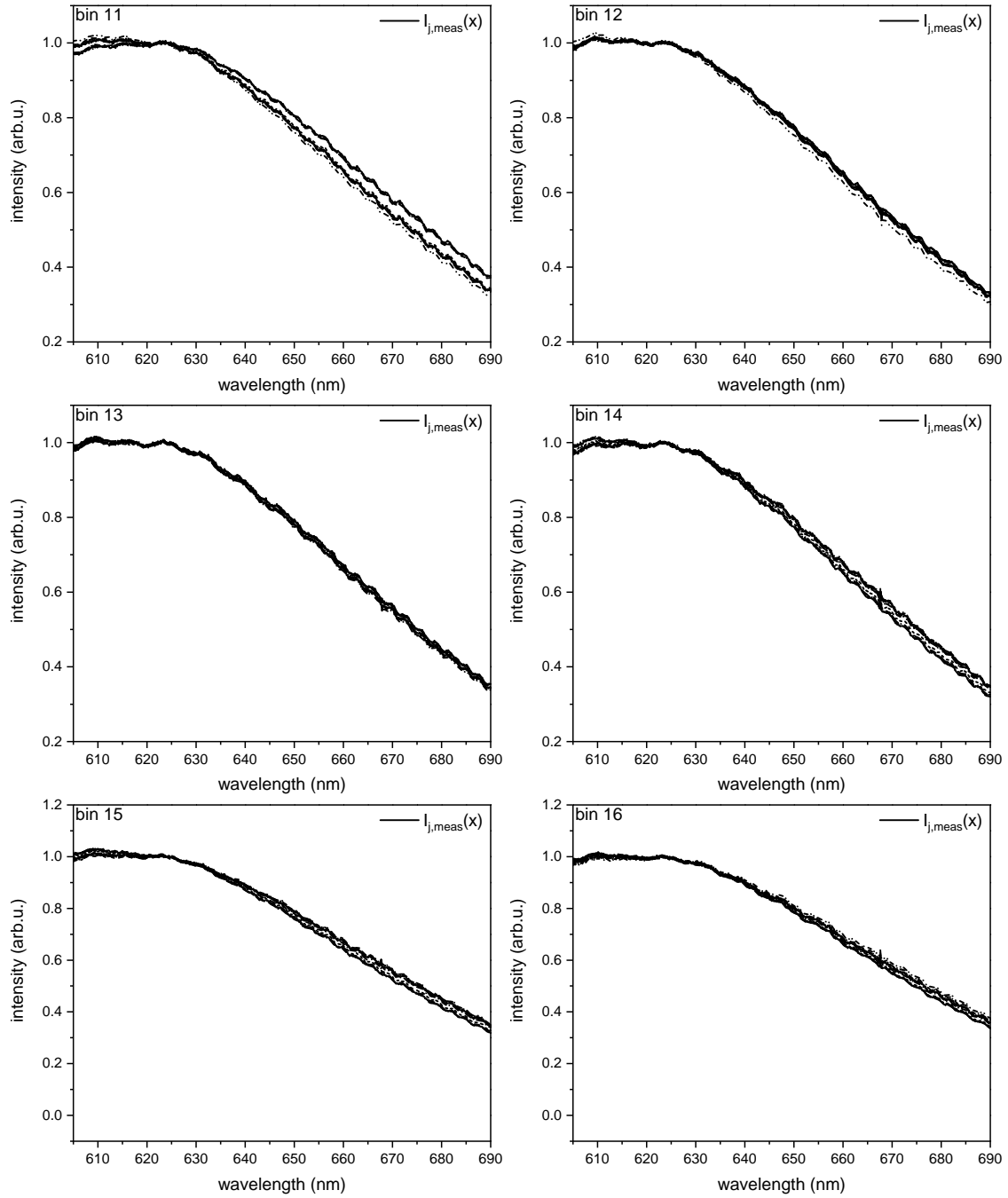


Figure A.4: Spectral sensitivity in every CCD bin of the KATRIN LARA system determined with multiple repositionings of the SRM 2242 inside the glovebox. Using the developed alignment procedure the SRM 2242 was positioned with the laser beam hitting directly under the surface. The resulting spectral sensitivity curves split up into 2 groups. In some bins the difference between the groups is up to 0.1, which is about 10 % difference. In bins the maximum difference is smaller than 0.01. The origin of the difference between bins is not completely clear.

A.5 Measured and normalized intensity curves of the SRM 2242 in every bin







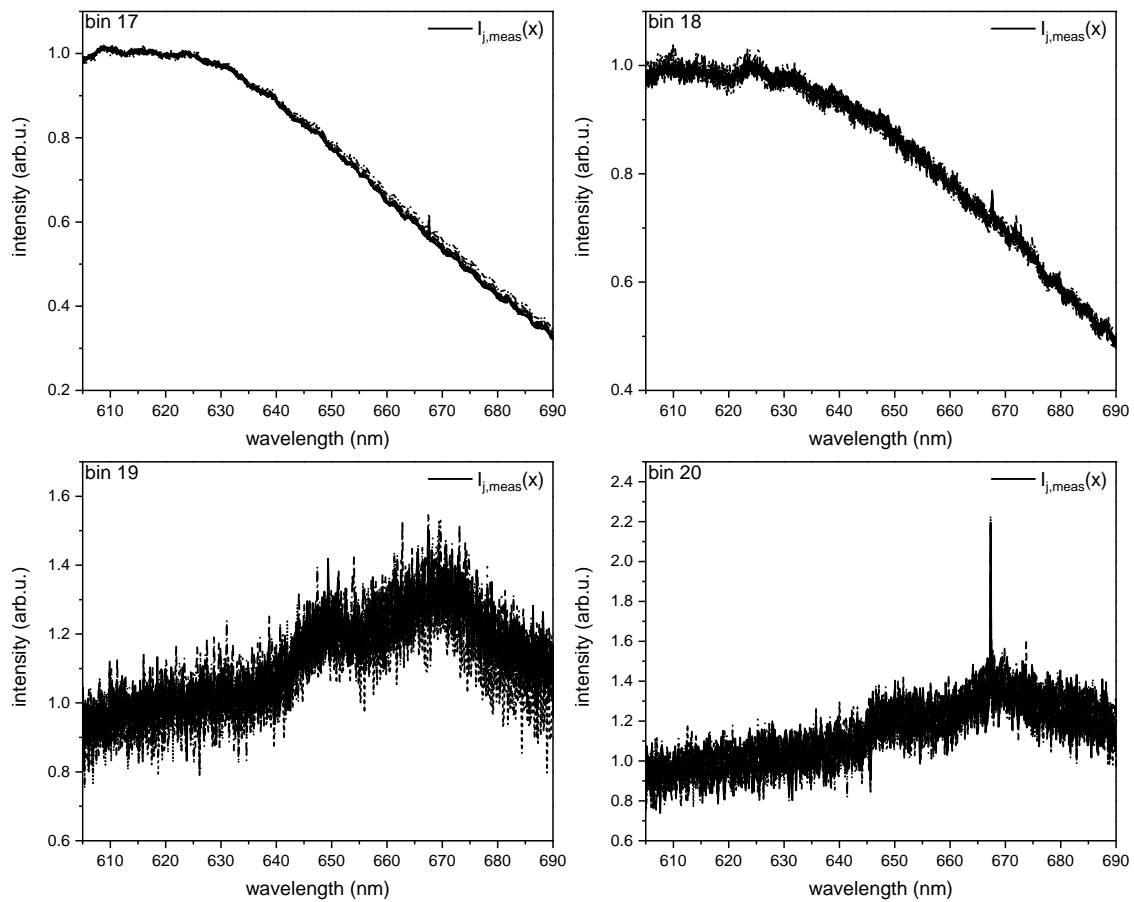


Figure A.4: Measured and normalized intensity curves of the SRM 2242. The curves are normalized at 624 nm. Using the alignment procedure the standard was positioned with the laser beam hitting directly under the surface. The curves split up into two groups. The values at 660 nm are shown in Appendix 5.4.

A.6 Histogram of the intensity values of the measured and normalized intensity curves of the SRM 2242 at 660 nm in every bin

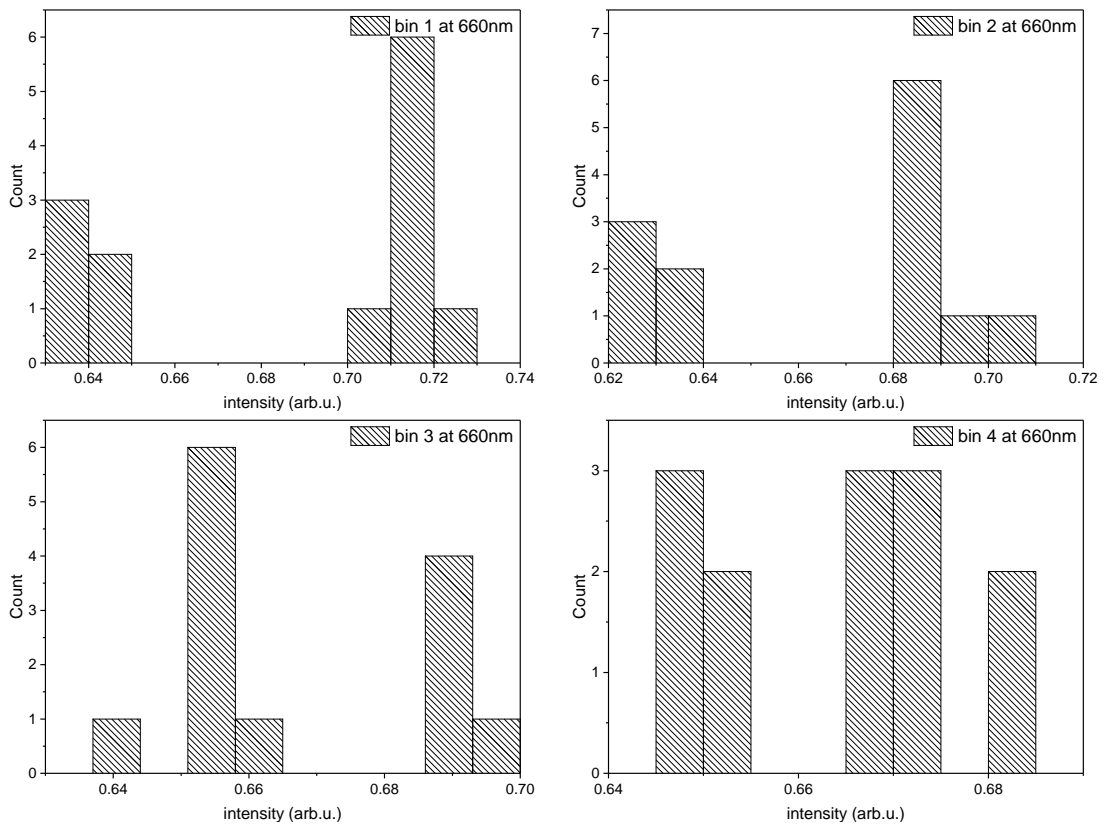
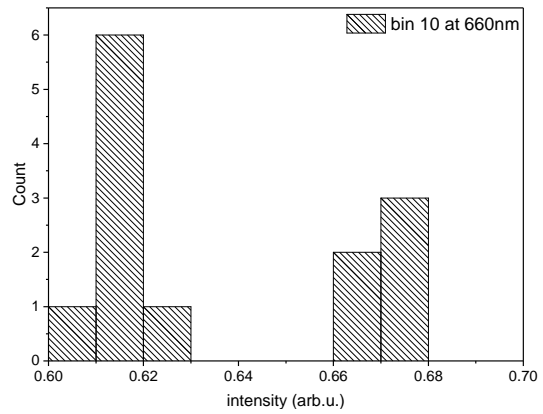
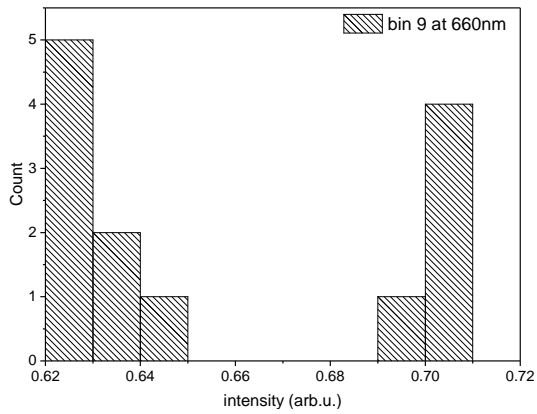
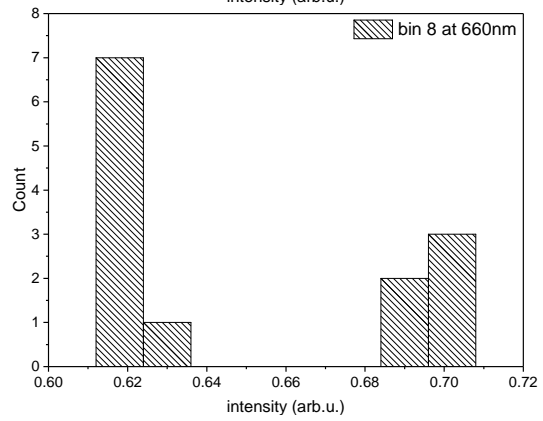
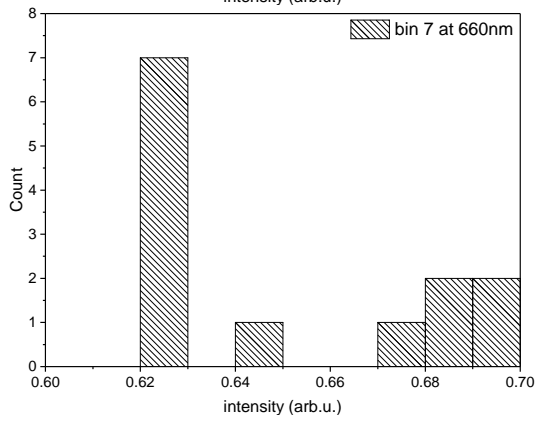
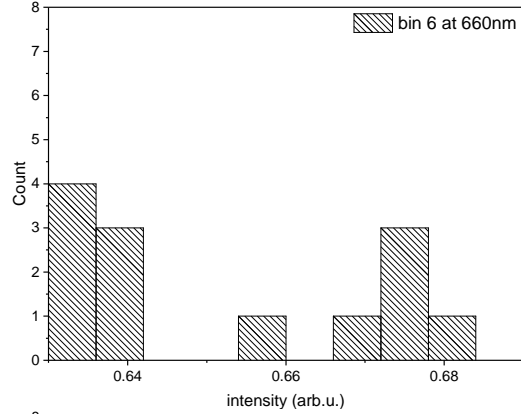
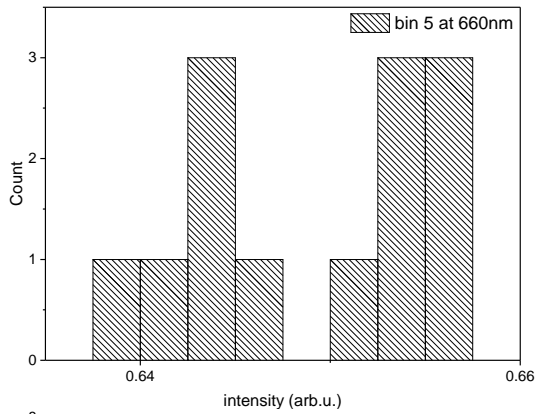
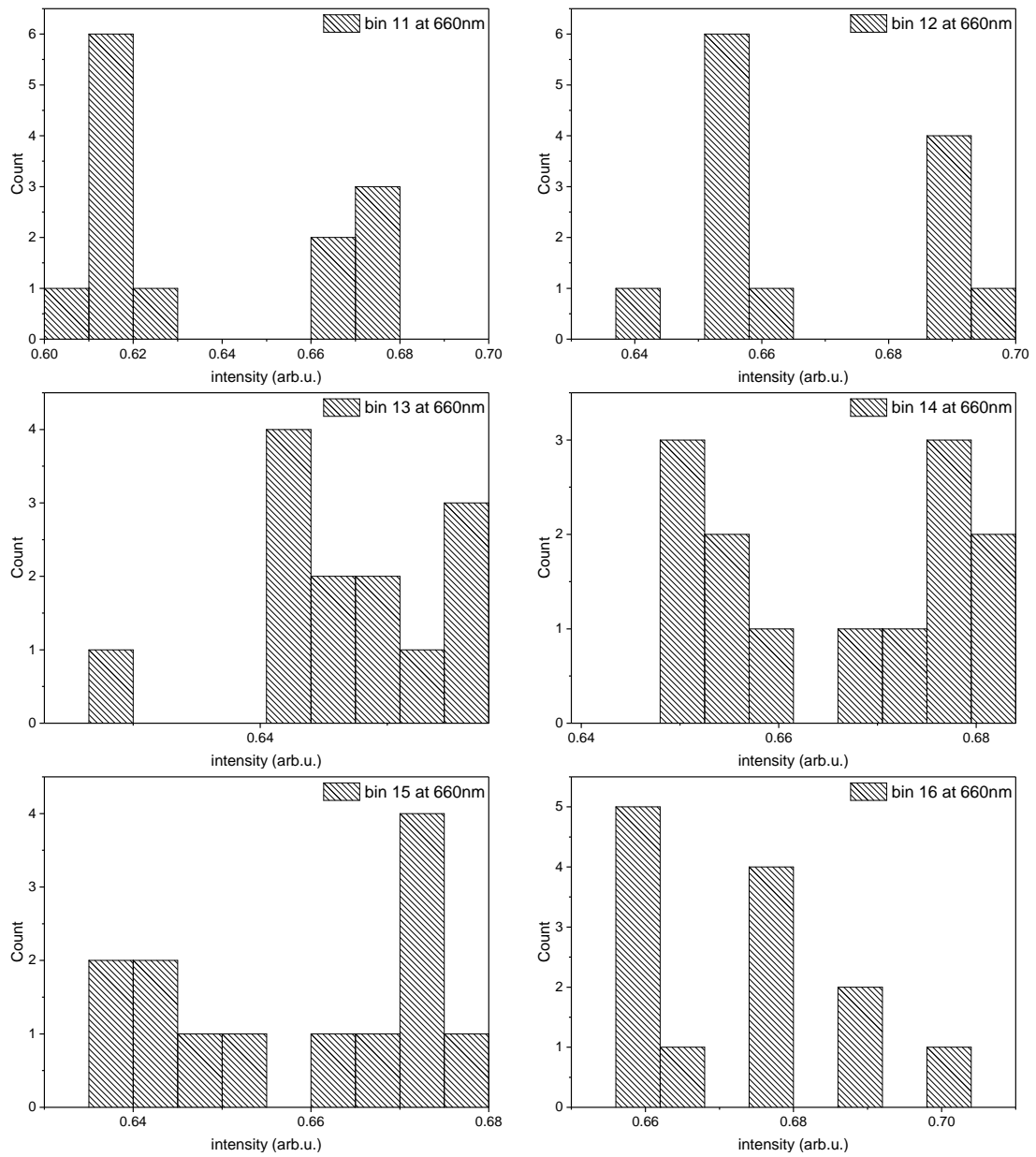


Figure A.5: text





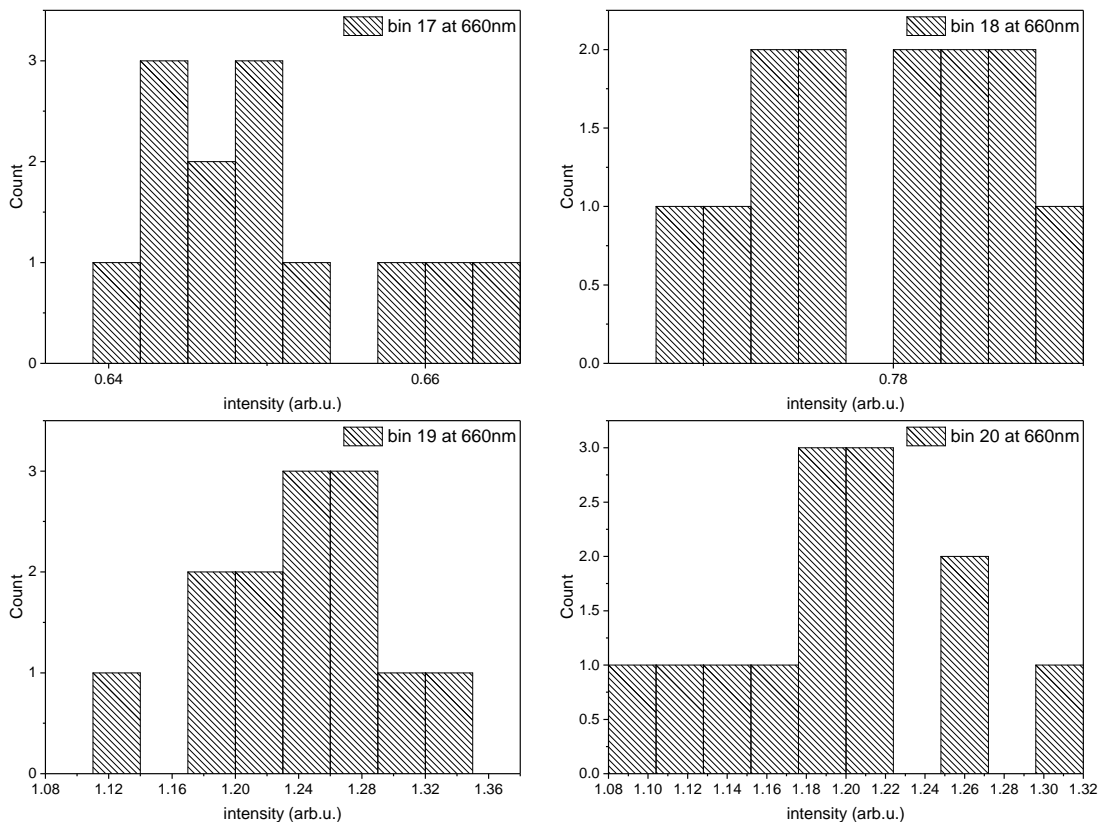


Figure A.5: Histogram of the intensity values of the measured and normalized intensity curves of the SRM 2242 at 660 nm. The intensity values clearly do not follow a Gaussian distribution. The distribution can be described as u-/arcsine-shaped. The values are taken at 660 nm in Appendix A.6.

A.7 Spectral sensitivity with the combined standard uncertainty confidence interval in every bin

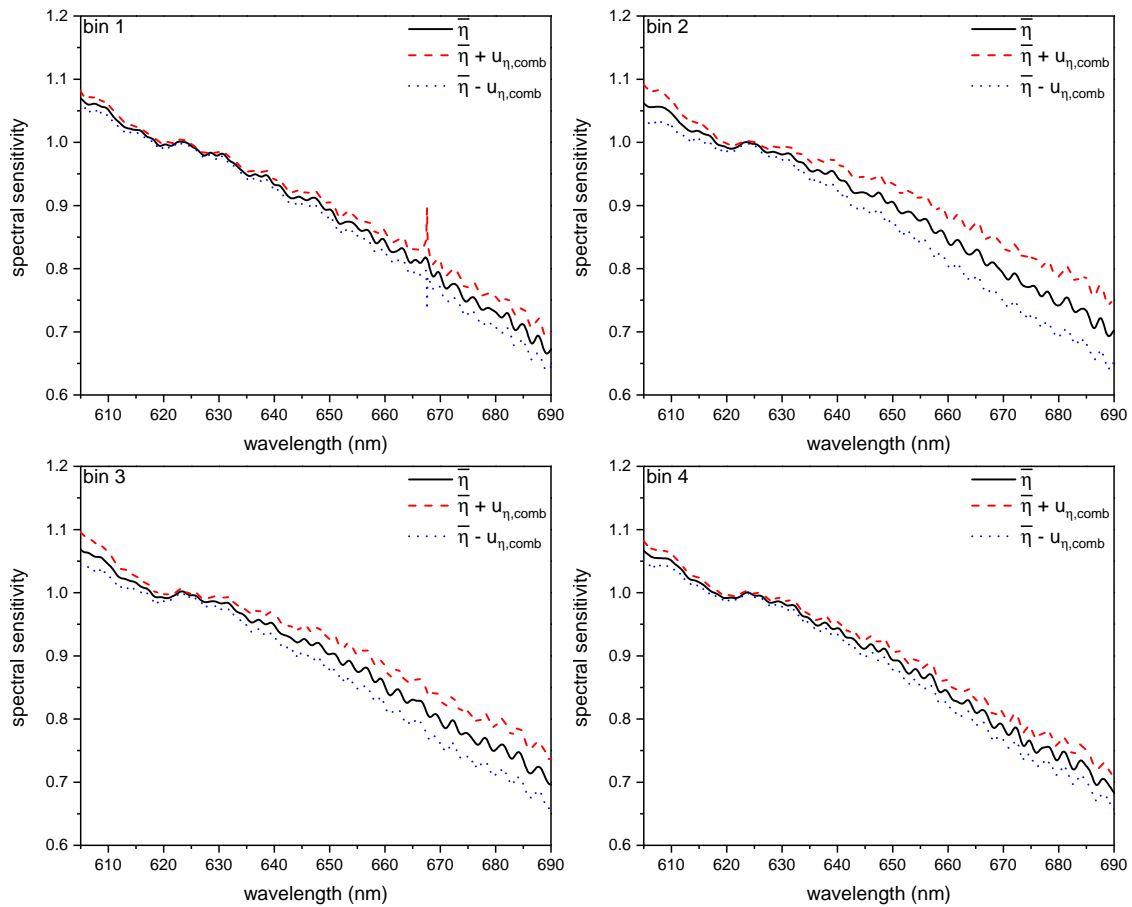
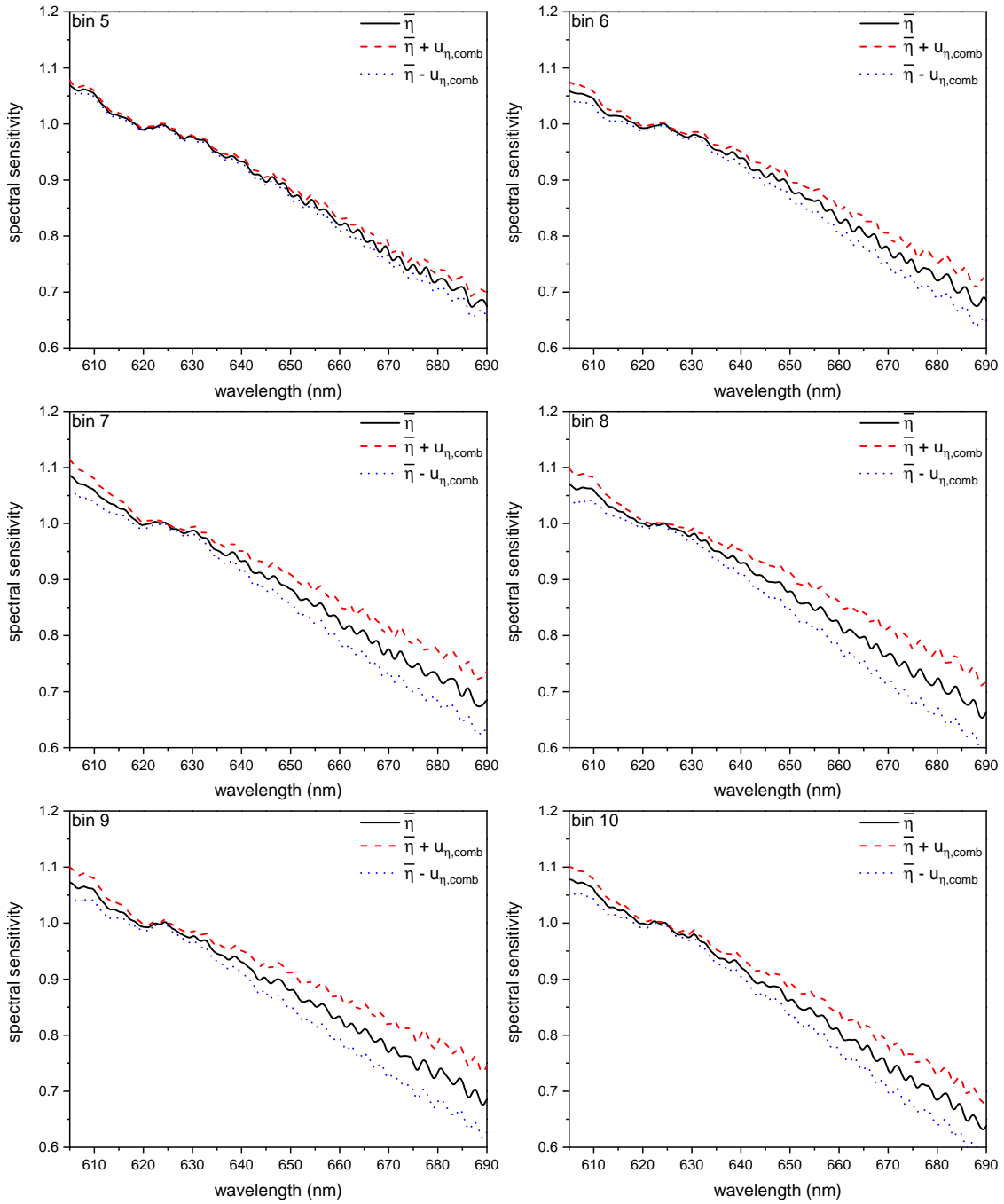
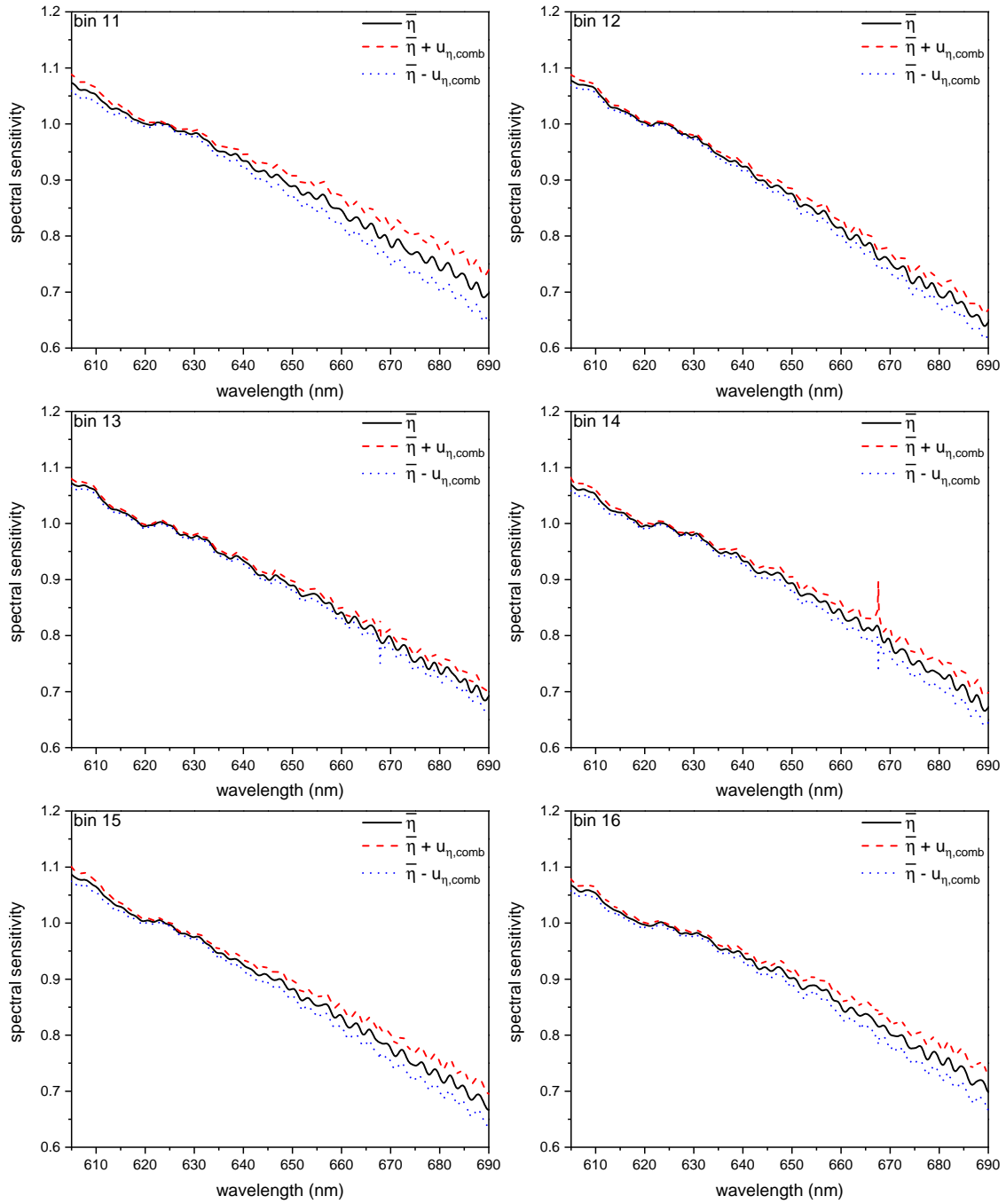


Figure A.6: text





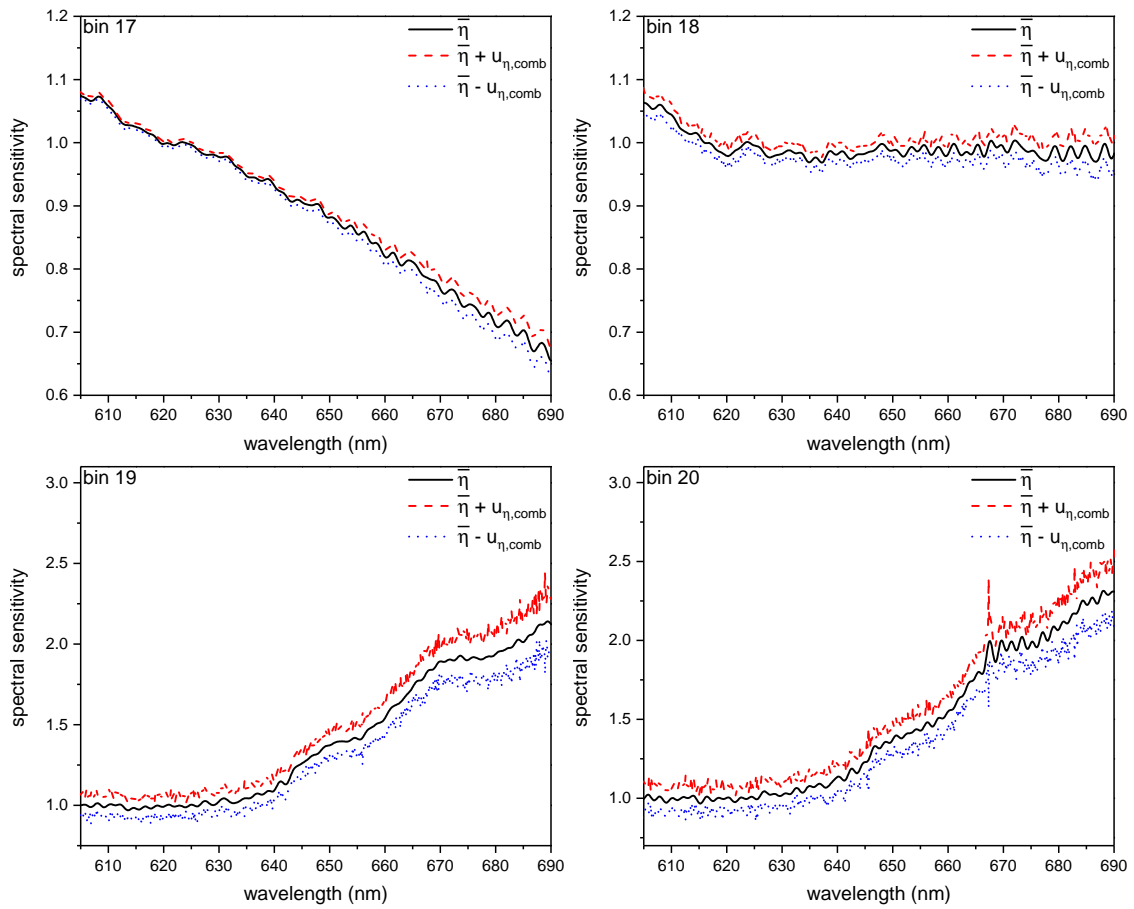


Figure A.6: Spectral sensitivity with the combined standard uncertainty confidence interval in every bin. Calculated using Fig. 5.7 and $\bar{\eta}$ from the data shown in Appendix A.4.

Appendix B

Full calculation of uncertainties

As described in section 5.4.3 the standard uncertainty of different processing steps of the LARASoft routine are calculated. All single shape fit scaling values F_x can be found here, while in section 5.4.3 only the standard uncertainty is discussed.

Table B.1: Full calculation of astigmatism correction uncertainty. Different astigmatism correction files are used within the LARASoft routine and the standard uncertainty of the 10 resulting shape fit scaling factors F_x is calculated.

Quantity	F_{T_2}	F_{DT}	F_{D_2}	F_{HT}	F_{HD}	F_{H_2}
AC-file 1	6578096.4	354325.3	115448.3	1888966.3	48926.9	71796.1
AC-file 2	6577526.2	354415.1	115511.7	1889186.8	49095.3	71876.4
AC-file 3	6577315.6	354272.8	115444.1	1888645.3	48876.7	71791.7
AC-file 4	6577713.1	354259.0	115488.6	1888619.0	48619.7	71821.9
AC-file 5	6577420.5	354211.8	115522.1	1888413.7	48389.7	71845.8
AC-file 6	6577572.8	354179.6	115478.0	1888664.8	48493.9	71889.1
AC-file 7	6576492.8	354136.8	115436.6	1888643.2	48729.1	71794.9
AC-file 8	6577891.4	354314.2	115441.8	1888803.7	48902.0	71787.7
AC-file 9	6577807.1	354224.5	115461.9	1888690.4	48661.7	71807.5
AC-file 10	6552091.1	351958.0	114872.0	1879778.6	48041.1	71235.4
\bar{F}_x	6574992.7	354029.7	115410.5	1887841.2	48673.6	71764.6
$u_{AC}(\bar{F}_x)$	2548.3	231.5	60.6	898.3	97.4	59.9
$u_{AC,p=68.27\%}$	2701.2	245.5	64.2	952.2	103.3	63.5
$u_{AC,p=68.27\%}/\bar{F}_x$ in %	0.04	0.07	0.06	0.05	0.21	0.09

Table B.2: Full calculation of baseline correction uncertainty. Different parameter sets are used for the SCARF algorithm within the LARASoft routine and the standard uncertainty of the 30 resulting shape fit scaling factors F_x is calculated.

$r1, r2, sg1, sg2$	F_{T_2}	F_{DT}	F_{D_2}	F_{HT}	F_{HD}	F_{H_2}
60, 80, 100, 120	731614.3	39804.6	12386.4	210048.9	5089.9	7855.7
55, 80, 100, 120	731599.4	39813.3	12371.1	210049.5	5093.5	7850.6
50, 80, 100, 120	731582.8	39821.8	12352.5	210051.6	5097.4	7844.3
45, 80, 100, 120	731564.3	39830.4	12329.3	210055.0	5099.5	7835.6
40, 80, 100, 120	731544.1	39838.2	12301.1	210059.8	5099.8	7824.7
35, 80, 100, 120	731521.1	39844.3	12268.0	210065.2	5098.5	7811.7
65, 80, 100, 120	731628.2	39795.6	12398.3	210049.7	5087.6	7860.1
70, 80, 100, 120	731642.0	39787.1	12407.1	210052.2	5087.1	7863.9
75, 80, 100, 120	731655.1	39779.4	12413.5	210056.7	5087.9	7867.0
80, 80, 100, 120	731667.5	39772.8	12417.8	210062.5	5090.3	7869.2
60, 100, 100, 120	731649.0	39814.5	12401.0	210058.7	5097.9	7844.7
60, 60, 100, 120	731572.8	39784.8	12361.6	210038.3	5078.9	7868.6
60, 40, 100, 120	731509.0	39741.2	12300.0	210026.9	5056.6	7894.3
80, 100, 100, 120	731702.3	39781.3	12431.8	210073.9	5104.2	7857.5
80, 60, 100, 120	731627.8	39753.4	12393.6	210050.9	5073.4	7883.2
80, 40, 100, 120	731570.4	39708.3	12333.3	210038.0	5043.4	7910.5
40, 100, 100, 120	731588.6	39847.4	12315.9	210070.7	5106.8	7813.6
40, 60, 100, 120	731488.6	39820.0	12275.9	210046.8	5088.8	7837.4
40, 40, 100, 120	731406.2	39780.1	12214.3	210033.5	5066.9	7862.3
60, 80, 80, 120	731695.0	39837.9	12397.3	210162.2	4971.5	7816.7
60, 80, 120, 120	731741.0	39840.7	12410.8	210056.5	5043.4	7846.3
60, 80, 140, 120	731980.3	39852.6	12448.9	210172.7	5024.1	7829.3
60, 80, 100, 80	731442.9	39892.9	12292.5	210080.8	5039.7	7778.4
60, 80, 100, 140	731808.7	39687.0	12470.9	210099.8	5095.6	7868.8
60, 80, 120, 80	731503.0	39950.8	12284.7	210078.3	4962.7	7748.1
60, 80, 120, 140	731949.3	39700.3	12520.9	210110.6	5060.9	7869.9
60, 80, 80, 80	731592.3	39912.8	12321.4	210188.4	4956.1	7750.7
60, 80, 80, 140	731870.5	39752.9	12474.3	210201.1	4982.8	7829.0
\bar{F}_x	731632.7	39805.2	12367.7	210076.4	5063.8	7842.6
$u_{AC}(\bar{F}_x)$	4.9	2.2	2.6	1.7	1.6	1.4
$u_{AC,p=68.27\%}$	5.0	2.2	2.6	1.7	1.7	1.4
$u_{AC,p=68.27\%}/\bar{F}_x$ in %	0.001	0.006	0.021	0.001	0.033	0.018

Bibliography

- [Ahm02] Q. R. Ahmad et al., *Direct evidence for neutrino flavor transformation from neutral current interactions in the Sudbury Neutrino Observatory*, Phys. Rev. Lett. **89** (2002) 011301.
- [An12] F. P. An et al., *Observation of Electron-Antineutrino Disappearance at Daya Bay*, Phys. Rev. Lett. **108**, 17 (2012) 171803.
- [Ase11] V. N. Aseev et al., *Upper limit on the electron antineutrino mass from the Troitsk experiment*, Phys. Rev. D **84**, 11 (2011) 112003.
- [Atk06] P. W. Atkins et al., *Physikalische Chemie (v. 4) (German Edition)*, Wiley (2006).
- [Bab12] M. Babutzka et al., *Monitoring of the operating parameters of the KATRIN Windowless Gaseous Tritium Source*, New J. Phys. **14**, 10 (2012) 103046.
- [Bab14] M. Babutzka, *Design and development for the Rearsection of the KATRIN experiment*, Phd thesis, Karlsruhe Institute of Technology (2014).
- [Bel95] A. I. Belesev et al., *Results of the troitsk experiment on the search for the electron antineutrino rest mass in tritium beta-decay*, Phys. Lett. B **350**, 2 (1995) 263 – 272.
- [Bod15] L. I. Bodine et al., *Assessment of molecular effects on neutrino mass measurements from tritium beta decay*, Phys. Rev. **C91**, 3 (2015) 035505.
- [Cam12] A. Campargue et al., *The absorption spectrum of H₂: CRDS measurements of the (2-0) band, review of the literature data and accurate ab initio line list up to 35 000 cm⁻¹*, Phys. Chem. Chem. Phys. **14** (2012) 802–815.
- [Cha14] J. Chadwick, *The intensity distribution in magnetic spectrum of β -rays of radium b + c*, Verhandl. Dtsch. phys. Ges. **16** (1914) 383.
- [Dav68] R. Davis et al., *Search for Neutrinos from the Sun*, Phys. Rev. Lett. **20**, 21 (1968) 1205–1209.
- [Dem07] *Laserspektroskopie : Grundlagen und Techniken* (2007).
- [Dos06] N. Doss et al., *Molecular effects in investigations of tritium molecule β decay endpoint experiments*, Phys. Rev. C **73**, 1 (2006) 025502.
- [Dre13] G. Drexlin et al., *Current Direct Neutrino Mass Experiments*, Adv. High En. Phys. **2013**, 293986 (2013).

- [Fis11] S. Fischer et al., *Monitoring of tritium purity during long-term circulation in the KATRIN test experiment LOOPINO using laser Raman spectroscopy*, *Fusion Sci. Technol.* **60**, 3 (2011) 925–930.
- [Fis14] S. Fischer, *Commissioning of the KATRIN Raman system and durability studies of optical coatings in glove box and tritium atmospheres*, Phd-thesis, Karlsruhe Institute of Technology (2014).
- [Fuk98a] Y. Fukuda et al., *Evidence for oscillation of atmospheric neutrinos*, *Phys. Rev. Lett.* **81** (1998) 1562–1567.
- [Fuk98b] Y. Fukuda et al., *Measurements of the Solar Neutrino Flux from Super-Kamiokande's First 300 Days*, *Phys. Rev. Lett.* **81**, 6 (1998) 1158–1162.
- [Gol58] M. Goldhaber et al., *Helicity of Neutrinos*, *Phys. Rev.* **109** (1958) 1015–1017.
- [Hac17] M. Hackenjos, *PhD thesis in preparation*, Phd thesis, Karlsruhe Institute of Technology (2017).
- [Hak06] H. Haken et al., *Molekülphysik und Quantenchemie: Einführung in die experimentellen und theoretischen Grundlagen*, Springer (2006).
- [Jam12] T. M. James et al., *Documentation of SpecTools: Automated Procedure for Quantitative Spectroscopic Analysis Combining Improved Background Subtraction, Cosmic Ray Removal and Peak Analysis* (2012).
- [Jam13a] T. M. James, *Quantitative Raman spectroscopy of gases related to KATRIN*, Phd-thesis, Swansea University (2013).
- [JCG08] Joint Committee for Guides in Metrology, *JCGM 200:2008*, Joint Committee for Guides in Metrology (2008).
- [KAT05] KATRIN Collaboration, *KATRIN Design Report 2004*, FZK - FZKA 7090 (2005).
- [Kra05] C. Kraus et al., *Final results from phase II of the Mainz neutrino mass search in tritium decay*, *Eur. Phys. J. C.* **40**, 4 (2005) 447–468.
- [Kuc16] L. Kuckert, *The Windowless Gaseous Tritium Source of the KATRIN Experiment - Characterisation of Gas Dynamical and Plasma Properties*, Phd thesis, Karlsruhe Institute of Technology (2016).
- [Lon02] D. A. Long, *The Raman Effect: A Unified Treatment of the Theory of Raman Scattering by Molecules*, John Wiley & Sons Ltd (2002).
- [Mak62] Z. Maki et al., *Remarks on the Unified Model of Elementary Particles*, *Prog. Theor. Phys.* **28**, 5 (1962) 870–880.
- [McM06] R. L. McCreery, *Handbook of Vibrational Spectroscopy*, chapter Photometric Standards for Raman Spectroscopy, John Wiley & Sons, Ltd (2006).
- [Mik85] S. P. Mikheev et al., *Resonance Amplification of Oscillations in Matter and Spectroscopy of Solar Neutrinos*, *Sov. J. Nucl. Phys.* **42** (1985) 913–917, [*Yad. Fiz.*42,1441(1985)].

- [Mye15] E. G. Myers et al., *Atomic Masses of Tritium and Helium-3*, Phys. Rev. Lett. **114** (2015) 013003.
- [NIS08] *Certificate of Analysis (Standard Ref. Mat. 2242)*, NIST, Gaithersburg, MD, USA (2008).
- [Nob15] Nobelprize.org, *The Nobel Prize in Physics 2015*, Web. 4 Nov 2017 (2015).
- [Pac14] K. Pachucki et al., *Accurate adiabatic correction in the hydrogen molecule*, The Journal of Chemical Physics **141**, 22 (2014) 224103.
- [Pac15] K. Pachucki et al., *Leading order nonadiabatic corrections to rovibrational levels of H₂, D₂, and T₂*, The Journal of Chemical Physics **143**, 3 (2015) 034111.
- [Pat16] C. Patrignani et al., *Review of Particle Physics*, Chin. Phys. **C40**, 10 (2016) 100001.
- [Pau30] W. Pauli, *Offener Brief an die Gruppe der Radioaktiven bei der Gauvereins-Tagung zu Tübingen (1930)*, wissenschaftlicher Briefwechsel mit Bohr, Einstein, Heisenberg, u.a: 1930-1939, Springer.
- [Pau85] W. Pauli et al., *Wissenschaftlicher Briefwechsel mit Bohr, Einstein, Heisenberg u.a. Band II: 1930-1939*, Editor Springer-Verlag Berlin Heidelberg (1985).
- [Pic92] A. Picard et al., *A solenoid retarding spectrometer with high resolution and transmission for keV electrons*, Nucl. Instrum. Meth. B **63**, 3 (1992) 345 – 358.
- [Pon57] B. Pontecorvo, *Mesonium and anti-mesonium*, Sov. Phys. JETP **6** (1957) 429, [Zh. Eksp. Teor. Fiz.33,549(1957)].
- [Pon68] B. Pontecorvo, *Neutrino Experiments and the Problem of Conservation of Leptonic Charge*, Sov. Phys. JETP **26** (1968) 984–988, [Zh. Eksp. Teor. Fiz.53,1717(1967)].
- [Puc17] M. Puchalski et al., *Relativistic corrections for the ground electronic state of molecular hydrogen*, Phys. Rev. A **95** (2017) 052506.
- [Ram28] C. V. Raman et al., *A new type of secondary radiation*, Nature **121** (1928) 501–502.
- [Rei56] F. Reines et al., *The Neutrino*, Nature **178** (1956) 446–449.
- [Röll15] M. Röllig, *Tritium analytics by beta induced X-ray spectrometry*, Phd thesis, Karlsruhe Institute of Technology (2015).
- [LeR11] R. J. L. Roy, *Recalculation of Raman transition matrix elements of all hydrogen isotopologues for 532nm laser excitation*, Private communication (2011).
- [Rup12] S. Rupp, *Proof of concept of a calibration method for the laser Raman system for KATRIN based on the determination of the system's spectral sensitivity*, Diploma thesis, Karlsruhe Institute of Technology (2012).
- [Sch87] C. Schwartz et al., *Nonadiabatic eigenvalues and adiabatic matrix elements for all isotopes of diatomic hydrogen*, J. Mol. Spectrosc. **121**, 2 (1987) 420 – 439.

- [Sch09] M. Schlösser, *First Laser Raman measurements with tritium for KATRIN and studies of systematic effects of the LARA-setup*, Diploma thesis, Karlsruhe Institute of Technology (2009).
- [Sch12a] M. Schlösser et al., *Accuracy of the Laser Raman system for KATRIN*, Proceedings of the International School of Physics "Enrico Fermi", Course CLXXXII "Neutrino Physics and Astrophysics", edited by G. Bellini (2012) 333–336.
- [Sch13a] M. Schlösser, *Accurate calibration of the Raman system for the Karlsruhe Tritium Neutrino Experiment*, Phd thesis, Karlsruhe Institute of Technology (2013).
- [Sch13d] M. Schlösser et al., *Accurate calibration of the laser Raman system for the Karlsruhe Tritium Neutrino Experiment*, J. Mol. Structr. **1044** (2013) 61–66.
- [Sch13b] M. Schlösser et al., *Evaluation method for Raman depolarization measurements including geometrical effects and polarization aberrations*, J. Raman Spectrosc. **44**, 3 (2013) 453–462.
- [Sch13a] M. Schlösser et al., *In-Line Calibration of Raman Systems for Analysis of Gas Mixtures of Hydrogen Isotopologues with Sub-Percent Accuracy*, Anal. Chem. **85**, 5 (2013) 2739–2745.
- [Sch14a] M. Schlösser et al., *Handling of uncertainties in LARASoft* (2014).
- [Sch14b] J. Schwarz, *Detector-System Implementation for the KATRIN Experiment*, Phd thesis, Karlsruhe Institute of Technology (2014).
- [Sch15a] M. Schlösser et al., *Relative Intensity Correction of Raman Systems with National Institute of Standards and Technology Standard Reference Material 2242 in 90°-Scattering Geometry*, Applied Spectroscopy **69**, 5 (2015) 597–607.
- [Sch15b] W. Schmid et al., *Main steps to the determination of measurement uncertainty according to GUM* (2015).
- [Sei11] H. Seitz, *Kalibrierung des KATRIN Laser-Raman-Systems mit katalytisch hergestellten, inaktiven Wasserstoffisotopologen*, Bachelorarbeit, Karlsruher Institut für Technologie (2011).
- [Sme23] A. Smekal, *Zur Quantentheorie der Dispersion*, Naturwissenschaften **11**, 43 (1923) 873–875.
- [Stu10b] M. Sturm, *Aufbau und Test des Inner-Loop-Systems der Tritiumquelle von KATRIN*, Phd thesis, Karlsruhe Institute of Technology (2010).
- [Stu10a] M. Sturm et al., *Monitoring of all hydrogen isotopologues at tritium laboratory Karlsruhe using Raman spectroscopy*, Laser Phys. **20**, 2 (2010) 493–507.
- [Wol78] L. Wolfenstein, *Neutrino oscillations in matter*, Phys. Rev. D **17** (1978) 2369–2374.

Danksagung

Diese Arbeit wäre ohne die Hilfe und Unterstützung vieler Personen nicht möglich gewesen.

Ich danke Prof. Dr. Guido Drexlin, der diese interessante Arbeit ermöglicht hat.

Ein besonderer Dank gilt Prof. Dr. Ulrich Husemann, der nicht nur die Zweitkorrektur für diese Arbeit übernommen hat, sondern auch bei persönlichen Schwierigkeiten beraten und geholfen hat.

Für seine wertvollen Beiträge bei den Besuchen in Karlsruhe und das Interesse an der Arbeit bedanke ich mich bei Prof. Dr. Helmut Telle.

Ich bedanke mich ebenso bei Dr. Sebastian Fischer dafür, dass er mich in der Anfangszeit der Arbeit betreut hat. Durch seine Motivation, sein Bemühen und seinen Einsatz konnte er mich schnell für diese Arbeit begeistern.

Für die Betreuung der Arbeit bedanke ich mich außerdem herzlichst bei Simon Niemes, Dr. Magnus Schlösser und Hendrik Seitz-Moskaliuk. Sie standen mir immer mit Rat und Tat zur Seite. Besonders bedanke ich mich für die gute Kommunikation, viel Verständnis und den regelmäßigen wissenschaftlichen Austausch. Dadurch konnte ich während der Masterarbeit viel über die Materie und darüber hinaus lernen. Danke auch, für das Korrekturlesen dieser Arbeit.

Für die Hilfe bei zahlreichen Arbeiten im Labor bedanke ich mich bei Andreas Off und Bennet Krasch.

Bernhard Heinle danke ich für seine Unterstützung, seine hilfreichen Einweisungen und sein Vertrauen bei den Arbeiten an der Handschuhbox.

Ich danke Eva Porter und Sylvia Krieger dafür, dass sie mir bei den zahlreichen Dokumenten geholfen haben und ich mit jeder Frage zu ihnen kommen konnte.

Ein großes Dankeschön gilt allen Kollegen für das gute Arbeitsklima und dafür, dass ich von jedem so freundlich aufgenommen wurde.

Meiner Mutter Olga Zeller und meiner Schwester Nicole Faltinski danke ich herzlichst für ihre Unterstützung und Geduld, nicht nur während der Masterarbeit. Ohne sie wäre mein Studium nicht möglich gewesen.

Zuletzt bedanke ich mich bei meiner Freundin Kristina Geistert für alles was sie auf sich genommen hat, um mich zu unterstützen. Sie zeigt mir was wirklich wichtig im Leben ist.